Title

Polymer Composites for Latent Heat Thermal Energy Storage

Permalink

https://escholarship.org/uc/item/4x7067qv

Author

Roy, Souvik

Publication Date

2023

UNIVERSITY OF CALIFORNIA, MERCED

Polymer Composites for Latent Heat Thermal Energy Storage

A dissertation submitted in partial satisfaction of the
requirements for the degree
Doctor of Philosophy

in

Mechanical Engineering

by

Souvik Roy

Committee in charge:

Prof. Gerardo Diaz, Chair
Prof. Abel Chuang
Prof. Venkattraman Ayyaswamy
Prof. James Palko

2023

The dissertation of Souvik Roy is approved, and
it is acceptable in quality and form for publication
on microfilm and electronically:

(Prof. Abel Chuang)

(Prof. Venkattraman Ayyaswamy)

(Prof. James Palko)

(Prof. Gerardo Diaz, Chair)

University of California, Merced

2023

DEDICATION

To my parents and my wife,
Who saw light in my darkest nights,
And to my advisor,
Who turned that light into dawn—
Your belief forged this path.
This achievement is ours.

EPIGRAPH

Karmanye vadhikaraste Ma Phaleshu Kadachana,
Ma Karmaphalaheturbhurma Te Sangostvakarmani
—Bhagavad Gita, 2-47.

TABLE OF CONTENTS

Signature Page ii

Dedication iii

Epigraph iii

Table of Contents v

List of Figures vii

List of Tables xv

Acknowledgements xvi

Vita and Publications xvii

Abstract xviii

Chapter 1 Thermal Energy Storage 1
- 1.1 Introduction 1
- 1.2 Literature Review 2
- 1.3 Classification of Thermal Energy Storage 2
- 1.4 Energy Sources for Thermal Energy Storage Systems . 4
- 1.5 Latent Heat Storage Materials 5
- 1.6 Phase Change Material Performance Enhancement . . 7
- 1.7 Packed Bed Thermal Energy Storage Systems 8
- 1.8 Application 9
- 1.9 Research Motivation 9
- 1.10 Summary of Research Objectives 11
- 1.11 Structure of the Thesis 13

Chapter 2 High Density Polyethylene Composite as Phase Change Material for Latent Heat Thermal Energy Storage - Bench-Scale Experimental Study 14
- 2.1 Introduction 14
- 2.2 Methods 15
  - 2.2.1 Media Synthesis 15
  - 2.2.2 Differential Scanning Calorimetry 17
  - 2.2.3 Experimental Setup 17
  - 2.2.4 Bulk Calorimetry Characterization 21
  - 2.2.5 Exergetic Efficiency 23
  - 2.2.6 Error Analysis 24
- 2.3 Results and Discussion 24
  - 2.3.1 Local Scale Heat Transfer Modelling of the Media 25
  - 2.3.2 Media Performance 26
  - 2.3.3 System Performance 32
  - 2.3.4 Effect of Flow-Reversal in the Bed 46
  - 2.3.5 Comparison with Existing HDPE Latent Heat Storage Systems 52

2.4 Conclusion 54

Chapter 3 High Density Polyethylene Composite as Phase Change Material for Latent Heat Thermal Energy Storage - Pilot-Scale Experimental Study 56
3.1 Introduction 56
3.2 Approach 57
3.2.1 Media 57
3.2.2 Pilot Scale Storage System 62
3.2.3 Thermal Characterization 68
3.2.4 Media Stability Characterization 71
3.3 Results and Discussion 74
3.3.1 Media Performance 74
3.3.2 System Thermal Performance 83
3.3.3 Comparison with Existing HDPE Latent Heat Storage Systems 92
3.4 Conclusion 95

Chapter 4 Rapid Steam Production and Performance Enhancement of a Steam Accumulator Using Packed-Bed Latent Heat Thermal Energy Storage Technology 97
4.1 Introduction 97
4.2 Conventional Steam Accumulator 101
4.3 Packed Bed Steam Accumulator 102
4.3.1 Latent Heat Thermal Energy Storage Media . . 103
4.4 Performance Models 105
4.4.1 Steam Storage Capacity 105
4.4.2 Kinetic Behavior 108
4.4.3 Solidification of Slab: Constant Temperature Boundary Condition 108
4.4.4 Solidification of Slab: Constant Heat Flux Boundary Condition 112
4.5 Results 116
4.5.1 Example System 116
4.5.2 Capacity Enhancement 116
4.5.3 Steam Accumulator Performance at Constant Pressure Steam Output 122
4.5.4 Steam Accumulator Performance at Constant Thermal Energy Output 124
4.5.5 TES Economics through Low-Power Heat Pump Integration 128
4.5.6 Comparison with Existing Steam Accumulator Models 135
4.6 Conclusion 137

Chapter 5 Conclusions 138
5.1 Summary of Research Findings 139
5.2 Future Work 140

Bibliography 142

LIST OF FIGURES

Figure 1.1: Types of TES 3
Figure 1.2: Types of PCM based on chemical composition. 5
Figure 1.3: Thesis within the broad Thermal Energy Storage landscape 11

Figure 2.1: Schematic of custom-made high shear mixer designed to blend treated glass fibers with molten HDPE. The mixer features a disc-shaped wooden head attached to the spindle of a drill press. A container holding the material sits atop a hot plate, with a temperature maintained at 160 °C. The spindle speed is fixed at 300 RPM to ensure uniform mixing. Prior to mixing, materials are preheated in a vacuum oven at 150 °C. 16
Figure 2.2: Setup for bulk experiments. (a) Flow loop and control schematic. (b) System in operational condition. (The photograph here shows a previous flow loop with flexible tubing, reversible pump, and single flow heater.) 18
Figure 2.3: Schematic of filled media containment vessel and fluid flow direction during charging and discharging. 20
Figure 2.4: Schematic of phase change media composite pellets in a heat transfer fluid (yellow). The red arrows represent interstitial flow of the heat transfer fluid between the media pellets. The blue rectangles here represent the media pellets, which in reality, are of irregular shape and size with an average thickness of 4 mm. 25
Figure 2.5: Phase change media for the TES system using form stable, epoxy coated, glass fiber reinforced, high-density polyethylene composite pellets (as synthesized). The pellets are roughly 4 mm thick and approximately 1 cm on a side. 26
Figure 2.6: DSC traces for pristine HDPE (black curve), a sample of the fresh composite (blue curve) and another sample of the composite aged in glycerol after 100 complete melt/freeze cycles (red curve). The thermal scan rate is 5 °C/min. The latent heat of melting (calculated) for the virgin HDPE, fresh composite (sample 1) and the aged one (sample 2) are 192 J/g, 181 J/g and 149 J/g respectively. The peak melting temperatures are 133.9 °C, 132.2 °C and 133.6 °C, respectively. The peak crystallization temperatures are 120 °C, 118.8 °C and 118.8 °C, respectively. 27
Figure 2.7: Schematic of the HDPE/glass fiber composite with epoxy exoskeleton. (a) Single pellet showing the random distribution of glass-fibers in the HDPE matrix and ossible leakage of HDPE from the gaps of the exoskeleton. (b) Pellets adhered with one another at their points of contact to form a stable open porous structure. 29

Figure 2.8: Integrity of storage media consisting of HDPE matrix with 15% glass fiber reinforcement and epoxy coating a.) immediately after synthesis and following melting/freezing in bed for b.) 30 thermal cycles. c.) 100 thermal cycles. d.) Small subset of media showing significant HDPE leakage after 100 thermal cycle. About 8 -10% of the samples tested showed some visible leakage. e.) A sample showing worst case leakage. f.) Composite pellets stuck with each other to form a stable porous structure. 30
Figure 2.9: Example charge/discharge cycle for TES system. Mass flux of glycerol is 173 g/m^2/s. After complete charging of the bed, flow is reversed for discharging. 32
Figure 2.10: Temperature vs time traces during charging: (a) for different charging temperatures (140.0 °C, 145 °C, 137 °C). The initial effective bed temperature and the mass flux of glycerol are fixed. (b) For different initial effective bed temperatures (110 °C, 115 °C, 120 °C). The mass flux and charging temperature are kept constant. (c) For different mass fluxes of glycerol. The initial effective bed temperature and charging temperature are maintained constant. 34
Figure 2.11: Temperature vs time traces for different discharging conditions. (a) Temperature profile during discharging from an initial bed temperature at 140 °C. The mass flux of glycerol is held constant at 173 g/m^2/s. The bed inlet temperature during the discharging process is studied for two different cases: 110 °C and 115 °C. (b) Temperature profile during discharging from steady bed outlet temperature of 145 °C, 140 °C and 133.5 °C at 173 g/m^2/s of glycerol mass flux to 110 °C final bed temperature. (c) Temperature profile during discharging from a steady bed temperature of 140 °C to 115 °C for different mass fluxes of glycerol. 36
Figure 2.12: Effect of minimum discharge temperature (a) Charge/discharge cycle for TES system, with initial bed temperature of 110 °C, charging temperature of 140 °C, and inlet temperature of 110 °C on discharge at mass flux of 173 g/m^2/s glycerol. (b) Cumulative energy versus discharging time and (c) cumulative energy versus fluid inlet temperature that can be extracted during the discharging cycle shown in (a). 38
Figure 2.13: Thermal performance for differing fluid inlet temperatures on discharge (nominally 110 °C and 115 °C). The initial bed temperature at discharge is 140 °C, and mass flux of glycerol is 173 g/m^2/s for both cases. (a) latent and total energy stored (b) average thermal power delivered. 40

Figure 2.14: Three discharging cases were studied with different initial bed temperatures (nominal) at 145 °C, 140 °C and 133 °C and a constant fluid inlet temperature of 110 °C and mass flux of glycerol at 173 g/m^2/s. (a) & (b) represent bar charts shows the latent energy and power respectively extracted during the discharging process for these three different discharging cases. (c) An example of an incomplete charge/discharge cycle for the TES system. Charging of the packed bed started from an initial bed temperature of 115 °C for a charging temperature of 135 °C (nominal). The discharging cycle with a fluid inlet temperature of 110 °C commenced before complete charging of the packed bed. The mass flux was held constant at 173 g/m^2/s of glycerol. 41

Figure 2.15: (a) Latent heat vs. discharge time and (b) total stored heat vs. discharge time during discharging from a steady bed temperature of 140 °C to 115 °C for different mass fluxes of glycerol. The numerical values corresponding to each data point represent glycerol mass fluxes in g·m^{-2}·s^{-1}. (c) Average thermal power corresponding total and latent heat vs. mass flux of glycerol. 43

Figure 2.16: Thermocouple arrangement in the packed bed system (a) schematic (b) actual. 48

Figure 2.17: Temperature distribution during discharging cycle within the bed along with the inlet and outlet bed temperatures along the (c) axial and (d) radial direction of the media containment. The initial bed temperature is 140 °C and the discharging temperature is 115 °C. The mass flow rate of glycerol was kept constant at 3.16 g/s. 49

Figure 2.18: Schematic of flow loop while (a) charging and (b) discharging. Packed bed during (c) charging showing hot fluid enters from the top and colder fluid exits from the bottom, (d) discharging showing hot fluid exits from the top and colder fluid enters from the bottom maintaining a stable temperature gradient in the bed. 50

Figure 2.19: Bed behavior without flow reversal. (a) Temperature traces of the bed outlet shows that there is no clearly defined exotherm plateau as found during flow-reversal. (b) Schematic of packed bed during discharging without flow-reversal, showing cold fluid enters from the top and hot fluid exits from the bottom. Given low hydrodynamic resistance of the bed, it is likely that colder fluid now unstable because of its weight, falls down in a column within the bed and collects at the bottom. 51

Figure 2.20: Schematic of a trickling flow of heat transfer fluid in the packed bed thermal energy storage system during discharging. Unlike the fully submerged system, the flow direction is not reversed, rather a unidirectional flow pattern is used. 53

Figure 3.1: Composite media production setup and components. (a) Schematic of the composite media layers inside the heated press, indicating a selection of the polyester batting and HDPE pellet layers. A total of 10 layers of polyester batting and 9 layers of HDPE pellets are used in the actual setup, though only 4 layers of batting and 3 layers of HDPE are illustrated here for simplicity. Also shown is the consolidated composite plate post-press, with thickness determined by the height of the spacers used between the two aluminum heating plates. (b) Actual ingredients and assembly of the composite media. On the left is a demonstration of HDPE pellets spread over a layer of polyester batting. On the right is an image of two stacks of the materials (before compression), separated by a PTFE Teflon sheet, taken during the construction of a small-scale prototype composite. 60
Figure 3.2: (a) Schematic of the custom-made, large heated press used for composite media sheet production, and (b) the final assembly of the full-scale setup. The press features a footprint of approximately 0.75 m × 0.75 m and is equipped with five heaters ensuring symmetrical heat distribution. The production setup consists of ten stacks of alternating layers of polyester batting and HDPE, each constituting a single media sheet. Unistrut attachments and threaded rods are used for compression, while spacers determine the final thickness of the consolidated composite sheet. The temperature and power to the heaters are controlled and monitored via a computer-controlled relay and K-type thermocouples. 61
Figure 3.3: (a) Schematic of the thermal energy storage system featuring a unidirectional gear pump, which facilitates two flow paths that can be manually switched using four controlling ball valves. (b) A fully insulated, full-scale TES system with an inline heater installed for media charging. The packed bed, comprising strategically arranged composite plates, is contained within a stainless-steel tank. The bed is designed for unimpeded flow of the heat transfer fluid and minimized porosity for increased storage capacity. The entire system is located outside of a climate-controlled area. 63
Figure 3.4: Detailed overview of the thermal energy storage system and its functioning: (a) A system schematic situated in a 350-gallon stainless-steel IBC, displaying the strategic arrangement of composite plates, supported by a unistrut structure and a thick aluminum mesh. The schematic also illustrates the containment of PCM surrounded by glycerol, the color gradient denoting fluid temperature distribution, and the insulation measures adopted for reducing heat loss. (b) A closer look at the bed, revealing the serpentine interstitial fluid flow amid the plates. This tailored design fosters optimized system parameters, including porosity, liquid volume, capacity, weight, cost, and heat loss. 65

Figure 3.5: Tiling design for alternate stacking in the bed. Gridlines represent the border of each composite block through which HTF will flow. HTF flow will be directed along the edges of the blocks. Serpentine flow is expected due to offsetting gaps. 66
Figure 3.6: Detailed illustration of the wiremesh assembly used in the thermal energy storage system: (a) Top view showing the combination of a 23-gauge galvanized steel hardware cloth with a 1/4 in. mesh size and a 14-gauge galvanized steel welded wire with a 5 cm × 10 cm rectangular mesh opening. (b) Side view of the layered arrangement featuring the coarser mesh sandwiched between two finer mesh cloths, providing a minimum opening of 3 mm, ensuring adequate fluid flow. This wiremesh setup enhances surface roughness, promoting turbulent flow, thus increasing the heat transfer coefficient and maintaining necessary gaps between composite plates to avoid fluid flow restriction. 67
Figure 3.7: Experimental setup to investigate the melt retention capacity of HDPE within polyester batting under external load. A polyester batting sample is saturated with paraffin oil (an analog for molten HDPE) and sandwiched between two glass slides (5 cm x 7.6 cm) with load applied to the top slide. A microporous paper tissue is positioned beneath the setup to collect any oil seeping from the batting. External weight is added on top. The lower portion shows a picture of the batting saturated with paraffin oil during testing. 72
Figure 3.8: Phase change media for the TES system (as synthesized). The composite is approximately 1.3 cm thick and 58 cm × 53 cm (23" × 21") on the sides, consisting of 10 layers of polyester batting and 9 layers of HDPE. The layers were subjected to high pressure and temperature (160 °C) till fully consolidated. The plates were formed without HDPE spreading to the edge. 75
Figure 3.9: Thermodynamic characterization of the pristine HDPE media performed through DSC. The calorimetry procedure involved heating and cooling the sample between 90°C and 140°C at a rate of 5°C/min. The DSC thermogram reveals a latent heat of fusion of 192 J/g for the HDPE, demonstrating a complete melting/solidification cycle with peak temperatures of 133.9 °C for melting and 120 °C for crystallization. The notable hysteresis between these temperatures, largely due to the rapid temperature change rate, is anticipated to be less pronounced under operational conditions. 76

Figure 3.10: Prototype composite media designed to minimize excess melt flow, consisting of low melt flow index HDPE and polyester batting. (Top) The composite immersed in glycerol pre-testing, showcasing a trimmed edge that reveals various layers of material composition and integration. This arrangement allows for testing potential HDPE extrusion under representative pressure (0.67 kPa). (Bottom) Post-thermal testing, subjected to approximately 600 Pa pressure and 150°C for 24 hours. Minor HDPE extrusion is observed on the cut edge, with intact sides effectively containing the HDPE within the composite structure. 78

Figure 3.11: Evaluation of composite media stability across numerous operational cycles in a thermal energy storage system. (a) Composite integrity post exposure to temperatures exceeding 100°C for 50+ hours, demonstrating robustness with no apparent signs of melt migration or consolidation. (b) Surface imprinting of the wiremesh on the composite does not compromise the surface or lead to HDPE leakage. The external polyester batting forms an additional barrier against leakage, absorbs molten HDPE, and mitigates edge flow, reinforcing the composite's operational reliability. 80

Figure 3.12: Relationship between applied external compressive stress and fraction of fluid volume retained in the saturated batting. Individual data points are measured retained volume ratio at different levels of applied external compressive stress. 81

Figure 3.13: Maximum deformation of a composite plate. The figure depicts a full plate, split into two halves, with the most pronounced deformation occurring near the center of the plate. . 82

Figure 3.14: Example discharge process in the thermal energy storage system. The graph depicts the temperature difference between the bed's inlet and outlet over time, with a constant glycerol mass flux of 146 g/m^2/s. A distinct temperature plateau during discharging marks the phase change of the storage media. The small fluctuation in the ambient temperature suggests a minimal impact on the computation of parasitic heat losses. 85

Figure 3.15: Cumulative energy extraction from the media during the discharge process shown in Figure 3.14. (a) Graph illustrates the time-dependent cumulative energy extraction since the start of retrieval, highlighting distinct phases of energy discharge: the rapid initial discharge due to hot fluid drainage and subsequent decrease in temperature difference, the consistent energy discharge rate corresponding to the release of latent heat, and the eventual deceleration marking completion of solidification. (b) Extracted energy is plotted against retrieval temperature, revealing the nuanced temperature change during the release of latent heat and the system's discharge efficiency. It is noted that approximately 79% of the maximum energy can be retrieved in about 67% of the full discharge time. . . 86

Figure 3.16: Evaluation of power extraction from the media during discharge process shown in Figure 3.14. (a) The power extraction plotted against time elapsed from the beginning of the discharge process, indicating an initial surge in power peaking at 76.1 W/kg within the first 0.86 hours. (b) The extracted power depicted against the retrieval temperature. 88
Figure 3.17: Relationship between the thickness of a slab and the total time it takes to melt completely, based on a composite thermal conductivity of 0.5 W/m/K and 1.31 W/m/K, a density of 0.835 g/cc, and a latent heat of melting of 192 J/g. The heat transfer is assumed to occur via direct contact with a fluid that is 1 °C higher than the fusion temperature of HDPE. . . 91
Figure 3.18: Schematic of continuous composite sheet forming for bulk-scale media production. The process begins with the stacking and preheating of alternating layers of polyester fibers and HDPE, followed by feeding the layers into a set of heated rollers maintained at temperatures optimal for HDPE melting but below polyester's melting point. The hot rollers, covered with PTFE sheets to prevent HDPE sticking, produce a consolidated composite, subsequently shaped using hot wire cutters. 95

Figure 4.1: Schematic of a steam accumulator with phase change materials (PCM) in water. 105
Figure 4.2: Illustration of specific energy as a function of temperature for a PCM. The specific energy varies linearly with temperature both before and after melting, showing a sudden increase at the melting temperature T_m. The calculations for specific energy are based on Equation (4.1). 107
Figure 4.3: Rectangular slab undergoing solidification, with a semi-thickness of L. Boundary conditions are established with a constant surface temperature T_0, less than the fusion temperature T_f, maintained at $x = 0$. A symmetric condition with zero heat flux is applied at $x = L$. The location of the melt interface, denoted as $s(t)$, indicates the progression of the solidification front from left to right in the positive x direction, beginning at $x = 0$ and culminating at the symmetric plane $x = L$. . . 109
Figure 4.4: Schematic of a solidification of a slab with constant heat flux at the surface. 113
Figure 4.5: conventional (a) and packed bed (b) steam accumulator, max steam output, HDPE composite. (c) fractional gain 118
Figure 4.6: Relation between total accumulated mass of steam over a specific surface area of the PCM and mass flux of steam with time of discharge for constant surface temperature. 123
Figure 4.7: Melt time as influenced by the thickness of the PCM slab for varying heat flux values. 125
Figure 4.8: Evolution of steam temperature and its associated output pressure during discharge time. 126

Figure 4.9: Relation between the total accumulated mass of steam per unit surface area of the PCM and the heat extracted with respect to the time of discharge, under conditions of constant surface heat flux 127
Figure 4.10: Relation between total heat extracted versus the output pressure. 128
Figure 4.11: Variation of saturation pressure (kPa), latent heat of vaporization (kJ/kg), and saturation temperature (°C) of water between 100 °C to 160 °C. The data for saturation pressure is fitted using the Antoine equation (Eq. 4.24) with parameters A = 7.0361, B = 1631.9818 °C, C = 224.4498 °C. The root mean squared error of the fit is 0.023. The data for latent heat of vaporization is also curve-fitted (Eq. 4.25) with parameters A_1 = -3.5458 kJ/(kg °C), B_1 = -2718.2939 kJ/kg, C_1 = 4.1282 °C. The corresponding root mean squared error is 0.257 kJ/kg. 129
Figure 4.12: Cost vs. volume for steam flash tanks. Blue points represent horizontal cylindrical tanks, while red points represent vertical cylindrical tanks. The lines of best fit illustrate the linear relationship between volume and cost for each tank type. Units for volume and cost are liters and USD, respectively. . 131
Figure 4.13: Relationship between the volume (in liters) and the thermal energy storage (TES) cost per kilogram (in USD) for horizontal tanks. The red curve represents the best-fit model, cost/kg = 7.40 + 2851.15/Vol (L), which closely fits the observed data with an R^2 value of 0.998 and a Root Mean Square Error of 0.869. The TES cost consist of the cost of the PCM in it and the tank. 134
Figure 4.14: Fractional savings achieved using a TES system coupled with a heat pump versus a high-power heat pump alone. The capital costs of the high-power heat pump are set at (a) 250 USD/kW and (b) 1000 USD/kW. Savings are calculated for a range of duty cycles (from 0.1 to 0.3) and operational durations, as per Eq. 4.36. 136

LIST OF TABLES

Table 2.1: Thermo-physical properties of HDPE and glycerol. 21
Table 2.2: Comparison with existing HDPE latent heat TES systems . . 54

Table 3.1: Media Size and weight 64
Table 3.2: Thermo-physical properties of HDPE and glycerol. 69

Table 4.1: Selected PCMs with Melting Points Below 170 °C 104
Table 4.2: Steam generation capacity (kg) per m^3 for standard steam accumulator 116
Table 4.3: Steam generation capacity (kg) per m^3 for enhanced steam accumulator utilizing a 50 % porous packed bed of PCM composites with HDPE as the primary storage medium, at various operating pressures (bar g). 117
Table 4.4: Fractional increase in steam generation achieved by using the packed bed method compared to a traditional steam generator. 117
Table 4.5: Steam generation capacity (kg) per m^3 for standard steam accumulator 120
Table 4.6: Steam generation capacity (kg) per m^3 for enhanced steam accumulator utilizing a 50 % porous packed bed of PCM composites with PP as the primary storage medium, at various operating pressures (bar g). 121
Table 4.7: Fractional increase in steam generation achieved by using the packed bed method compared to a traditional steam generator. 121
Table 4.8: Comparison of thermal energy storage tanks. "Vol (Ga)" and "Vol (L)" indicate the volume in gallons and liters, respectively. "Cost (USD)" is the flash tank cost, while "TES Cost" also includes the cost of the Phase Change Material and flash tank. "TES Cost/kg" denotes the cost of Thermal Energy Storage per kilogram of PCM. "Orientation" describes whether the tank is horizontal or vertical, along with its shape. 132
Table 4.9: Fractional savings in dollars based on a heat pump capital cost of 250 USD/kW. 134
Table 4.10: Fractional savings in dollars based on a heat pump capital cost of 1000 USD/kW. 135

ACKNOWLEDGEMENTS

I stand here at the end of this academic journey, humbled by the multitude of individuals who have helped pave the way for my successes.

First and foremost, my deepest gratitude goes to my PhD advisor, Prof. James Palko. Over the last five years, he has provided immeasurable encouragement, unwavering support, and invaluable guidance. Without his wisdom and patient mentorship, this journey would have been far more challenging.

Equally significant has been the companionship and support of my lab mates. The culture of collaboration has not only enriched my research but also made the experience more fulfilling. Thank you for the valuable research discussions, assistance, and emotional support throughout this period.

My sincere appreciation extends to my PhD committee members, whose critical comments and insightful suggestions have played an indispensable role in shaping this thesis and my understanding of the field.

A thriving academic pursuit is often buoyed by a strong personal support network. In this regard, I am endlessly grateful to my parents. Their ceaseless encouragement has been my anchor and their faith in me, my motivation.

To my wife, who has been my rock throughout this rigorous journey, I owe a debt of gratitude. Your support, both emotional and practical, has been nothing short of a blessing.

I must also acknowledge my previous teachers, whose belief in my capabilities spurred me to undertake this ambitious endeavor. You lit the initial spark that led to this flame.

Last but by no means least, I thank my friends. Your unconditional love and unwavering support have been my lifeline during the most challenging times. You have each, in your own way, contributed to this milestone.

VITA

2008	B. E. in Mechanical Engineering, Indian Institute of Engineering Science and Technology, Shibpur, India
2017	M. S. in Mechanical Engineering, Rensselaer Polytechnic Institute, Troy, NY (**GPA:** 3.8)
2023	Ph. D. in Mechanical Engineering, University of California, Merced, CA (**GPA:** 4.0)

FELLOWSHIPS AND AWARDS

Dan David Solar Fellowship (Oct 2019), University of California, Merced

Fred and Mitzie Ruiz Fellowship (Oct 2020), University of California, Merced

ME Bobcat Graduate Fellowship (June 2019), University of California, Merced

ME Bobcat Graduate Fellowship (June 2020), University of California, Merced

ME Bobcat Graduate Fellowship (June 2021), University of California, Merced

RELEVANT JOURNAL PUBLICATIONS

Roy, Souvik, Gerardo Diaz, Roland Winston, and James W. Palko. ”Packed bed thermal energy storage system using form-stable high-density polyethylene.” Applied Thermal Engineering 218 (2023): 119209

RELEVANT CONFERENCE PRESENTATIONS

Souvik Roy, Roman Giglio, Ruben Juan Soto, Christian Lopez Garcia, James Palko, “Polymer Composite for Thermal Energy Storage,” InterPACK 2020 Oct. 27 – 29, 2020. **Online Presentation, self**

Souvik Roy, Roman Giglio, Ruben Juan Soto, Christian Lopez Garcia, James Palko, “Polymer Composite for Thermal Energy Storage,” IMECE 2021 Nov 1 – 5, 2021.
Online Presentation, self

Souvik Roy, Gerardo Diaz, Roland Winston, James W. Palko, “Shape Stable Polymer Composites for Medium Temperature Thermal Storage: Detailed Heat Transfer and Scale Up”, IMECE 2022, Columbus, Ohio: Oct 30 - Nov 3, 2022.
Podium Presentation, self

ABSTRACT OF THE DISSERTATION

Polymer Composites for Latent Heat Thermal Energy Storage

by

Souvik Roy
Doctor of Philosophy in Mechanical Engineering

University of California Merced, 2023

Prof. James Palko, Advsior

Energy storage is a pressing need throughout a range of applications. While electrical storage systems, such as for renewable power intermittency mitigation and electric vehicles, often receive considerable attention, the potential of thermal energy storage is equally significant. Storage of thermal energy is an important element in energy management. Thermal energy can be stored directly as sensible heat corresponding to a change in temperature of the storage media, latent heat corresponding to a change of phase in the storage media, or as heat of a chemical reaction in the media. Latent heat storage systems have significant advantages in terms of their energy density, exergetic efficiency, and practicality.

The focus of this thesis is a multi-scale examination of high-density polyethylene (HDPE) composites as potential phase change materials in latent heat thermal energy storage systems, specifically in a packed-bed setup suited for medium-temperature applications requiring heat below 125°C and involving direct contact heat exchange between the phase change materials and the heat transfer fluid.

The research commences with a bench-scale experimental evaluation, providing an in-depth thermal characterization of an HDPE composite fortified with surface-treated glass fiber fillers and coated with a thin layer of epoxy resin. This media is stable over repeated melting and solidification cycles and shows excellent thermal capacity, with more than 160 kJ/kg attributable to latent heat. The system can be charged and discharged at relatively high rates, e.g. > 100 W/kg. The performance of direct contact heat exchange between the storage media and heat transfer fluids, such as glycerol, flowing over the media is characterized. The performance study includes effects of the mass flow rate of the heat transfer fluid, the charging and the discharging temperature, and the initial

bed temperature of the porous packed bed TES system. Significant advantages of this TES system are excellent energy density with high exergetic efficiency averaging approximately 79% (i.e. low temperature differences between charge and discharge). The direct contact heat exchange mode improves heat transfer performance, reducing the transport component of $\Delta T_{c/dc}$ while eliminating the costs associated with the heat exchanger. Experimental characterization and models of conjugate heat transfer processes in a bed of storage media are presented. The simple construction also leads to a compact system for easy transportation and installation on site. The approach presented offers opportunities to enhance the use of thermal storage in medium temperature applications (e.g. a charge/discharge operational range between 120 °C – 140 °C).

The thesis transitions to a pilot-scale experimental assessment, introducing another novel composite consisting of HDPE and polyethylene terephthalate (polyester) fibers. Synthesis of this composite and its implementation in a pilot-scale thermal energy storage system is presented. Complexity associated with previous media composition and manufacturing is reduced. This refined media has improved manufacturability and lower cost of components. A strategy for in-house production of the composite and its installation in a media containment vessel is introduced and discussed. Thermodynamic characterization, including determination of latent heat of fusion using differential scanning calorimetry, reveals that the composite exhibits a thermal capacity with a latent heat of melting value of over 190 kJ/kg for HDPE. The thermal energy storage system, tailored for medium-temperature processes requiring heat below 120 °C, leverages the novel composite as a phase change material within a strategically designed containment system. This design offers efficient heat storage, promoting maximum capacity and heat transfer while minimizing parameters such as porosity, liquid volume, cost, and heat loss. Results indicate that the system can be discharged at rates exceeding 70 W/kg and maintains stability during extended thermal testing. This study also examines the composite's deformation, long-term stability, and leakage potential. The energy storage and discharge power, observed through bulk calorimetry tests, rely significantly on latent heat, confirming the composite's high performance. In conclusion, the composite shows potential for use in large-scale thermal energy storage for medium-temperature applications, with an operational charge/discharge range between 120 °C – 140 °C.

The final component of this work presents an analytical analysis of steam generation in pressure-drop steam accumulators with the incorporation

of phase change material, in a packed bed configuration. The work employs a thermodynamic framework, featuring equations to quantify steam generation capacities under different working pressures. A quasi-steady approximation is also utilized to focus on latent heat effects during phase changes. The system's performance is assessed under two operational contexts—constant pressure output and constant thermal energy output. The study identifies conditions under which the phase change material-enhanced, packed bed, steam accumulator's performance surpasses that of a conventional steam accumulator, offering insights that are backed by derived equations and graphical representations.

Through this investigation that incorporates bench-scale testing, pilot-scale validation, and analytical modeling, the thesis provides a comprehensive understanding of the key performance metrics, operational constraints, and areas requiring further research, with respect to the use of polymeric composites as phase change materials in latent heat thermal energy storage systems for medium-temperature applications.

Chapter 1

Thermal Energy Storage

1.1 Introduction

Recent projections predict that the primary energy consumption will rise by 48% in 2040 [1]. The depletion of fossil resources and its negative impact on environment in terms of CO_2 emissions, a primary cause of global warming, is a leading reason for the shift towards sustainable energy sources. One important part of sustainable energy technology systems implementation is development of efficient and sustainable methods of storing energy. Thermal energy storage (TES) technology is a way of storing thermal energy in a storage medium by heating. The stored energy is retrieved later by cooling of the media. This can have a lot of applications for heating and cooling at a range of temperatures [2] and even power generation. As per the recent reports from Global Industry Analysts, Inc, "The global market for Thermal Energy Storage (TES) estimated at USD 4.1 Billion in the year 2020, is projected to reach a revised size of USD 6.2 Billion by 2027, growing at a compound annual growth rate (CAGR) of 6.3% over the analysis period 2020-2027... The Thermal Energy Storage (TES) market in the U.S. is estimated at USD 1.4 Billion in the year 2020. The country currently accounts for a 34.22% share in the global market... In the global Phase Change Material (PCM) segment, USA, Canada, Japan, China and Europe will drive the 7% CAGR estimated for this segment" [3]. TES systems have potential for high efficiency with the ability to recover, for example, over 98% of stored energy [4]. Depending on design, they can be charged and discharged over either short or long durations of time. Finally, they have potential to provide heat with relatively low incremental cost compared to the original cost of generating the thermal energy. Following extensive research in this field, some applications where thermal energy storage has gained recognition are effective peak load balancing, electricity generation during non-peak hours, waste heat recovery, energy efficient buildings and electronics cooling.

1.2 Literature Review

Significant research has been dedicated to comprehensive study and review of thermal energy storage systems. Sarbu and Sebarchievici [1] did a comprehensive review of thermal energy storage. Sharma *et al.* [5] reviewed thermal energy storage with phase change materials for different applications. Tao *et al.* [6] reviewed phase change materials and their performance enhancement method for latent heat storage system. Fallahi *et al.* [7] reviewed solid-solid phase change materials for thermal energy storage. Zhang *et al.* [8] reviewed thermal energy storage and its practical applications. Cunha *et al.* [9] reviewed phase change materials for thermal energy storage systems regarding low and medium operating temperature applications. Xu *et al.* [10] reviewed application of phase change materials for thermal energy storage in concentrated solar thermal power plants. Pielichowska *et al.* [11] reviewed phase change materials for thermal energy storage systems. Tian and Zhao *et al.* [12] reviewed thermal energy storage in solar thermal applications. Regin *et al.* [13] reviewed heat transfer characteristics of thermal energy storage system using PCM capsules. Kenisarin and Mahkamov *et al.* [14] reviewed solar energy storage using phase change materials in the range of temperatures from 120 to 1000 ℃. Khudhair and Farid *et al.* [15] reviewed energy conservation in building applications with thermal storage by latent heat using phase change materials. Farid *et al.* [16] reviewed phase change material and its application in thermal energy storage system. Zabla *et al.* [17] reviewed the heat transfer analysis of a thermal energy storage system using phase change materials. Liu *et al.* [18] reviewed storage materials and thermal performance enhancement techniques for high temperature phase change thermal storage systems.

1.3 Classification of Thermal Energy Storage

Thermal energy storage works on the principle of change in internal energy of a material. The common approaches of storing heat are through addition of sensible heat, latent heat and thermo-chemical or combination of these. Fig. 1.1 [19] gives an overview of the different techniques of storing thermal energy. In

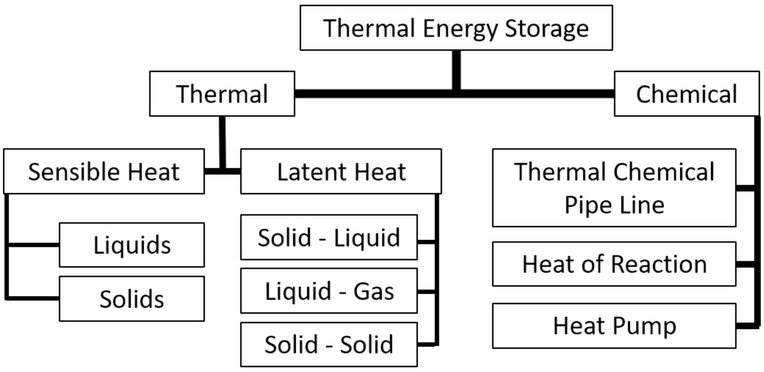

Figure 1.1: Types of TES

sensible heat storage (SHS), thermal energy is stored by raising the temperature of a solid or liquid. The amount of heat stored depends on the specific heat of the medium, the temperature change and the amount of storage material. Water having a high specific heat of 4.2 kJ/kg.K and being low cost material is an example of very good SHS liquid. Above 100 °C, oils for eaxmple, Caloriea HT43 (sp. heat: 2.2 kJ/kg.K), engine oil (sp. heat: 1.88 kJ/kg.K), glycerine (sp. heat: 2.43 kJ/kg.K), etc. are used. For air heating applications rock bed type storage materials (sp. heat: 0.88 kJ/kg.K) are used [5]. Whereas, latent heat storage (LHS) materials stores thermal energy by absorbing the latent heat of melting and latent heat of vaporization when a storage material undergoes a phase change from solid to liquid or liquid to gas respectively. LHS materials provide high-energy storage density at constant temperature corresponding to its phase-transition temperature. Phase change can be in the following form: solid–solid, solid–liquid, solid–gas, liquid–gas and vice versa. In solid–solid transitions, heat is stored during crystalline transformation in the material [20]. Although the volume change compared to other phase transitions is very small, these transitions generally have a small amount of latent heat. The solid-gas and liquid-gas transition involves very high latent heat of sublimation and vaporization, respectively, but the large volumes changes in phase transition rule out their potential utility in thermal storage systems [21]. Whereas, Solid–liquid phase change involve decently high latent heat of fusion and involve only a small change (of order of 10% or less) in volume. Solid–liquid transitions have proved to be economically attractive for use in thermal energy storage systems. Thermo-chemical systems absorb and release energy by reversible chemical reactions through making and breaking molecular bonds. The heat stored depends on the amount of storage material, the endothermic heat of reaction, and the extent of conversion.

1.4 Energy Sources for Thermal Energy Storage Systems

While the previous section emphasized the methods by which thermal energy can be stored, understanding the origins of this energy is crucial to the design and implementation of effective storage systems. Just as there are various mechanisms for storing heat, there are also a myriad of sources from which this thermal energy is derived. These sources can vary based on the temperature ranges desired, the scale of the application, and the local availability of resources. Some of the main sources of energy for TES systems are as follows.

1. **Concentrated Solar Power (CSP)**: CSP systems harness energy of sun as a heat source. They can be categorized into three main types: linear concentrators, dish/engine systems, and power tower systems [22]. Linear concentrator systems have two prominent variations: parabolic trough systems and linear Fresnel reflector systems. In parabolic trough systems, sunlight is focused onto a focal line by a parabolically shaped mirror, where a receiver is strategically placed [23, 24]. Linear Fresnel reflector systems feature one receiver tube positioned above multiple mirrors, offering these mirrors enhanced flexibility in tracking the sun [25]. Both systems employ a receiver that includes an evacuated glass tube with an inner absorber tube. As a heat transfer fluid flows through the absorber tube, it captures and conveys the heat away from the collector, either for storage or direct use in heating processes. Meanwhile, a power tower system utilizes a vast array of flat sun-tracking mirrors, known as heliostats [26, 27]. These heliostats direct and concentrate sunlight onto a receiver located atop a tower, where a heat-transfer fluid gets heated within the receiver.
2. **Electricity:** A crucial component of many solar heating systems is the backup system, which becomes indispensable during prolonged cloudy spells. Electric power, derived either from resistance heating or powering heat pumps, serves as a suitable backup. Utilizing electricity during off-peak times can be advantageous due to potentially reduced rates. Storing the heat generated from electricity in the thermal storage system during these off-peak intervals, for deployment during peak times, might not only be feasible but also economically beneficial [28].
3. **Others:** Our environment is teeming with potential sources of thermal energy, even if many are of relatively low quality or temperature. To

harness these efficiently, the integration of a heat pump can be invaluable [29, 30, 31]. These sources encompass ambient air, geothermal heat from the ground [32], water bodies like lakes or rivers, and waste heat from industrial processes [33, 34]. Additionally, nuclear energy, through nuclear reactors, provides a consistent and significant source of thermal energy as a byproduct of the nuclear fission process [35, 36]. Leveraging the vast thermal mass of the air, ground, water bodies, or the heat generated from nuclear reactors can yield a substantial amount of thermal energy, making this approach especially potent in warmer regions or areas with substantial industrial or nuclear activity.

1.5 Latent Heat Storage Materials

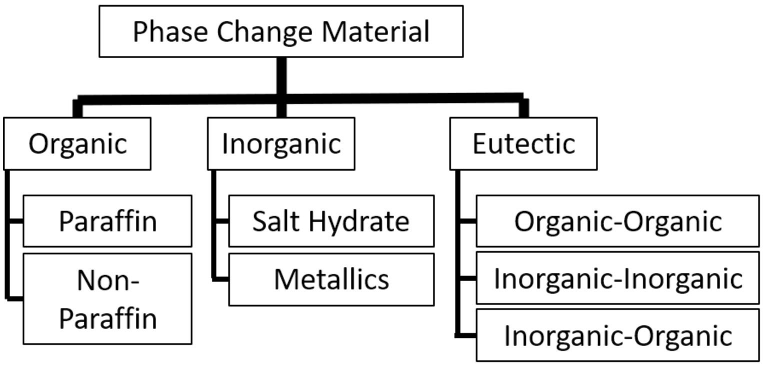

Figure 1.2: Types of PCM based on chemical composition.

The main focus in this thesis is latent heat thermal energy storage systems. The materials that undergo solid-liquid and vice-versa phase transitions are called Phase change material (PCM). Initially, PCMs perform like SHS materials, their temperature rises as they absorb heat. But unlike SHS materials, PCM absorbs and release heat at a nearly constant temperature during phase change. They store 5–14 times more heat per unit volume than sensible storage materials such as water, masonry, or rock. An ideal LHS material should posses the following properties [21], [37]: The liquid-solid phase transition temperature of the material should at least match the operating temperature of the heating-cooling application. The material with high heat of fusion and very less melting-solidification hysteresis is desired. Material with high thermal diffusivity will help faster charging or discharging of the media. Media must have high density to allow a smaller size of storage container. Small volume changes on phase transformation and small vapor pressure at operating temperatures is a must to avoid complex containment design. The material must be thermally stable to allow numerous charge-discharge cycle. The PCM should be chemically stable or inert to its surroundings, and it should be non-toxic, non-flammable and non-explosive for safety. Finally, low cost and large-scale availability of the phase change materials is also very important. Based on chemical composition, PCMs can be classified into organic, inorganic and eutectic types as shown in Fig. 1.2. While most of the PCM do not meet all of the criteria required for an adequate storage media as discussed, there are a large number of materials, which can be identified as PCM based on its melting temperature and latent heat of fusion.

Cardenas and Leon [38] summarizes the comprehensive thermophysical properties of inorganic salt compositions and metallic alloys, which could potentially be used as storage media in a high temperature (above 300 °C) LHS system. Solid-liquid PCM may flow and leak during the application; thus specially designed devices/containers are an option to prevent leaking. But the additional thermal resistance between the devices/containers and PCMs will diminish the heat transfer and also increases the operational costs. To overcome this problem, PCMs encapsulated with polymeric materials (e.g., polymethyl methacrylate [39], [40], polyethylene oxide [41], [42], and styrene maleic anhydride copolymer (SMA) [43]) have been investigated; these PCMs are termed as the form-stable PCMs, they are cost effective and maintain a stable shape upon melting.

HDPE has been extensively studied as a material for the encapsulation of PCM, rather than a thermal energy storage material. Hong and Xin-shi, [44] prepared a form-stable PCM of paraffin as dispersed PCM and high density polyethylene (HDPE) with different melting index as supporting material. Inaba and Tu [45] investigated the latent heat storage properties and thermal conductivity of paraffin/HDPE composite as form-stable PCM and Sarı, [46] suggested inclusion of 3% (by wt) expanded graphite as promising form-stable PCM for LHTES applications. Lee and Choi [47] studied the durability of HDPE (high and low)/paraffin blends as energy storage materials by investigation of the seepage behavior of paraffin. Cai *et al.* [48] choose high density polyethylene (HDPE) as the supportive material to encapsulate paraffin to prepare the paraffin/HDPE form-stable PCM using different methods. Cai *et al.* [49] prepared thermal energy storage phase change materials (PCM) based on paraffin/high density polyethylene (HDPE) composites by using twin-screw extruder technique. Huang *et al.* [50] studied microstructure and thermal properties of cetyl alcohol/high density polyethylene composite phase change materials with carbon fiber as shape-stabilized thermal storage materials. Krupa *et al.* [51] synthesized phase change materials based on low-density polyethylene(LDPE)/paraffin wax blends.

Some studies use polymers as PCMs for latent heat TES system. Alkan *et al.* [52] synthesized a form stable paraffin/polypropylene composite for thermal energy storage using paraffin as the PCM and dispersed it into the polymer (polypropylene) matrix. Among organic materials, High density polyethylene (HDPE) as a PCM present good thermal properties, chemical stability and low price. It has a high degree of crystallinity, is a non-polar thermoplastic resin, nontoxic. It has a good chemical stability, with a melting point above 125 °C. Conventional HDPE presents a latent heat between 210 and 180 J/g [53]. However, its thermal conductivity is around 0.3 W/mK [54]. HDPE has been considered as PCM by a few authors. Kanimoto *et al.* [55], Abe *et al.* [56] reported direct contact latent thermal storage units using cross-linked form-stable HDPE. Zauner *et al.* [57], [58] used 170 kg HDPE in a fin-tube heat exchanger and characterized its energy capacity, power characteristics and temperature profiles using a thermal oil test rig. They performed 30 melting and crystallization cycles above 100 °C for more than 140 hours. Post experiment they found thin layer of degradation on PCM surface most likely related to thermo-oxidative degeneration of HDPE. Salyer and Davison [59] synthesized cross-linked HDPE using electron beam for phase-change thermal-energy storage. Inaba and Li [60] did an experimental investigation of latent thermal energy storage characteristics of surface cross-linked form-stabilized HDPE pellets as a phase change material (PCM), using pool boiling and condensation of an ethylene glycol–water solution. Yang *et al.* [61] formulated and characterized a novel composite, a recycled HDPE/graphite mixture, for medium temperature thermal energy storage application. Few people for example Kanimoto *et al.* [55], Abe *et al.* [56], Salyer and Davison [59], Inaba and Li [60] have cross-linked HDPE surface to form a shape-stable PCM.

1.6 Phase Change Material Performance Enhancement

One way to enhance performance for LHS system is increase the thermal conductivity of the PCM i.e. to decrease PCM side thermal resistance.

In recent years, improving the thermal performance of PCM has received great attention. Several studies report enhancement of the overall thermal conductivity of the PCM. Jagadheeswaran and Pohekar [62] summarized the performance enhancement techniques where the influence of enhancement techniques on the thermal response of PCM in terms of phase change rate and amount of latent heat stored/retrieved has been addressed. Fan and Khodadadi [63] reviewed the experimental/computational studies to enhance the thermal conductivity of PCM. Liu *et al.* [64] also reviewed the experimental and theoretical methods to enhance PCM thermal conductivity and the thermal conductivity inserts/ additives. Ibrahim *et al.* [65] reviewed the heat transfer enhancement of phase change materials for thermal energy storage applications. Ma *et al.* [66] worked on nano-enhanced phase change materials for improved building performance. Amaral *et al.* [67] reviewed using carbon nanostructures for performance enhancement in phase change materials.

One way to increase thermal conductivity of PCM is to use a porous media with high thermal conductivity which will absorb the PCM in its pores. Metal foams such as copper [68], [69], [70], [71], [72], nickel [69], [73] and aluminum foams [74], expanded graphite foams [75], [76], [77], [78], [79], [80], [81], [82], [83], [84], [85], [86], [87] are used as the porous supporting material. Nanomaterial additives with high thermal conductivity and chemical compatibilty with the PCM are dispersed in the PCM uniformly to form a stable composite. The carbon nanomaterials such as multi-walled carbon nanotubes (MWCNT) [88], [89], [90], [91], [92], [93], [94], [95], [96], single-walled carbon nanotubes (SWCNT) [88], graphite [90], [92], [94], [97], [98], [61], graphene [92], [94], [95], [99], [100] and metal oxide nanoparticles [101], [102], [103] or metal nanoparticles [104] are commonly used as additives to enhance PCM thermal conductivity.

1.7 Packed Bed Thermal Energy Storage Systems

Flow and heat transfer in packed beds, including random and structured packings, were extensively investigated by many researchers. Bedecarrats *et al.* [105], [106] studied the performance of a packed bed phase change energy storage system using spherical capsules. They did both experimental and numerical studies. Cascetta *et al.* [107] worked on a sensible heat thermal energy storage system with alumina beads as the energy storing medium and air as the heat transfer fluid. Wu *et al.* [108] investigated the dynamic thermal performance of a molten-salt packed-bed thermal energy storage (TES) system using capsules filled with high-temperature phase change material (PCM). Singh *et al.* [109] investigated flow and heat transfer in packed beds, including random and structured packings. Coutier and Faber [110] did a numerical study on packed bed with rocks as the sensible energy storage medium for air based solar systems. Kanimoto *et al.* [111] did a numerical analysis of heat transfer for a latent thermal storage unit using form-stable high density polyethylene.

1.8 Application

There are a lot of commercial and industrial applications of a thermal energy storage system. Pintaldi *et al.* [112] reviewed thermal energy storage technologies and control approaches for solar cooling system. They mainly focused on types of thermal storages used in solar cooling applications, with emphasis on higher temperatures (> 100 °C). Tian and Zhao [12] compiled various types of research in solar collectors and thermal energy storages used for solar thermal applications. Joybari *et al.* [113] compiled a review on PCM for cold storage for the application of domestic refrigeration, i.e., evaporator side only. The study performed by Oró *et al.* [114] also covered ice storage and air conditioning separately. TES systems are used particularly in buildings and in industrial processes. Advantages of using TES in an energy system include an increase in overall efficiency and better reliability, and it can lead to better economics, reductions in investment and running costs, and less pollution of the environment, i.e., fewer carbon dioxide (CO2) emissions [115].

One major application that we will focus later is the application of form stable phase change materials in steam accumulators. Steam accumulators use sensible heat storage in pressurized saturated liquid water[116]. Using thermal energy storage to generate additional steam is not new. Steinmann and Eck [117] integrated latent heat storage material with steam accumulator for increased output of steam. Medrano *et al.* [118] also did few case studies on the application of high-temperature thermal energy storage for power generation, direct steam generation and steam accumulators. Bai *et al.* [119] integrated steam accumulator and a sensible heat storage unit to produce super-heated steam.

1.9 Research Motivation

Within the broad landscape of Thermal Energy Storage (TES), various methods have been developed to harness and store energy efficiently. The flowchart (Figure 1.3) provided offers a structured view of this landscape. The three primary categories of TES are Sensible Heat Storage, Latent Heat Storage, and Thermochemical Heat Storage.

My research is concentrated on Latent Heat Storage, particularly focusing on the storage of thermal energy as latent heat of fusion. The Phase Change Material (PCM) is crucial in this context. While PCMs can be solid-solid, liquid-vapor, or solid-liquid, my attention was on the widely utilized solid-liquid PCM. These materials are esteemed for their capacity to store high-density energy with minimal volume change during phase transitions.

The selection criteria for PCMs often involve their operating temperature range, which can be categorized into low, medium, or high. My choice was the medium temperature range. Another vital classification of PCMs is based on the types of materials they are composed of, either organic or inorganic. My work utilized organic materials, more specifically, thermoplastic polymers.

The design intricacies of TES systems involve decisions on how heat exchange occurs with the Heat Transfer Fluid. I opted for a direct-contact heat exchange mechanism. As part of this endeavor, the challenge was to create shape-stabilized PCM. This stabilization can be achieved in various ways, such as surface cross-linking the polymers, encapsulating them, or reinforcing with fillers. I leaned towards reinforcement with fillers, and rather than employing high thermal conductivity fillers as some researchers have, I incorporated fillers with lower thermal conductivity. This approach was influenced by considerations of cost-effectiveness and material availability.

Delving deeper, in the first phase of my research, glass fibers were the reinforcement of choice. The second phase incorporated polyester fibers in the form of partially bonded batting. The third segment of my study took a slightly different route, exploring the potential of a liquid-vapor PCM, specifically water, in a pressure drop steam accumulator and integrating the PCMs described in the first two phases. This was an exploration into formulating a hybrid system that potentially enhances steam generation performance.

Given this structured approach, my research aims to provide insights on the heat transfer characterization in a packed bed system at the bench scale and intends to upscale this to a more extensive system integrated with a solar collector. The behavior of heat transfer and flow in both scales, as well as the further application of PCM in steam accumulators, remain areas of keen interest and study.

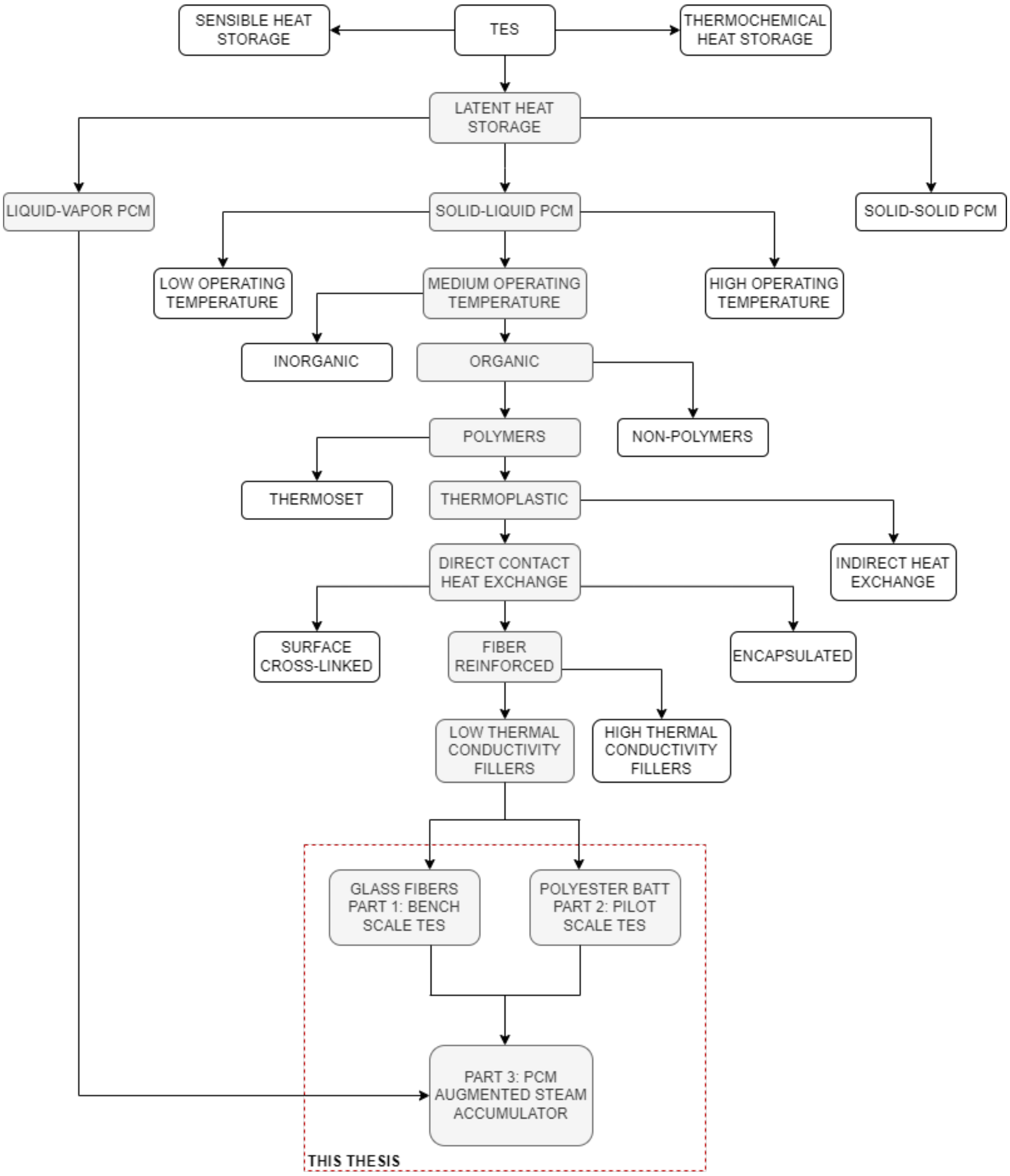

Figure 1.3: Thesis within the broad Thermal Energy Storage landscape

1.10 Summary of Research Objectives

The principal aim of this thesis is to investigate the feasibility and efficiency of using high-density polyethylene composites as phase change materials for latent heat thermal energy storage systems. This was contextualized within the scope of medium-temperature applications that require heat below 120°C. The objectives were further divided into the following key areas:

1. **Investigation of High-Density Polyethylene Composites**: This objective entails a comprehensive bench-scale evaluation of high-density polyethylene composites, examining their thermal and mechanical properties. The

initiative aligns with the ambition to utilize solid-liquid PCMs in energy storage applications. It acknowledges the challenges and design solutions pertinent to the identification of the core material, the thermal resistance, and the form stability of the composite. Following this, there is an emphasis on transitioning from a bench-scale thermal energy storage system to a pilot-scale setup. The goal is to address and curtail manufacturing complexities and associated costs from the bench-scale setup, ensuring there is no impact on the overall efficacy of the system, including the energy and power it delivers and the forms-stability of the PCM composite.

2. **Efficacy in Steam Production via PCM Augmented Steam Accumulators**: Frequently, steam can be required for industrial purposes at high instantaneous flow-rate for short duration of time. In such applications, a steam accumulator which can store and provide clean dry steam instantaneously at high temperature and pressure, to meet peak demand, is commonly used. Conventional steam accumulators store energy via the sensible heat of saturated water. When pressure drops, a portion of this water flashes to steam, allowing for high instantaneous steam flow rates for brief periods, evening out peak loads. In contrast, augmented accumulators utilize PCMs to achieve a higher energy density. This improved energy density makes augmented accumulators more compact and efficient, providing a superior solution for managing peak loads in steam systems. Therefore, the benefits of this design include a smaller tank size, reduced costs, and enhanced safety. However, these come with some trade-offs. The energy release is slower, the discharge rate is limited, and the long-term durability of PCMs in steam accumulators is still uncertain. This study aims to:

   - Examine and contrast the maximum steam storage capacity per unit volume of a conventional steam accumulator and a packed bed steam accumulator. This is studied thermodynamically, considering operations transitioning from a high charging pressure to a lower discharging pressure.
   - Using analytical thermodynamic models to evaluate the maximum steam storage capacity and develop the kinetic behavior of the augmented system for two different cases: a constant pressure steam output and a constant rate of heat extracted during discharge. The purpose of this model is to enhance the understanding of the dynamics

occurring in heat transfer and steam generation within the system.

- Investigate the behavior of a Thin PCM, where heat transfer is predominantly 1-dimensional. Utilize approximate solutions, such as the quasi-steady approximation, in the absence of exact solutions to understand PCM behavior during solidification, including solidification rate and temperature distribution changes within the slab.

3. **Economic Analysis of Thermal Energy Storage Integration with Heat Pumps**: The main objective here is to evaluate the economic aspects of integrating TES systems with heat pumps. There's a substantial high capital cost per KW for heat pumps, and this study aims to quantify how the capital cost savings achieved by opting for a low-power heat pump can be effectively reinvested into a TES system, optimizing resources.

1.11 Structure of the Thesis

This thesis is organized as follows. Chapter 1 briefly described TES systems, challenges faced, some prior work done to address these issues and the novelty of this work. Chapter 2 describes work done toward the synthesis of a form-stable fiber-reinforced HDPE composite PCM and characterization of the heat transfer performance of a bench scale TES packed bed system using these PCM composites. Chapter 3 presents the upscaling of the bench scale packed bed system to a large scale system. Another novel shape-stable HDPE composite composition and synthesis approach is presented. Chapter 4 discusses the application of form-stable phase change materials in steam accumulators. Lastly Chapter 5 concludes this work.

Chapter 2

High Density Polyethylene Composite as Phase Change Material for Latent Heat Thermal Energy Storage - Bench-Scale Experimental Study

2.1 Introduction

As detailed above, this work focuses on Thermal Energy Storage (TES) systems using phase change material (PCM) to store latent heat at the appropriate operating temperature. I investigated two PCM chemistries, alkali metal nitrates and high-density polyethylene. Shaped stabilized nitrate media synthesized via absorption in an inert matrix was considered, but due to the highly oxidizing nature of nitrates, this approach was not pursued further due to incompatibility with many working fluids and the difficulty in adequately isolating the media.

Polyethylene storage media is the focus of this thesis. Highly crystalline, high density polyethylene (HDPE) pellets are stabilized via a combination of reinforcement with an inert filler and partial coating or encapsulation. This approach yields media with excellent latent heat capacity, mechanical and thermal stability, and compatibility with heat transfer liquids such as propylene glycol and glycerol and was selected for implementation.

2.2 Methods

2.2.1 Media Synthesis

The PCM used here consists of fiber-reinforced HDPE composite. The following section describes the constituent materials and detailed process of manufacture.

MATERIALS

To prepare the composite, virgin HDPE resin (Petrothene Homopolymer, LM60- 0700) was purchased with better than 99.5% purity from Equistar Chemicals, LP (Houston, Texas). The material obtained was in the form of biconvex, disc shaped pellets. From the HDPE technical data sheet, the specific gravity at ambient condition is 0.96 [120]. For the composite filler material, quarter-inch chopped glass fibers was procured from Fibre Glast Developments Corporation (Part #30 – $\frac{1}{4}$" Chopped Glass Fibers). As per the safety data sheet, this product includes organic surface treatment, but the composition is unknown. Loctite Epoxy Marine (item # 1919324) obtained from Henkel Corporation was used for media coating. This is a filled two-part epoxy. For glass fiber treatment, 97% concentrated octyltrichlorosilane from Acros Organics was acquired.

SAMPLE PREPARATION

Glass fiber reinforced, epoxy coated HDPE composite was synthesized using a custom-made high shear mixer. Synthesis procedures are as follow:

Glass fiber treatment: 5% (by volume) silane coupling agent solution was prepared by dissolving 97% concentrated octyltrichlorosilane into hexane. Quarter inch chopped glass fibers were immersed, as received, into the 5% silane solution. For every 1 g of glass fibers, approximately 2 ml of solution was used. The mixture was rolled for 24 hours at ambient conditions, after which the treated fibers were rinsed with pure hexane. The treated glass fibers were then immersed in hexane for 24 hours and rinsed with hexane a final time. The glass fibers were dried in air at room temperature, then kept under vacuum at 100 °C for 12 hours.

Filling: A custom-made high shear mixer (Fig. 2.1) was used to uniformly mix the treated glass fibers with molten virgin HDPE. For every 100 g of HDPE, 17 g of treated glass fibers were used. The high shear mixer comprises a custom made, disc-shaped, wooden head attached to the spindle of a drill press. A container holding molten HDPE and treated glass fibers is attached on top of a hot plate which is fixed to the table of the drill press. The inner diameter of the container is slightly larger than the wooden head. To increase throughput, HDPE pellets and glass fibers were placed in small batches in a vacuum oven preheated to 150 °C for melting prior to mixing. After complete melting of the HDPE, the batch was transferred to the high shear mixer. During the mixing process, the hot plate was maintained at 160 °C to prevent HDPE from solidifying. The spindle speed was kept fixed at 300 RPM. After uniform mixing of glass fibers and HDPE, the composite was pressed to a sheet of roughly 4 mm thickness and cut to chips approximately 10 mm on a side while still hot and malleable.

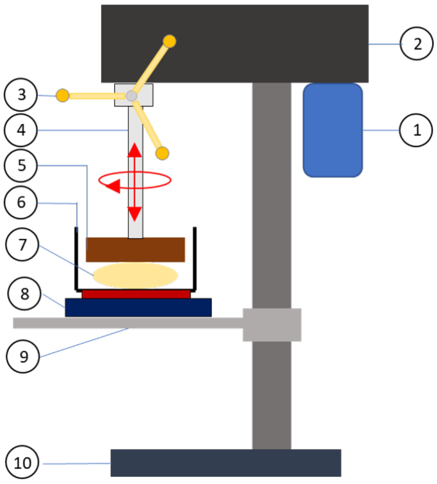

1	Motor
2	Pulley assembly
3	Feed Handle
4	Spindle
5	Custom-made wooden head for high shear mixing
6	Container for shear mixing HDPE and fillers
7	molten polymer and fillers before mixing
8	Hot plate
9	Table
10	Base

Figure 2.1: Schematic of custom-made high shear mixer designed to blend treated glass fibers with molten HDPE. The mixer features a disc-shaped wooden head attached to the spindle of a drill press. A container holding the material sits atop a hot plate, with a temperature maintained at 160 °C. The spindle speed is fixed at 300 RPM to ensure uniform mixing. Prior to mixing, materials are preheated in a vacuum oven at 150 °C.

Epoxy Coating of media: Loctite Epoxy Marine, a filled epoxy, was used for surface coating of the composite pellets. Equal volumes of epoxy and hardener were used. The coating process was done by mixing small batches of pellets in the epoxy-hardener mixture by stirring. The coated media pellets were then spread and rested on a sheet of wax paper for curing (24 hours at 32 °C). Considering an average epoxy thickness of 0.1 mm and average dimension of a composite pellet as stated earlier, approximately 0.13 grams of epoxy was applied per gram of composite. The specific gravity of epoxy hardener and resin is 1.49 and 1.56 respectively [121], giving an average density of 1.53 g/ml neglecting shrinkage on curing.

2.2.2 Differential Scanning Calorimetry

The thermodynamic performance of the media is characterized in terms of latent heat of fusion. We conducted differential scanning calorimetry (DSC) experiments using a Perkin Elmer Jade calorimeter on three sets of samples: pure HDPE media in pristine conditions, fresh fiber reinforced composite, and composite that has been aged for more than 100 thermal cycles in glycerol. The materials were sealed in an aluminum pan for testing, and experiments were conducted under nitrogen atmosphere. For all three cases, 9.7 mg of sample was used for DSC testing. The test procedure involved holding the sample for a minute at 90 °C, then heating it from 90 °C to 140 °C at 5 °C/min, followed by cooling from 140 °C to 90 °C at 5 °C/min. For latent heat calculation, we subtracted a baseline heat flow value (consistently 16.5 mW) from the actual heat flow values during the melting of the material. The area under the resulting endothermic curve was calculated. This consists primarily of the latent heat of melting of the material.

2.2.3 Experimental Setup

Figure 2.2a gives a schematic of the thermal loop and controls for the energy storage system used for experiments. The system was located outside of climate control in a 6 ft. x 8 ft. metallic shed (Fig. 2.2b) to simulate actual operating conditions. The flow loop consists of a unidirectional gear pump supplying two alternating flow paths actuated by four solenoid valves controlling the flow direction at the bed.

An aluminum containment vessel with a volume of approximately 11.4 L and internal diameter of 20 cm holds 3.6 kg of the stabilized PCM. The PCM is held in place in the containment vessel between two perforated aluminum plates separated 20 cm apart and completely submerged in glycerol (Fig. 2.3). Glycerol is used as a heat transfer fluid due to its low vapor pressure to minimize the influence of evaporation. Table 2.1 gives relevant thermophysical properties for the

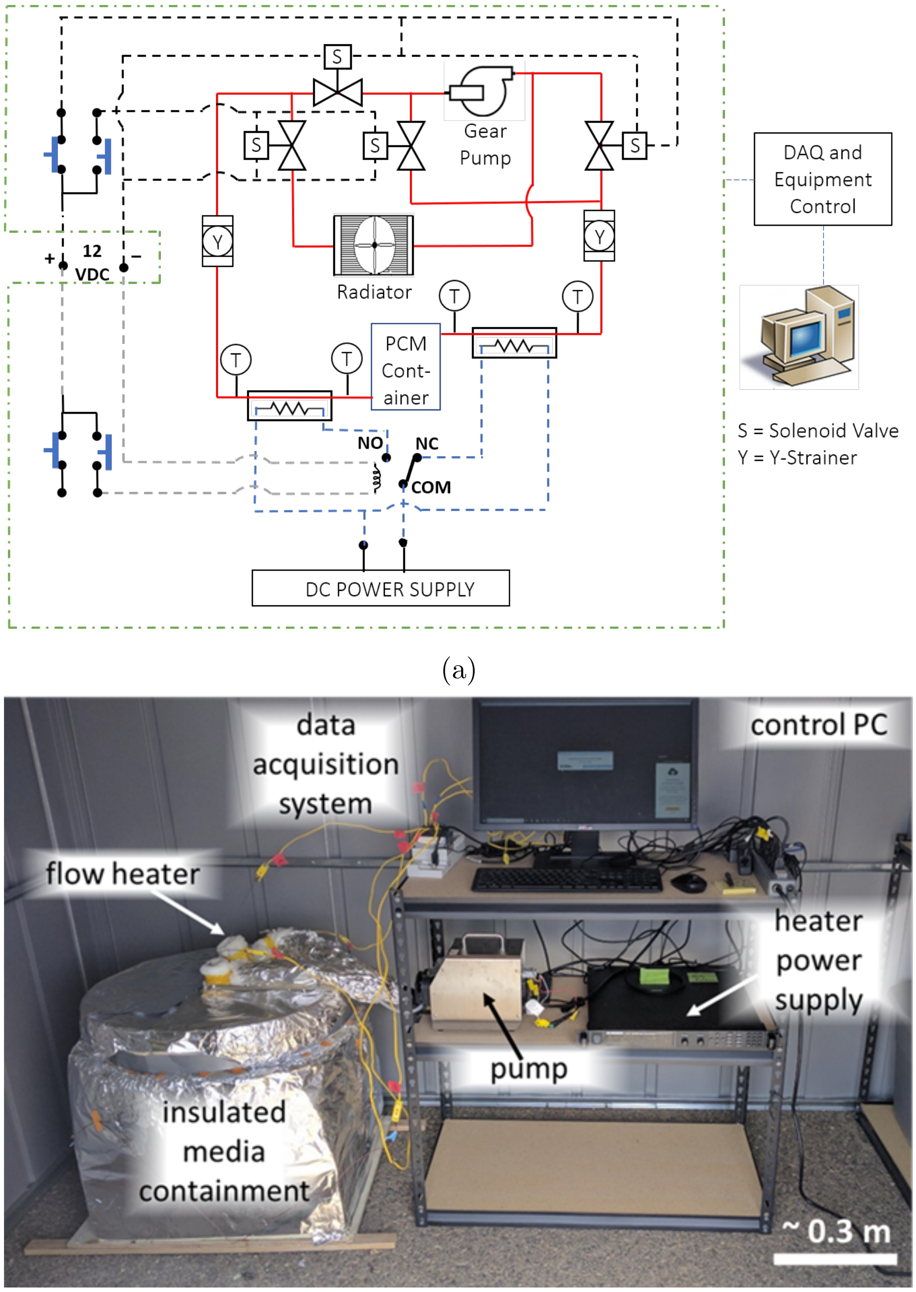

(a)

(b)

Figure 2.2: Setup for bulk experiments. (a) Flow loop and control schematic. (b) System in operational condition. (The photograph here shows a previous flow loop with flexible tubing, reversible pump, and single flow heater.)

experiments. Heat transfer fluid is delivered into and out of the bed is done using stainless steel tubes with external diameter of 0.25 in. As shown in Fig. 2.3, the shorter tube reaches near the top perforated platform such that the opening is below liquid level an no air is entrained while discharging. The longer tube extends approximately 1 cm below the bottom platform. Two thermocouples are placed inside these tubes to directly measure the temperature of the fluid inlet and exit from the bed. Both thermocouples are placed just at the entry of the containment vessel, above the heat transfer liquid pool. The containment vessel is insulated with polyisocyanurate foam, glass wool and polyurethane foam insulation. Parasitic heat loss to the ambient is discussed below and characterized in supplementary material.

The media bed is incorporated in the loop using two inline flow heaters attached to a DC power supply to control heat transfer fluid temperature entering the storage bed during charge and discharge. To maintain hydrodynamic stability in the bed, flow reversal is necessary during charging and discharging for a fully submerged packed bed system [56]. Therefore, hot fluid must remain on the top and colder fluid on the bottom to prevent local convection in the bed. For example during charging, hot fluid is delivered on the top of the bed above the top platform while colder fluid exits from the space below the bottom platform (Fig. 2.3). A liquid-air heat exchanger serves as a thermal load that is operational only during discharge.

CONTROL

During experiments, the charge/discharge rate of the packed bed configuration was controlled by flow rate and fluid temperature. A desired mass flux of the heat transfer fluid was achieved by controlling the RPM of the gear pump, while fluid temperature was adjusted via power delivered to the heaters. Although two heaters were included in the thermal loop, only one heater was active at any time, depending on flow direction. Flow direction during charging and discharging was controlled through the solenoid valves. K-type thermocouples were used to measure temperature (Evolution Sensors and Controls, LLC). They were connected to a temperature input module (National Instruments, NI-9211) of a compact data acquisition chassis (National Instruments, NI cDAQ-9172) controlled via a personal computer.

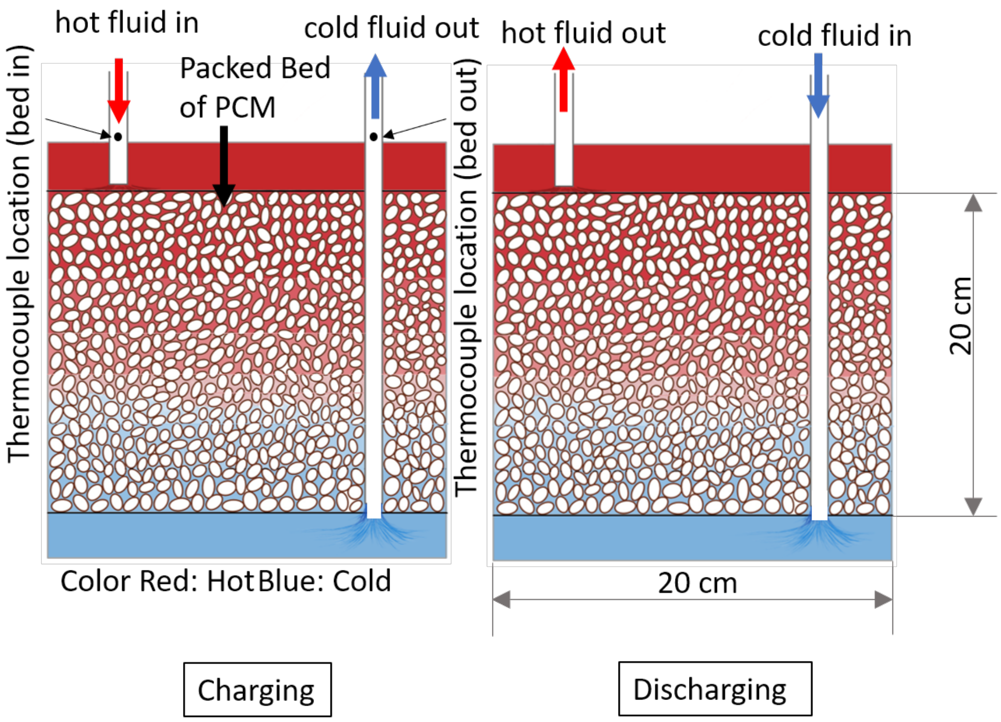

Figure 2.3: Schematic of filled media containment vessel and fluid flow direction during charging and discharging.

THERMOCOUPLE CALIBRATION

All thermocouples were calibrated while attached to the data acquisition system. An aluminum block with dimensions 150 mm x 150 mm x 25 mm was used to create a uniform temperature environment. Holes of approximately 50 mm length and diameter marginally greater than the thermocouple probe diameter were drilled close to each other perpendicular to the narrow axis of the block. A small amount of thermal interface compound (Arctic MX-4) was used to minimize contact resistance with thermocouple probes inserted into the block (following cleaning with isopropyl alcohol). The block was placed on top of a hot plate and insulated with glass wool insulation. The block was heated and held steady at a temperature of 190 °C. Temperatures were recorded for the thermocouples while the block was at steady state and as it was allowed to cool slowly. For calorimetry purposes, two thermocouples were selected to measure the fluid inlet and the fluid exit temperatures that had the closest readings overall with a maximum difference of 0.15 °C.

Table 2.1: Thermo-physical properties of HDPE and glycerol.

Properties	Value	Units
HDPE Melt Flow Rate (190 °C/2.16 kg)	0.8	g/10 min
HDPE Density (23 °C)	≥ 0.96	g/cm^3
Glycerine (pure) specific heat (127 °C)	3.09	kJ/kg/K
Glycerine (pure) viscosity (127 °C)	0.00686	Pa.s
Glycerine (pure) density (127 °C)	1195.3	kg/m^3

EXPERIMENTAL PROCEDURE

Before the charging process, glycerol was gradually heated from room temperature to a steady bed temperature below the melting point of HDPE. Power was then directed to one of the flow heaters to obtain a constant charging temperature higher than the PCM melting point throughout the charging process. The charging process continued until a steady bed outlet temperature was obtained. After charging, the fluid flow direction was reversed. The heating power was stopped for a couple of minutes before directing power to the second heater controlling fluid inlet temperature during discharging. Fluid with a constant temperature lower than the re-crystallization temperature of the media was introduced at the bottom of the packed bed. The discharging process again continued until a steady outlet temperature was reached.

2.2.4 Bulk Calorimetry Characterization

The TES system has been characterized for thermal capacity and charge/discharge temperature (heat transfer) performance. The rate of heat transfer to the system is calculated based on calorimetry of the flow and is given by the product of the mass flow rate, $\dot{m}$, the specific heat of the fluid, c, and the temperature difference between the fluid inlet, T_{in} and outlet, T_{out} to the bed as shown in equation 2.1.

$$q_{\text{flow}} = \dot{m}c(T_{\text{out}} - T_{\text{in}}) \tag{2.1}$$

The total heat capacity of the system is calculated as the time integral of the rate of heat extracted during solidification and the rate of parasitic heat loss from the system to the ambient as given by equation 2.2.

$$Q_{\text{latent}} = \int_{\text{solidification}} (q_{\text{flow}} + q_{\text{loss}})dt \tag{2.2}$$

The heat loss rate is calculated by a steady state energy balance of the bed after complete charging. At steady state conditions, this could be measured instantaneously based on the inlet and exit temperatures and heat capacity flow, but a time integral provides better accuracy. The total energy loss over a chosen time period of steady state operation (say, between t_a and t_b) is thus calculated as the time integral of the product of the temperature difference between the inlet and exit of the fluid, the mass flow rate, and the specific heat of glycerol over that time. The average heat loss rate, q_{loss} is then equal to the energy loss divided by the time chosen (t_b - t_a) as shown in Eq. 2.3 below:

$$q_{\text{loss}} = \frac{\int_{t_a}^{t_b} \dot{m}c(T_{\text{in}|_{\text{steady}}} - T_{\text{out}|_{\text{steady}}})dt}{t_b - t_a}. \tag{2.3}$$

The average power loss measured ranged from 2.8 - 26.8 W for this experimental setup, which is not in a climate controlled enclosure. We have used the minimum value of 2.8 W for following calculations to provide a conservative estimate of the stored energy (see eq. 2.2). Heat dissipation rate measured throughout multiple charging/discharging processes is given in supplementary material.

Due to the non-isothermal exotherm during discharging, a 'nominal latent heat' term is defined for heat energy extracted between 130 °C and 125 °C. 'Total heat' is then defined here as the heat energy extracted during discharging between initial bed temperature to the minimum operating/discharging temperature. In section 2.3.3 we discuss the effect of varying this minimum discharging temperature, but throughout the rest of the chapter, we consider it fixed at 125 °C.

The extracted energy, Q_{ex} is calculated as follows:

$$\begin{gathered} Q_{ex} = \int_{t_1}^{t_2} (\dot{m}c(T_{\text{out}} - T_{\text{in}}) + q_{\text{loss}})dt = \\ \sum_{i=1}^{N-1} (\dot{m}c(T_{\text{out}_i} - T_{\text{in}_i}) + q_{\text{loss}})(t_{i+1} - t_i) \end{gathered} \tag{2.4}$$

Where, N is the total number of experimental data points recorded between times t_1 to t_2, which correspond to the starting and ending temperatures, respectively. The corresponding discharging time is the difference between t_2 and t_1. To calculate the nominal latent heat extracted, t_1 and t_2 correspond to the time at which the bed outlet temperature is 130 °C and 125 °C, respectively. Whereas, the total energy retrieved during discharging is calculated based on $t_1 = 0$ and t_2 corresponding to the minimum operating temperature. The corresponding average power extracted, P_{ex} is calculated as follows:

$$P_{ex} = \frac{Q_{ex}}{t_2 - t_1} \tag{2.5}$$

2.2.5 Exergetic Efficiency

Exergetic performance for the system is calculated as follows. T_0 is the dead state temperature (25 °C here). T_c and T_d are the temperatures of the inlet fluid during charging and discharging of the bed, respectively. The exergy input to the system during charging can be calculated as

$$x_{ch} = Q_{ch}\left(1 - \frac{T_0}{T_c}\right). \tag{2.6}$$

The exergy output from the system after discharging can be calculated as

$$x_{dis} = Q_{dis}\left(1 - \frac{T_0}{T_d}\right). \tag{2.7}$$

where Q_{ch} and Q_{dis} are the energy required to charge the system from T_d to T_c and discharge the system from T_c to T_d respectively.

$$Q_{ch} = \int\limits_{t_1 @ T_{out}=T_d}^{t_2 @ T_{out}=T_c} (\dot{m}c(T_{\text{in}} - T_{\text{out}}))dt \tag{2.8}$$

$$Q_{dis} = \int\limits_{t_1 @ T_{out}=T_c}^{t_2 @ T_{out}=T_d} (\dot{m}c(T_{\text{out}} - T_{\text{in}}))dt \tag{2.9}$$

It needs to be noted that the parasitic loss is already included in Eq. 2.8 and 2.9 since T_{in} and T_{out} are actual experimental data. The exergetic efficiency of the TES system is

$$\eta_x = \frac{x_{dis}}{x_{ch}}, \tag{2.10}$$

and the energetic efficiency of the TES system is

$$\eta_e = \frac{Q_{dis}}{Q_{ch}}. \tag{2.11}$$

2.2.6 Error Analysis

Several sources contribute to the uncertainty of determining heat flow and capacity in the system. Based on the calibration discussed above, the calorimetric temperature probes have an estimated error of ±0.15 °C between each other. This uncertainty is negligible compared to other sources contributing to uncertainty in energy. Likewise, error bars are not shown for temperature, as they are generally not visible. Uncertainty in measurement of time is also negligible.

There is a ±2% error in volume flow determination of the heat transfer fluid based on calibration of the gear pump via measurements of total flow volume and time at relevant viscosity. The value of specific heat of glycerol varies about ±1% over the temperature range for this study. We use an average value of 3.09 kJ/kg/K for all calculations. Thus errors in flow measurement and thermophysical properties of the heat transfer fluid contribute ±3% to the uncertainty of energy and power values.

The largest contribution to uncertainty in energy and power is heat loss to ambient (e.g. Eq. 2.4). We measured this loss for the system at steady state at various temperatures during multiple experiments over several days. (See supplementary material and section 2.2.4 for more detail.) The instantaneous value of parasitic heat loss ranges from 2.8 - 26.8 W (0.778 - 7.44 W/kg media) depending on the environment in the enclosure containing the system. We use the minimum heat loss rate (2.8 W, 0.778 W/kg) in the calculation of our declared values for energy and power as this is the most conservative choice. A larger choice of parasitic loss results in a higher calculated value of stored energy.

The reported error bars for energy and power result from the combination of uncertainty in parasitic heat loss, flow, and thermophysical properties. The lower bound of uncertainty is simply 3% lower than the declared value, which is calculated using the minimum heat loss rate to ambient. The upper bound of uncertainty is 3% higher than the energy/power value calculated with the maximum ambient loss rate (26.8 W, 7.44 W/kg).

2.3 Results and Discussion

In this section we will discuss the performance of the media as an individual component and as part of a fully immersed packed bed TES system.

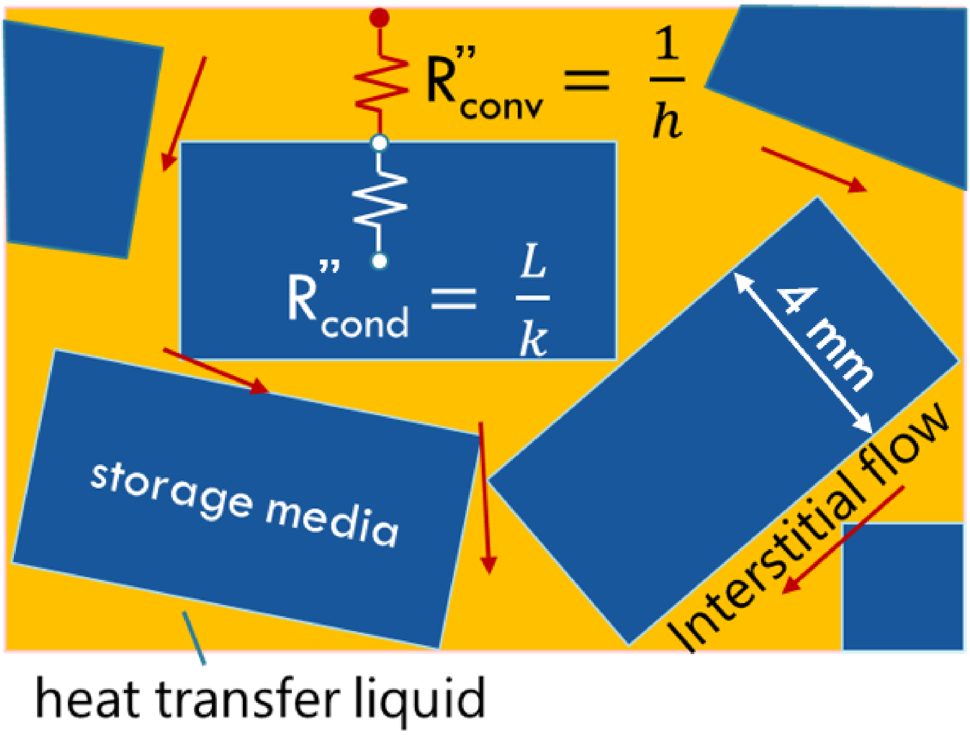

Figure 2.4: Schematic of phase change media composite pellets in a heat transfer fluid (yellow). The red arrows represent interstitial flow of the heat transfer fluid between the media pellets. The blue rectangles here represent the media pellets, which in reality, are of irregular shape and size with an average thickness of 4 mm.

2.3.1 Local Scale Heat Transfer Modelling of the Media

One of the primary advantages for the packed bed approach is in its direct contact heat exchange. This results in good heat transfer performance. The elements important in this performance are the convective resistance and the conductive resistance within the solid. Various models exist to describe the local convective heat transfer at the media level for a packed bed system. A commonly used correlation between the local Nusselt number, Reynolds number and Prandtl number, valid for low Reynolds number, is given in Equation 2.12 [122].

$$Nu_{loc} = 2.19(RePr)^{1/3} \tag{2.12}$$

For representative flow rates for this system, e.g. 1.2 g/s of heat transfer fluid per kg of phase change media, we obtain a local heat transfer coefficient of 75 W/m^2/K. For comparison, for an approximately 4 mm thick media, as illustrated in Fig. 2.4, the worst case equivalent heat transfer coefficient, or inverse area specific thermal resistance, is calculated to be 500 W/m^2/K based on HDPE thermal conductivity of 0.5 W/m/K. Given the small size of the media pellets, clearly convective heat transfer dominates performance. However, both HDPE and the treated glass fibers have poor thermal conductivity, so conductive resistance can become important for thicker media. Therefore, large surface areas and small elements are important for an effective direct contact heat transfer process.

2.3.2 Media Performance

Figure 2.5: Phase change media for the TES system using form stable, epoxy coated, glass fiber reinforced, high-density polyethylene composite pellets (as synthesized). The pellets are roughly 4 mm thick and approximately 1 cm on a side.

Figure 2.5 shows the phase change media as synthesized. We have characterized media performance quantitatively in terms of thermal capacity and qualitatively in terms of stability.

DIFFERENTIAL SCANNING CALORIMETRY

The DSC thermograms in Fig. 2.6 show that the latent heat of fusion for the fresh composite (181 J/g) is less than the pristine material (192 J/g)

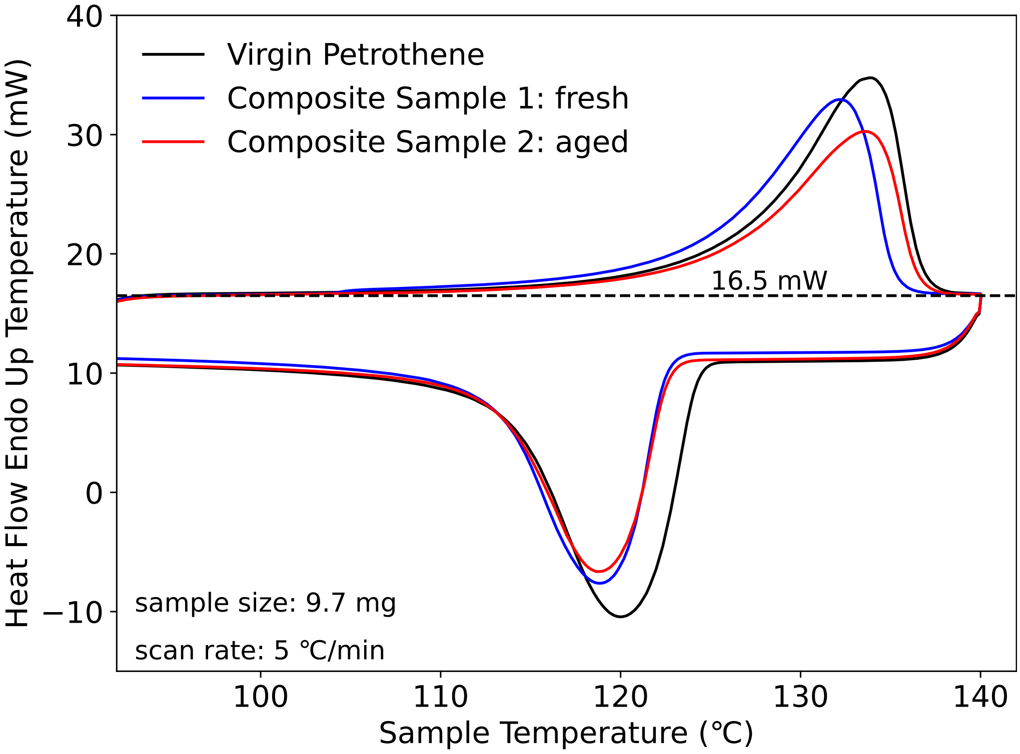

Figure 2.6: DSC traces for pristine HDPE (black curve), a sample of the fresh composite (blue curve) and another sample of the composite aged in glycerol after 100 complete melt/freeze cycles (red curve). The thermal scan rate is 5 °C/min. The latent heat of melting (calculated) for the virgin HDPE, fresh composite (sample 1) and the aged one (sample 2) are 192 J/g, 181 J/g and 149 J/g respectively. The peak melting temperatures are 133.9 °C, 132.2 °C and 133.6 °C, respectively. The peak crystallization temperatures are 120 °C, 118.8 °C and 118.8 °C, respectively.

due to addition of fillers. A melting/solidification cycle for another sample of the composite following 100 melt/freeze cycles in glycerol is also shown. Latent heat for this sample is 149 J/g. The difference in heat capacity between the two composite samples likely reflects the compositional variability (percentage of glass fiber filler) in the extremely small DSC samples rather than a change in chemistry of the composite. Bulk calorimetry (as discussed later) does not show significant change in heat capacity for aged media. For example, the bulk latent heat after 100 thermal melt/freeze cycles ranges from 162 kJ/kg - 172 kJ/kg. Significant hysteresis in melting and solidification temperature is noted in all samples, but this is likely due in part to the rapid rate of temperature change. For the DSC traces, the scanning rate was 5 °C/min which is significantly faster than the actual operational case. Therefore, local hysteresis at operational heating and cooling rates is expected to be lower.

STABILITY

While molten, it is necessary to preserve the shape of the PCM pellets and avoid consolidation in the packed bed TES system. Additionally, migration of molten HDPE in the media must be inhibited. Either of these mechanisms will restrict the flow of heat transfer fluid through the packed bed resulting in poor local heat transfer performance. The media (Fig. 2.7) described here is stabilized to prevent deformation or melt migration by two mechanisms: fiber reinforcement and encapsulation. The relatively long fibers ($>$ 6 mm) used for reinforcement are interlocked during the shear mixing process to enhance the mechanical integrity of the composite when molten. Furthermore, the octyltrichlorosilane treatment of glass fibers yields a highly non-polar surface that shows strong affinity for the HDPE, acting as a sponge to retain the melt. Encapsulation acts to further retain melt within the media and provide a rigid skeleton for the media bed. Encapsulation here is not expected to be defect free. Furthermore, cracking of the epoxy encapsulant may occur during thermal cycling. Leakage of melt is possible from gaps and fissures in the encapsulation. We synthesized the composite using HDPE with a low melt flow index of 0.8 to minimize flow of any melt not held by capillarity within the fibers or contained by the encapsulation. Finally, an important characteristic enhancing stability of the system is the small driving force for deformation or melt migration in the fully submerged system. Density of glycerin is 1.2 g/cc at 125 °C while density of molten HDPE is 0.76 g/cc and average density of the composite in its

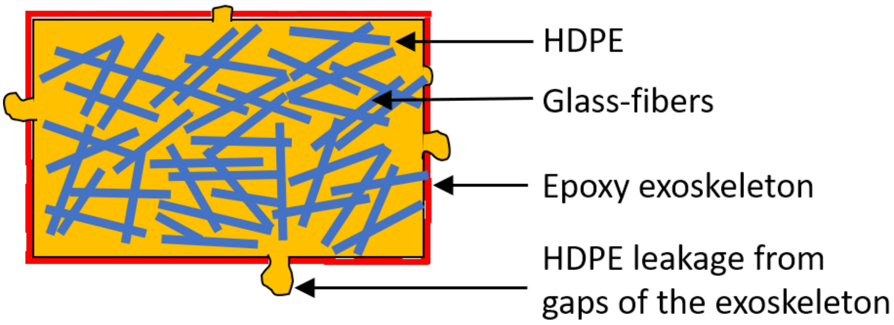

(a)

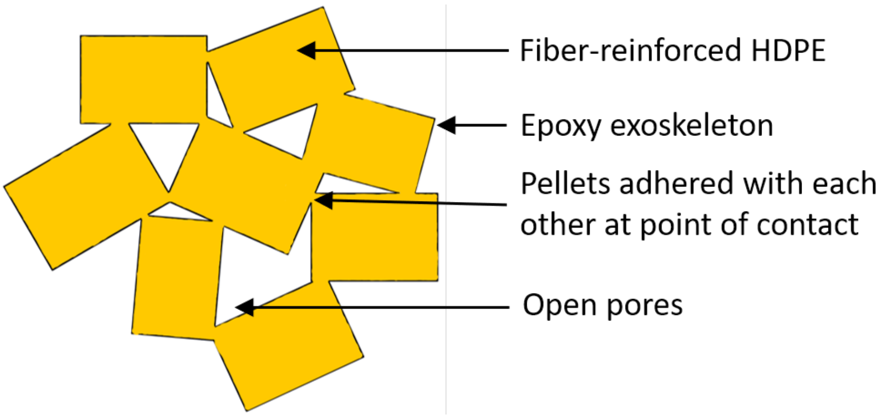

(b)

Figure 2.7: Schematic of the HDPE/glass fiber composite with epoxy exoskeleton. (a) Single pellet showing the random distribution of glass-fibers in the HDPE matrix and ossible leakage of HDPE from the gaps of the exoskeleton. (b) Pellets adhered with one another at their points of contact to form a stable open porous structure.

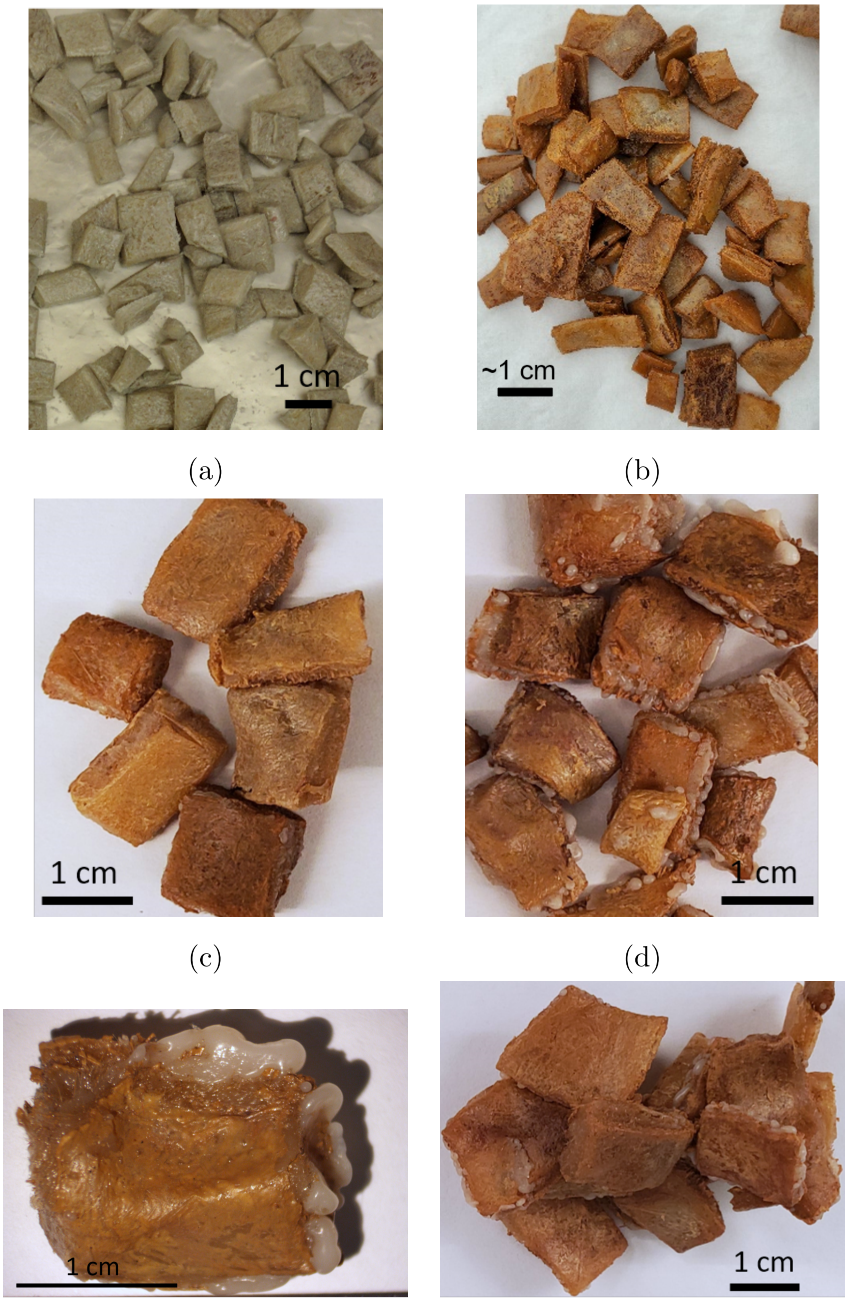

(a) (b)

(c) (d)

(e) (f)

Figure 2.8: Integrity of storage media consisting of HDPE matrix with 15% glass fiber reinforcement and epoxy coating a.) immediately after synthesis and following melting/freezing in bed for b.) 30 thermal cycles. c.) 100 thermal cycles. d.) Small subset of media showing significant HDPE leakage after 100 thermal cycle. About 8 -10% of the samples tested showed some visible leakage. e.) A sample showing worst case leakage. f.) Composite pellets stuck with each other to form a stable porous structure.

molten state is 0.85 g/cc. Therefore HDPE and composite media tend to float in glycerol at operating condition, and stress felt by the composite media at top of the bed is less than 41% of the stress experienced by the media at bottom of a similar bed free of glycerol. Moreover, due to addition of glass fiber fillers in the composite, stress experienced by the composite at the top of the bed is less than 20% of the stress experienced by a pure HDPE media deprived of any fillers due to buoyancy.

For a viable system, the storage media has to be stable over many cycles. We evaluated the stability of this media over 100 bed thermal cycles. Figure 2.8a shows the freshly coated composite and figures 2.8b and 2.8c, the composite following approximately 30 and 100 bed thermal cycles, respectively. The media showed some change in color in the epoxy coating after thermal cycling in glycerin, but the coating remained rigid. Most of the media is mechanically stable and robust with little melt migration or consolidation of pellets after 100 cycles. A sample of about 1500 pellets were collected randomly after more than 100 bed thermal cycles. Greater than 91% of the media showed no leakage, while less than 9% displayed detectable leakage of HDPE from the media. Figure 2.8d shows a few handpicked samples of media pellets with leakage. Figure 2.8e shows an example of the most severe leakage corresponding to less than 1% of the media. Probable reasons of HDPE migration from the composite are non-uniform fiberglass mixing with the HDPE matrix and improper coating of epoxy leading to holes in the encapsulation. Adhesion of composite pellets to each other was also examined and found to be minimal. Adhesion that did occur resulted in open porous structures as shown in 2.8f. These structures could easily be broken to their individual pellet form. Similar phenomena was reported by Salyer and Davison [59] for cross-linked HDPE pellets.

Thermal stability of media was measured by dry and wet thermal cycling. One sample was completely submerged in glycerol at 150 °C and another sample was placed on a hot plate maintained at 150 °C in air. Both these samples were subjected to long term (24 hours) exposure in their respective environments. After complete cooling, mass change for both these media samples were found to be less than 0.1%.

The non-polar fiber surface treatment also proved effective in preventing intrusion of the glycerol to the fiber/HDPE interface. No swelling was noted in the media following long term glycerol exposure and thermal cycling (more than 100 cycles). Media synthesized without additional fiber surface treatment shows gradual swelling of the PCM at operating conditions in glycerol.

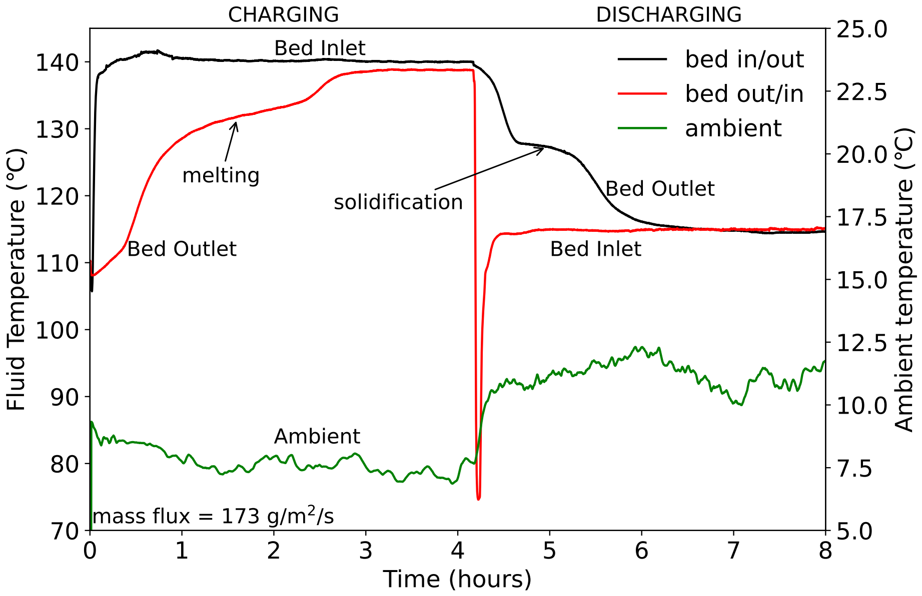

Figure 2.9: Example charge/discharge cycle for TES system. Mass flux of glycerol is 173 g/m^2/s. After complete charging of the bed, flow is reversed for discharging.

2.3.3 System Performance

In this section, we focus on the overall TES system performance in terms of system stored energy density, discharge power, and temperature difference between charge and discharge, $\Delta T_{c/dc}$. We performed bulk calorimetry characterization on packed beds consisting of 3.6 kg of stabilized media.

While the latent heat of melting and the melting and recrystallization temperatures of HDPE can be obtained from the DSC traces, bulk experiments provide three key advantages. Firstly, they are more representative of the overall media composition. A small sample of ($\approx$ 10 mg) is sensitive to compositional fluctuations in the composite. Secondly, the heating and cooling rate in DSC is significantly faster than that applied during cycling of the full system as necessitated by experimental constraints. This is likely to have a strong influence on melting/recrystallization hysteresis and possibly total heat capacity. Thirdly, bulk experiments allow characterization of the heat transfer performance of the entire system including fluid/media interactions.

Figure 2.9 illustrates a typical charge/discharge cycle of the packed bed system consisting of 3.6 kg of stabilized phase change media. The mass flux of glycerol is 173 g/m^2/s. The flow heater rapidly raises the inlet fluid temperature from 110 °C to 140 °C at the start of charging and holds it relatively steady throughout the charging process.

Consequently, the bed outlet temperature rises sharply until the onset of the melting endotherm. Gradual increase in temperature, corresponding to melting of the media, is observed until the packed bed is fully molten or charged. Completion of bed melting is detected at approximately 135 °C after which the outlet temperature rises rapidly and attains a steady state value slightly lower than the charging temperature. This steady temperature difference between the bed inlet and the outlet temperature reflects the parasitic losses from the bed to the environment. It is dependent on the bed temperature and local environment including ambient temperature and air flow in the vicinity of the system.

After the charging process, the heat transfer fluid flow direction is reversed and the discharging process commences. The heater is shut down for 4 minutes during flow reversal. Due to the introduction of cold, stagnant fluid in the loop, a dip in the bed inlet temperature is noticeable before returning to a near constant value. In this particular experiment, fluid inlet temperature during discharging is 115 °C and the corresponding initial bed temperature is 140 °C.

The bed outlet temperature decreases rapidly until the onset of the solidification exotherm. During solidification, a plateau in temperature is apparent. After complete solidification of the packed bed, the outlet temperature drops sharply before reaching a steady state close to that of the inlet.

The system shows a charge/discharge temperature difference, $\Delta T_{c/dc}$ of 12 °C for these operating conditions. Compared to sensible heat storage systems, this represents a low exergetic loss. The current $\Delta T_{c/dc}$ is also likely not a measure of the intrinsic limit but a measure of the choice of operating conditions. Lower temperature differences on charge/discharge are believed possible, ultimately limited by the melting/solidification hysteresis.

The shed containing the system is relatively small (6 ft. x 8 ft.). As a result, during discharging, the heat rejected by the system noticeably increases the air temperature of this enclosed space. The ambient temperature in the immediate vicinity of the experimental setup increases around 4 °C during discharge compared to charging.

To characterize the influence of operational conditions on system performance, the effects of fluid inlet temperature, initial bed temperature, and mass flux of the heat transfer fluid on the charging and discharging behaviour of the bed is studied. Each parameter is varied independently. Thermal capacity, charge/discharge rate, and charge/discharge temperature difference are analyzed as a function of these parameters.

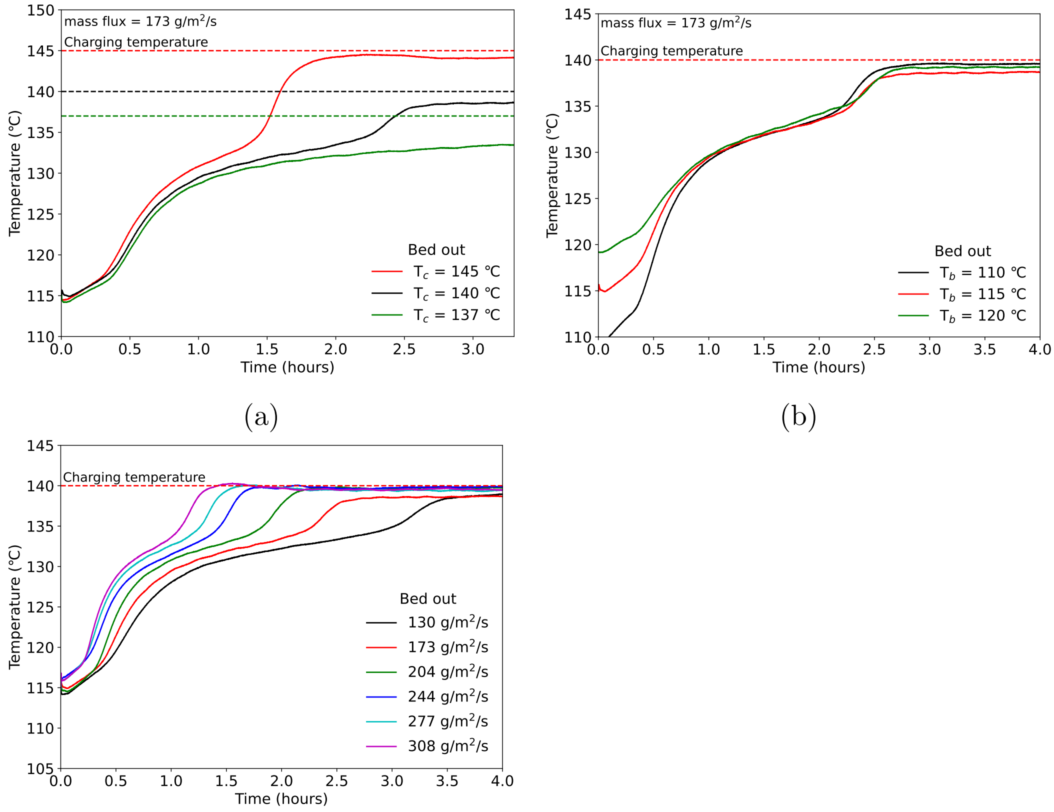

(a)

(b)

(c)

Figure 2.10: Temperature vs time traces during charging: (a) for different charging temperatures (140.0 °C, 145 °C, 137 °C). The initial effective bed temperature and the mass flux of glycerol are fixed. (b) For different initial effective bed temperatures (110 °C, 115 °C, 120 °C). The mass flux and charging temperature are kept constant. (c) For different mass fluxes of glycerol. The initial effective bed temperature and charging temperature are maintained constant.

CHARGING BEHAVIOR

Figure 2.10 shows the various charging conditions for the packed bed. The dotted lines in the figure show the nominal bed inlet or charging temperature and solid lines represent actual bed outlet temperature. (Actual inlet temperature varies somewhat with time, as seen in Fig. 2.9, but generally stays within ± 0.5 °C of the nominal value.) Each subplot considers variation in a different operational parameter. Figure (a) shows the effect of varying charging temperature for the packed bed at an initial bed temperature of 115 °C at the beginning of the cycle and heat transfer fluid flow rate of 173 g/m^2/s. Three different charging temperatures with nominal values 145 °C, 140 °C and 137 °C are studied. Figure (b) shows three cases of media charging with different initial bed temperatures 110 °C, 115 °C and 120 °C. A constant mass flux of glycerol at 173 g/m^2/s and a constant charging temperature of 140 °C is used. Figure (c) shows the influence of varying fluid flow rates (from 130 g/m^2/s to 308 g/m^2/s) on charging for an initial bed temperature of 115 °C and constant charging temperature of 140 °C. We observe that the duration of charging depends strongly on the charging temperature and mass flux of the heat transfer fluid. Whereas, the initial bed temperature has no significant effect on the duration of charging. Figure 2.10a shows a case (137 °C inlet temperature) of incomplete charging of the bed in the experimental time (3.5 hours).

DISCHARGING BEHAVIOR

Figure 2.11 shows bed outlet temperature vs time during discharging. Solid lines indicate the actual bed outlet temperatures during discharging, whereas the broken lines indicate nominal bed inlet temperatures. (As discussed above, bed inlet temperatures vary slightly during discharge but are maintained close to the nominal target value.) Figure 2.11a shows the effect of changing fluid inlet temperature from 110 °C to 115 °C while keeping the initial bed temperature and mass flux fixed at 140 °C and 173 g/m^2/s, respectively. For both these cases the bed cools at the same rate until the initiation of the crystallization process. Afterward, the lower inlet temperature results in more rapid discharge as expected. Figure 2.11b displays the influence of the initial bed temperature (after charging), 145 °C, 140 °C, or 133 °C. The mass flux of the heat transfer fluid is held constant at 173 g/m^2/s, and the fluid inlet temperature for all three cases is held fixed at 110 °C throughout the discharging process.

Figure 2.11c shows the temperature trace for discharging from an initial bed temperature of 140 °C. The bed is subjected to a discharge temperature of 115 °C for different mass fluxes ranging from 101 g/m^2/s to 308 g/m^2/s. Figure 2.11c shows some odd behavior after solidification for some experiments. About half of the traces show final bed outlet temperatures approximately 2 °C higher than the inlet temperature. As there is no heat source available between the inlet and outlet after complete discharging, this is unexpected. We believe the effect may be due to a parasitic conduction path from a heater or possibly a measurement error for the outlet thermocouple (which is well beyond that observed during calibration). However, the inflection corresponding to the onset of solidification occurs at a relatively consistent temperature for all flow rates with

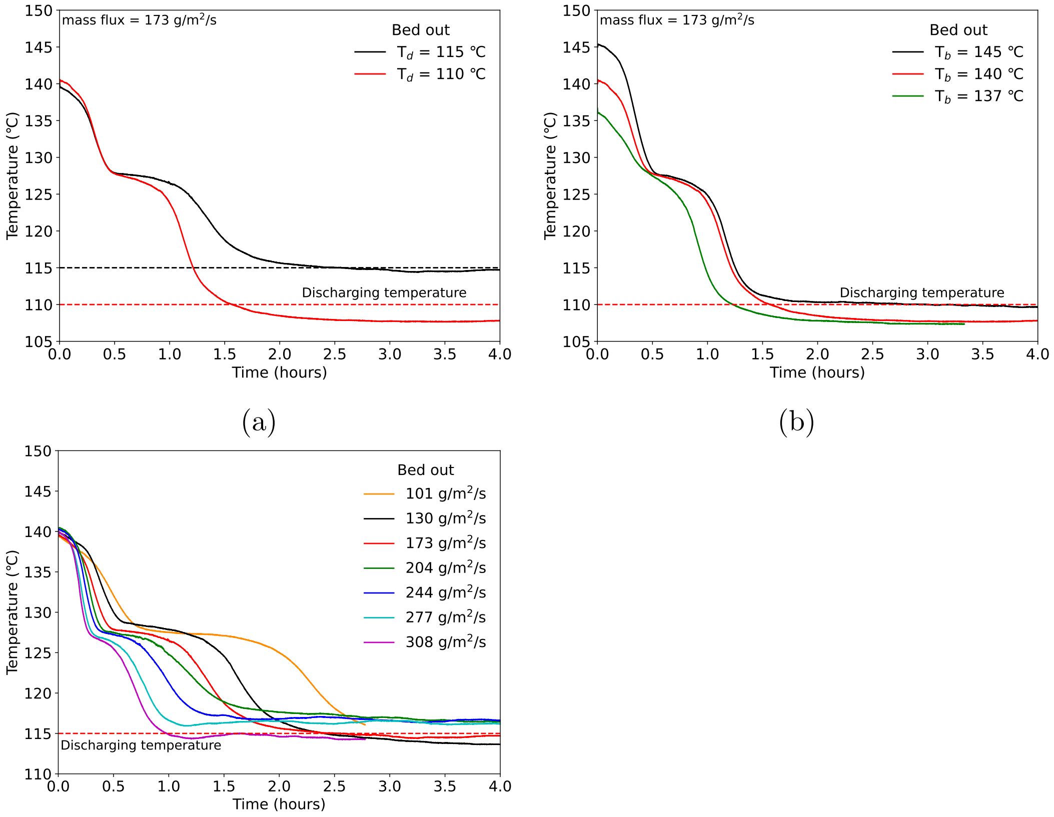

(a)

(b)

(c)

Figure 2.11: Temperature vs time traces for different discharging conditions. (a) Temperature profile during discharging from an initial bed temperature at 140 °C. The mass flux of glycerol is held constant at 173 g/m^2/s. The bed inlet temperature during the discharging process is studied for two different cases: 110 °C and 115 °C. (b) Temperature profile during discharging from steady bed outlet temperature of 145 °C, 140 °C and 133.5 °C at 173 g/m^2/s of glycerol mass flux to 110 °C final bed temperature. (c) Temperature profile during discharging from a steady bed temperature of 140 °C to 115 °C for different mass fluxes of glycerol.

no apparent correlation to the discrepancy in final temperature. Therefore, we believe influence on calorimetric characterization at the temperatures of interest are minimal. We note that for the mass flux of 101 g/m^2/s, the bed does not reach steady state condition. However, this does not influence any analyses as we only consider heat available at temperatures above 125 °C for this case (see section 2.2.4).

EFFECT OF MINIMUM DISCHARGE TEMPERATURE

Latent heat is the primary energy storage mechanism targeted with this system. The latent heat is released over a narrow temperature range associated with solidification. However, there is also significant energy stored as sensible heat in the system which is available over a larger range of temperature. Here we consider the effect of temperature at discharge (i.e. minimum allowable temperature of heat delivered by the system) on system energy capacity and the corresponding rate of energy delivery. (In following sections, we fix the minimum discharge temperature at 125 °C.)

Figure 2.12a shows another example of a complete charge/discharge cycle for the packed bed system. For this case, the mass flux of glycerol was 173 g/m^2/s, with initial bed temperature at 110 °C and charging at 140 °C for approximately 4 hours. After complete charging of the bed, the system was discharged with a nominal fluid inlet temperature of 110 °C for the next 2.5 hours. Figure (b) shows the cumulative energy retrieved from the media during discharge as a function of the time of retrieval (as calculated from eq. 2.4 with t_1 corresponding to the onset of discharging and time shown in the figure equal to $t_2 - t_1$). Initially, energy is delivered at a rapid rate corresponding to the emptying of hot fluid from the containment vessel along with the low temperature of the inlet fluid at the beginning of discharging. (The inlet temperature in eq. 2.4 is taken as the measured inlet temperature, not the nominal temperature, to accurately account for the energy balance of the bed.) After the initial surge, energy release slows due to the decreasing temperature difference between the inlet fluid and cooling media (and auxiliary thermal mass of the system) until a relatively steady rate is reached (from 0.39 hours - 0.94 hours since the commencement of the discharging process) corresponding mainly to release of latent heat. After 0.94 hours, the rate of energy release slows further as solidification is completed and the system cools toward equilibrium with the inlet fluid. Figure (c) shows the energy retrieved from the storage bed versus the temperature at

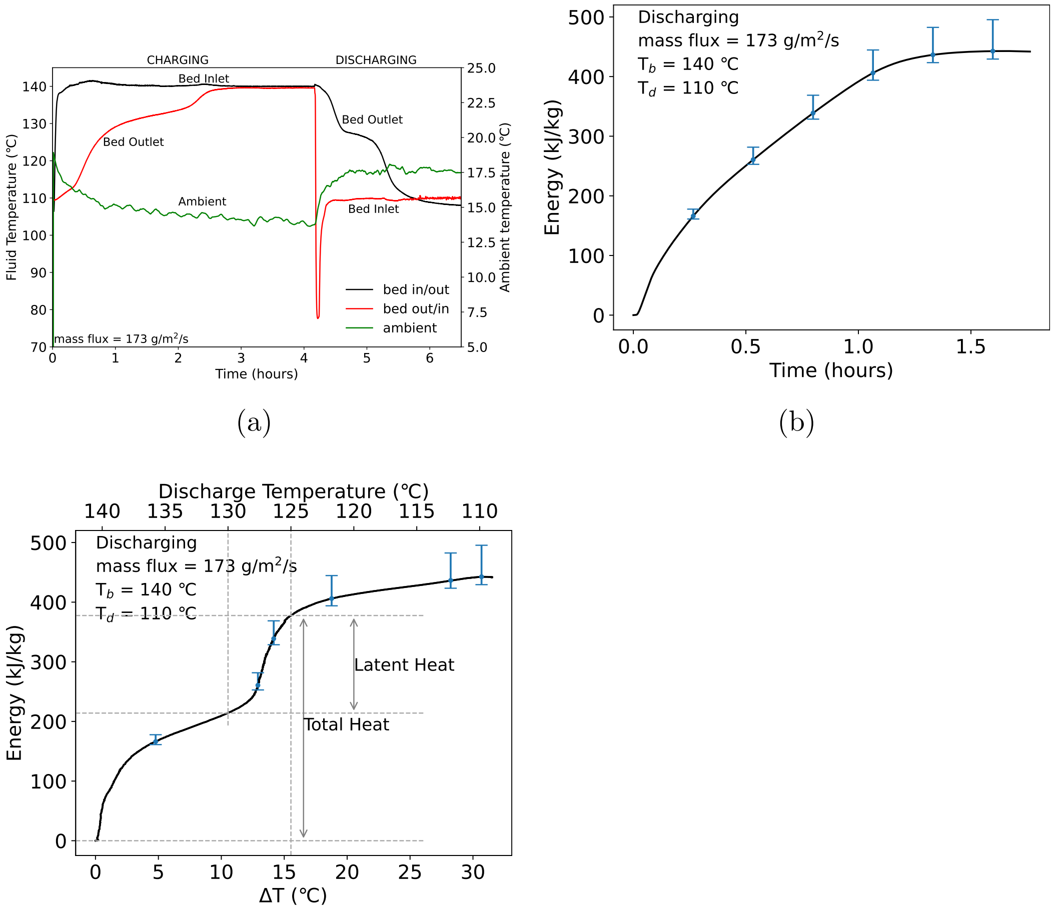

(a)

(b)

(c)

Figure 2.12: Effect of minimum discharge temperature (a) Charge/discharge cycle for TES system, with initial bed temperature of 110 °C, charging temperature of 140 °C, and inlet temperature of 110 °C on discharge at mass flux of 173 g/m^2/s glycerol. (b) Cumulative energy versus discharging time and (c) cumulative energy versus fluid inlet temperature that can be extracted during the discharging cycle shown in (a).

which the heat is retrieved. The contribution of latent heat is clearly visible based on the small temperature change during its release. Assuming the most conservative estimate of the power loss to the environment (2.8 W), the total energy retrieved between 140 °C to 125 °C is 377 kJ/kg, and the time of retrieval is 0.94 hours. The maximum energy that can be retrieved during discharging to 110 °C is 442 kJ/kg, with a discharge time of 1.58 hours. Therefore, about 85% of the maximum energy can be retrieved in approximately 59% of the maximum time for this case. By comparison, the nominal latent energy that can be retrieved during discharging from 130 °C to 125 °C is 163 kJ/kg in 0.55 hours.

EFFECT OF FLUID INLET TEMPERATURE ON DISCHARGE

As quantified above, the amount of energy available to extract from the system depends on the minimum temperature at which the heat is usable. Conversely, the fluid inlet temperature during discharge is expected to influence the rate of extraction but not strongly affect the energy available. Here (and in all following calculations) we fix the minimum discharge temperature at 125 °C. Figures 2.13a and 2.13b give a comparison of energy and power, respectively, extracted for the two discharging cases shown in Fig. 2.11a with fluid inlet temperatures of 110 °C and 115 °C. The nominal latent heat extracted (165 kJ/kg and 163 kJ/kg for 110 °C and 115 °C respectively) is almost the same. The total energy extracted since the commencement of the discharging process till the bed outlet temperature reaches 125 °C is approximately 7% higher for the lower bed inlet temperature as expected for the lower value of T_{in} in eq. 2.4 with similar final T_{out}. In contrast to stored energy, the delivered average thermal power varies significantly with inlet temperature. The average powers corresponding to nominal latent and total energy extracted for a bed inlet temperature of 115 °C are 59 W/kg and 84 W/kg respectively. Whereas, the average extracted powers are greater for the lower bed inlet temperature (110 °C) by 43% and 36% for the latent portion and total stored energy, respectively.

EFFECT OF INITIAL BED TEMPERATURE

The latent heat stored by the system depends only on the degree of melting achieved and should be independent of bed temperature above a value for complete melting. Conversely, sensible heat stored in the system will be proportional to bed temperature. Figures 2.14a and 2.14b give comparisons of energy and power, respectively, extracted for the three discharging cases shown in

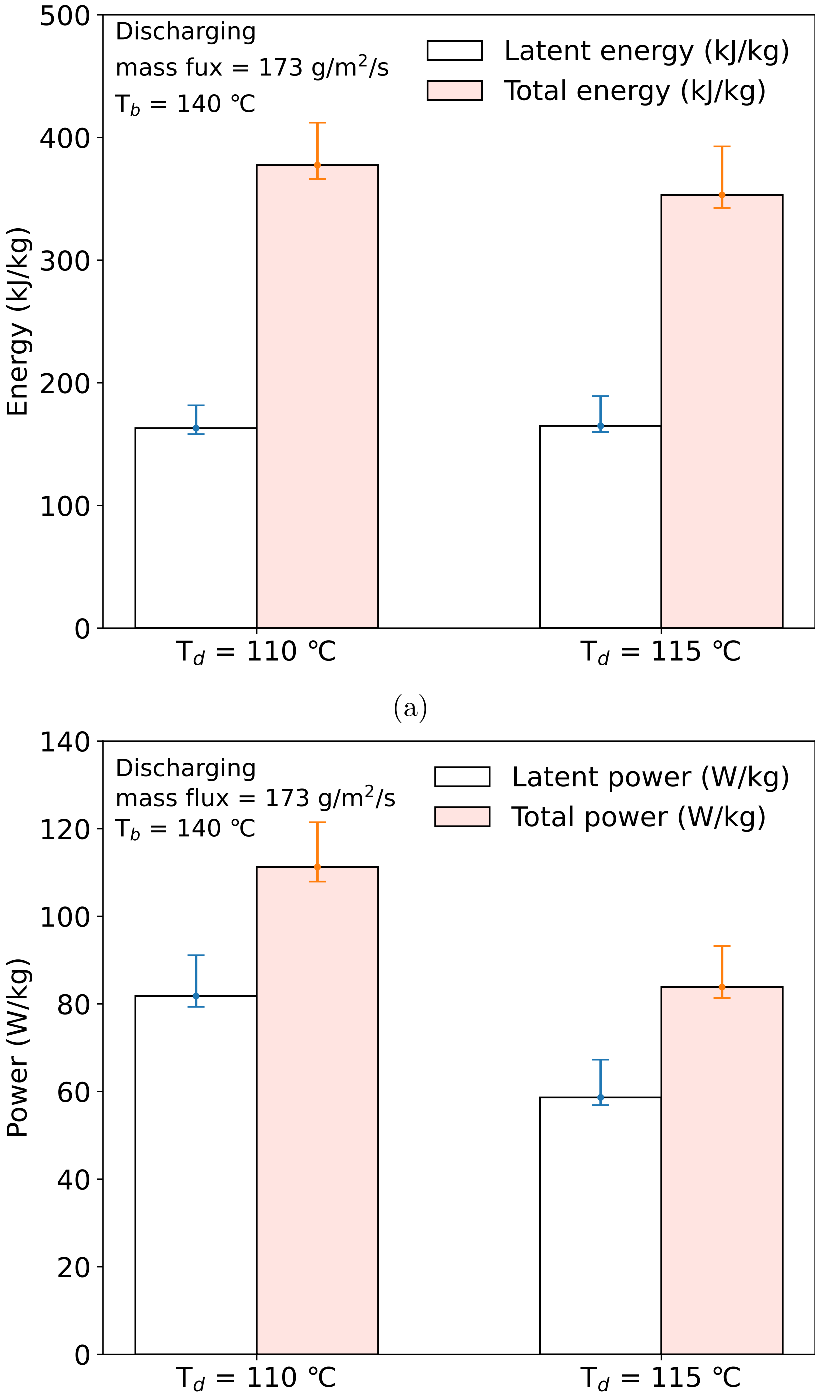

(a)

(b)

Figure 2.13: Thermal performance for differing fluid inlet temperatures on discharge (nominally 110 °C and 115 °C). The initial bed temperature at discharge is 140 °C, and mass flux of glycerol is 173 g/m^2/s for both cases. (a) latent and total energy stored (b) average thermal power delivered.

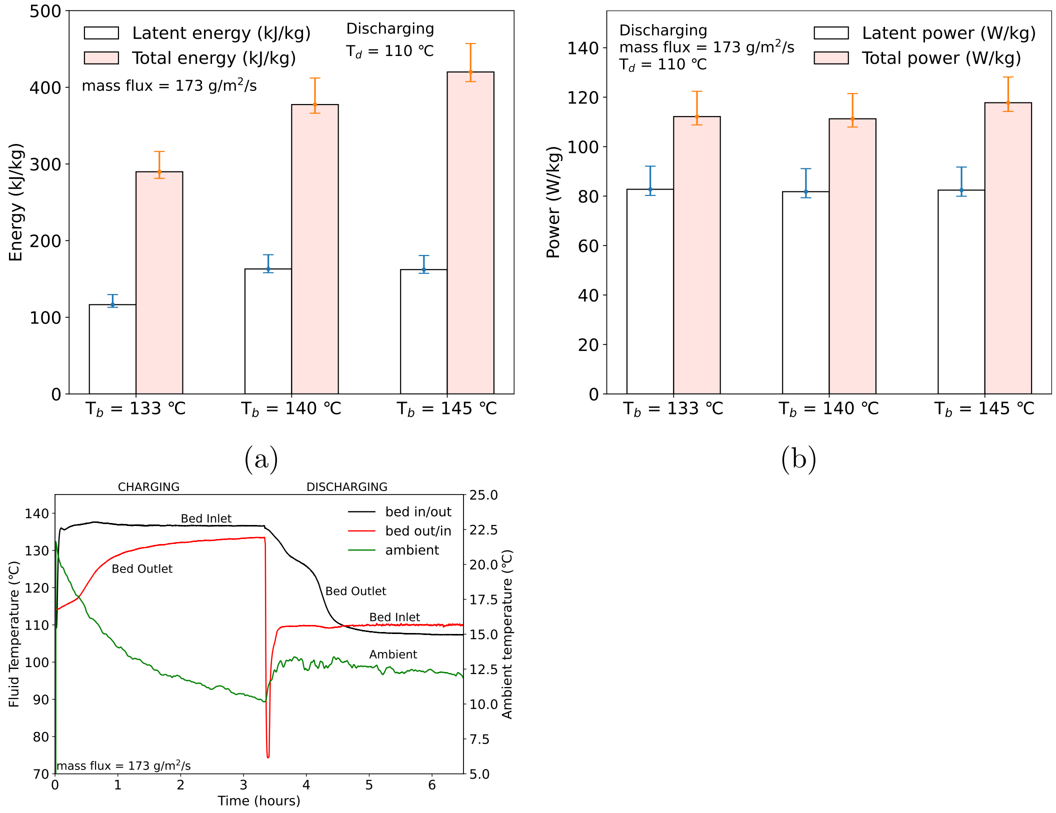

(a)

(b)

(c)

Figure 2.14: Three discharging cases were studied with different initial bed temperatures (nominal) at 145 °C, 140 °C and 133 °C and a constant fluid inlet temperature of 110 °C and mass flux of glycerol at 173 g/m^2/s. (a) & (b) represent bar charts shows the latent energy and power respectively extracted during the discharging process for these three different discharging cases. (c) An example of an incomplete charge/discharge cycle for the TES system. Charging of the packed bed started from an initial bed temperature of 115 °C for a charging temperature of 135 °C (nominal). The discharging cycle with a fluid inlet temperature of 110 °C commenced before complete charging of the packed bed. The mass flux was held constant at 173 g/m^2/s of glycerol.

Fig. 2.11b with bed temperatures 145 °C, 140 °C, and 133 °C. Figure (a) shows that the latent heat extracted is almost same for the discharging cases with initial bed temperature 140 °C and 145 °C. For the case with 133 °C initial bed temperature, the latent energy extracted is significantly less. This is apparently due to incomplete charging. Figure (c) shows the full charge and discharge cycle for this case indicating insufficient time for charging. The discharge trace still shows a clear inflection corresponding to solidification. Therefore, we expect charging at 137 °C to yield similar stored latent heat with sufficient charging time. As expected, in all cases additional sensible heat is available corresponding to higher initial bed temperature, yielding higher total retrieved thermal energy. As seen in Fig. (b), the average extracted power, both latent and total, is insensitive to initial bed temperature.

EFFECT OF MASS FLUX

Figure 2.15a shows a plot of the nominal latent heat extracted and its corresponding discharge time for different mass fluxes. We can see that as the mass flux increased, the nominal latent energy and its time of discharge increases but it appears to saturate as shown by the nonlinear curve. It should be noted that this curve fit is only for a visual aid to see the trend and not a physical model to predict the values. In this case we have used the following equation for the non-linear curve fit:

$$e_L = d + \frac{a - d}{1 + (t/c)^b} \tag{2.13}$$

where a = 100 kJ/kg, b = 4.7166, c = 0.39085 hr, and d = 167.375 kJ/kg. e_L denotes the latent energy in kJ/kg and t represents the time in hours. We used the “scipy.optimize.curve_fit” module in python3 for the non-linear curve fitting using a least squares method.

Figure 2.15b also shows a plot of the total useful heat and its corresponding total discharge time for the mass fluxes shown in Figure 12a. We used “scipy.interpolate. CubicSpline” module in Python version-3 to fit a cubic spline to the scatter plot with the second derivative at curve ends to be zero. We can see that as the mass flux decreased, the curve takes the form of a skewed bell-shaped curve. Therefore, an optimum value of the mass flux of the heat transfer fluid is obtained such that maximum amount of thermal energy can be retrieved within a reasonably short time period. It should be noted that this curve fit is

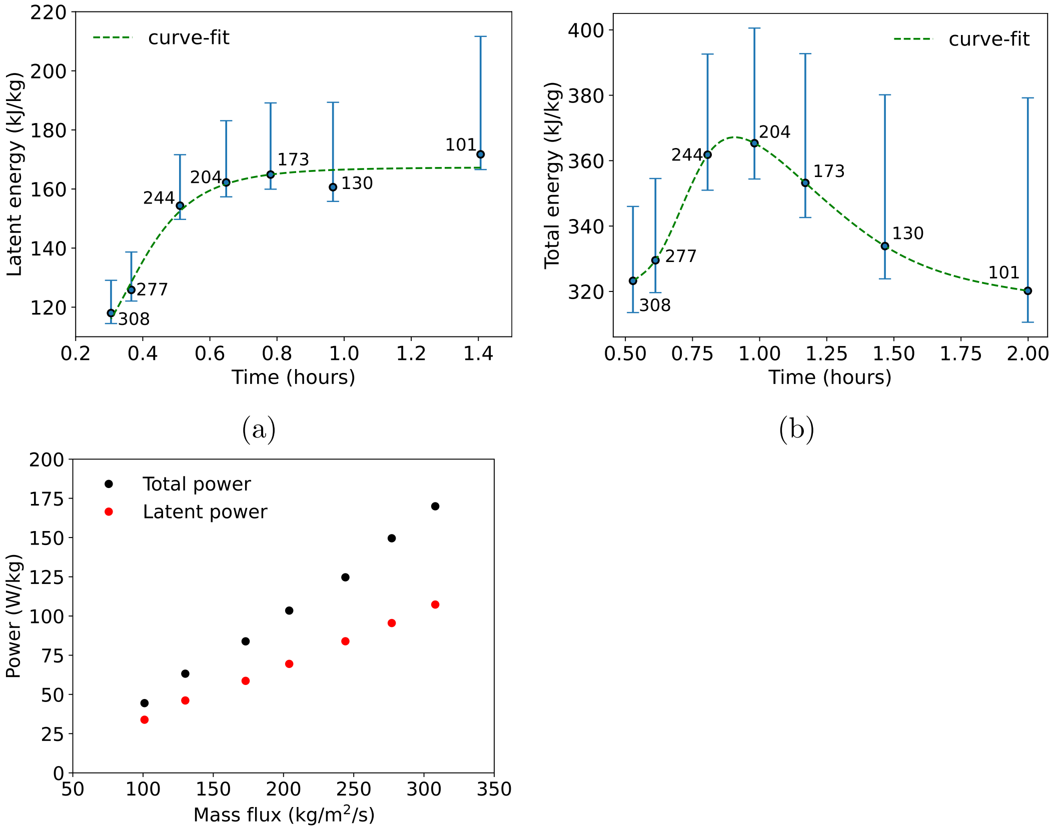

(a)

(b)

(c)

Figure 2.15: (a) Latent heat vs. discharge time and (b) total stored heat vs. discharge time during discharging from a steady bed temperature of 140 °C to 115 °C for different mass fluxes of glycerol. The numerical values corresponding to each data point represent glycerol mass fluxes in g·m^{-2}·s^{-1}. (c) Average thermal power corresponding total and latent heat vs. mass flux of glycerol.

only for a visual aid to see the trend and not a physical model to predict the values.

Higher mass fluxes allow higher thermal power at the expense of overall efficiency, (Figure 2.15c). The linear dependence of the power with mass flux indicates that the heat transfer is controlled by the rate at which thermal capacity is delivered by the heat transfer fluid. Thus the system has potential to rapidly respond to highly transient thermal loads. This performance is enabled by the form stability of the PCM composite. The robust media maintains small feature size, resulting in low conduction resistance, and large surface area with direct contact heat exchange to the transfer fluid, resulting in high rates of convective heat transfer per unit mass of media.

PRESSURE DROP IN THE BED

The power required to pump heat transfer fluid is an important characteristic of many thermal systems. The packed bed configuration offers the advantage of a large cross section for flow and correspondingly small pressure drop. The pressure drop for laminar flow through a randomly packed bed, ΔP, can be estimated using the Carman-Kozeny [123], [124] equation as follows:

$$-\frac{\Delta P}{H} = 180\frac{\mu u_b (1-\varepsilon)^2}{\Psi^2 d_p^2 \varepsilon^3}. \tag{2.14}$$

H is the height of the packed bed. u_b denotes superficial fluid velocity, and μ is the viscosity of the heat transfer fluid. ε represents the bed porosity, Ψ is the sphericity of a pellet [125], and d_p denotes the spherical equivalent particle diameter [126], which are calculated as follows:

$$d_p = \frac{3V_p}{S_p}, \tag{2.15}$$

$$\Psi = \frac{\pi^{\frac{1}{3}}\,(6V_p)^{\frac{2}{3}}}{S_p} \tag{2.16}$$

where, V_p is the volume of the pellet, and S_p is the surface area of the pellet.

The spherical equivalent diameter for a typical pellet of size 1 cm X 1 cm x 0.4 cm is 0.334 cm (Eq. 2.15) and the sphericity is 0.73 (Eq. 2.16). We measured the porosity of a randomly packed bed of PCM pellets to be 0.502. As an example of representative flows, for a moderate mass flux of 173 g/m^2/s (5.42 g/s for the current system) and fluid density of 1195.3 kg/m^3 (at 127 °C), the superficial velocity of the fluid through the packed bed is 1.45×10^{-4} m/s.

The dynamic viscosity of glycerol is 0.00686 Pa.s at 127 °C.[127]. For these conditions, the pressure drop per height of the packed bed is calculated (Eq. 2.14) to be 59.28 Pa/m, and therefore, the power required to pump the fluid through the bed is 8.60×10^{-3} W/m^3, or 5.3×10^{-5} W for the current system. In comparison, the total discharge power for the same mass flux is approximately 300 W (for initial bed temperature 140 °C and fluid inlet temperature 115 °C). The pumping power expended for pushing the liquid through the bed is negligible compared to the thermal power extracted. Further, the depth of the a storage bed with relatively equiaxed geometry will scale as the cube root of the capacity of the system, so much larger implementations would also consume negligible pumping power.

EXERGETIC EFFICIENCY AND COMPARISON TO SENSIBLE HEAT STORAGE

The exergetic efficiency of the TES system was calculated using Equations 2.6 - 2.10. Initially, we consider the charging-discharging case as shown in Figure 2.9 (mass flux of 173 g/m^2/s, initial bed temperature of 110 °C, charging liquid temperature of 140 °C, discharging liquid temperature of 115 °C). Due to parasitic losses from the bed to the environment, the final temperature of the bed never reaches the charging temperature. We define the time at which the bed outlet reaches 137 °C as the end of charging. Heat is available for the charging process at 140 °C (T_c = 413 K). We consider a process accepting heat at the minimum discharge temperature of 125 °C (T_d = 398 K). We choose the dead state temperature, T_0, to be 25 °C (298 K). The thermal energy required to charge the TES system from 125 °C to 137 °C (for these conditions) is 269 kJ/kg. Therefore the exergy input (at 140 °C) is 74.9 kJ/kg. Similarly, the heat extracted from 137 °C to 125 °C is 223 kJ/kg and the exergy available at 125 °C is 56.0 kJ/kg. We note that this is less than the 'total heat' previously given based on the starting temperature for defining discharge. By choosing 137 °C as the starting point for discharge, we do not include the initial surge in energy corresponding to the start of discharge (see Figure 2.12c, lower left corner). As discussed above, this is a result of the low inlet fluid temperature at the onset of discharge. Considering a fixed starting discharge temperature slightly below the initial bed temperature provides a better metric of the behavior of the media itself.

For these particular experimental conditions, the exergetic efficiency is calculated to be 74.8% and the energetic efficiency is 82.9%. We also calculate the exergetic efficiencies and energetic efficiencies for 4 different charge/discharge conditions with a nominal charging temperature of 140 °C and mass flux of 173 g/m^2/s. The initial and final bed temperatures vary between 110 °C and 120 °C. The resulting exergetic efficiencies range from 74.0% to 84.0%, with a mean of 79% and standard deviation of 4.8%, whereas, the energetic efficiencies ranges from 82% to 93%, with a mean of 87.6% and standard deviation of 5.3%.

Both thermal capacity and exergetic efficiency provide useful points of comparison between the current material and a sensible heat storage media, for example sand (specific heat, 0.95 kJ/kg/K [128]). A sensible heat system of similar mass would require a $\Delta T_{c/dc}$ of 235 °C for a similar storage capacity (223 kJ/kg). Conversely, over 70 kg of mineral would be required to achieve a $\Delta T_{c/dc}$ of 15 °C while storing the same energy as the current system, or more generally, the sensible heat storage will require about 20 times more mass than the latent heat system to achieve a similar exergetic efficiency. (As the heat source and sink temperatures are considered constant, exergetic efficiency can be directly related to $\Delta T_{c/dc}$.)

2.3.4 Effect of Flow-Reversal in the Bed

The packed bed configuration offers advantages in terms of heat transfer efficiency and construction simplicity, but its storage performance depends strongly on the flow patterns within the bed. It can be seen from Figure 2.17, for a fully submerged packed bed system, while charging the hot fluid enters the packed bed system from the top and colder fluid is withdrawn from the bottom. Therefore, buoyancy acts against mixing between the layers. Hence, the temperature gradient throughout the bed is stable. Similarly, while discharging, when the flow direction is reversed, cold fluid is pushed from the bottom and the hot fluid is pulled out from the top. This will again ensure that the temperature gradient throughout the bed is stable. Thus flow redirection is effective in maintaining the desired flow pattern, but leads to additional system complexity. If the flow-direction is not reversed during discharging, cold fluid will enter the top of the hot bed and will tend to fall down in a column to the bottom of the bed. This will lead to inefficient direct contact heat transfer. For a fully submerged bed, unidirectional flow is thus unfavorable. However, there is potential for unidirectional flow if a trickling flow regime in the packed bed. This will lead to a much simpler flow loop design and also lessen the weight and cost of the TES system due to reduced heat transfer liquid loading.

TEMPERATURE DISTRIBUTION IN THE BED

Experiments were performed to measure the temperature distribution in the fully submerged packed bed TES system. An example is presented in this chapter for discharging with an initial bed temperature of 140 °C and a constant bed inlet temperature of 115 °C. The mass flow rate of the heat transfer fluid was kept constant at 3.16 g/s throughout the experiment.

Figure 2.16a and b show the arrangement of thermocouples in the bed used to measure the spatial and temporal variation of temperature in the bed. Two thermocouples were placed outside the two platforms holding the bed, one above and one below. 5 more thermocouples (A - E) were placed axially in the bed between the two perforated platforms and along the center-line of the containment. 3 more thermocouples were placed horizontally in the radial direction at the midplane of the bed. Figure 2.17a and b show temperature evolution throughout the bed during discharging. Distinct temperature profiles with time are apparent at different axial positions but along the radial direction, a uniform temperature profile is measured. This indicates a solidification front that moves through the bed.

EFFECTS OF NO FLOW REVERSAL

We have also conducted tests without flow reversal, and we do not detect a solidification signature of the packed bed phase change media during discharging as shown in Figure 2.19a.

We hypothesize that the cold dense fluid when put in at top of the hot bed is unstable to natural convection. As shown in Figure 2.19b, the cold fluid will likely fall in a column to the bottom given the expected low hydrodynamic flow resistance of the bed.

Therefore, none of the bed media away from this column will participate in the direct heat transfer and the discharge rate will be slow, resulting only from conduction and convective mixing. Hence, flow reversal is essential for fully submerged storage media.

More study needs to be conducted on the effects of non-flow reversal of the heat transfer fluid between charging and discharging process.

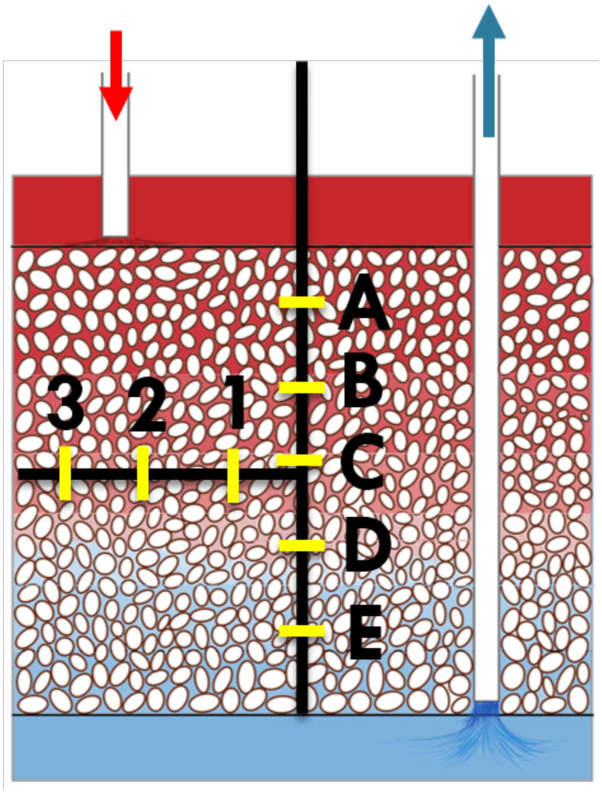

(a)

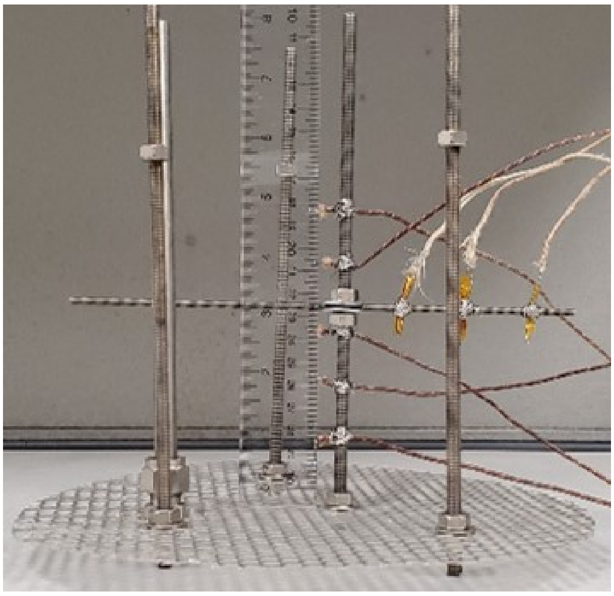

(b)

Figure 2.16: Thermocouple arrangement in the packed bed system (a) schematic (b) actual.

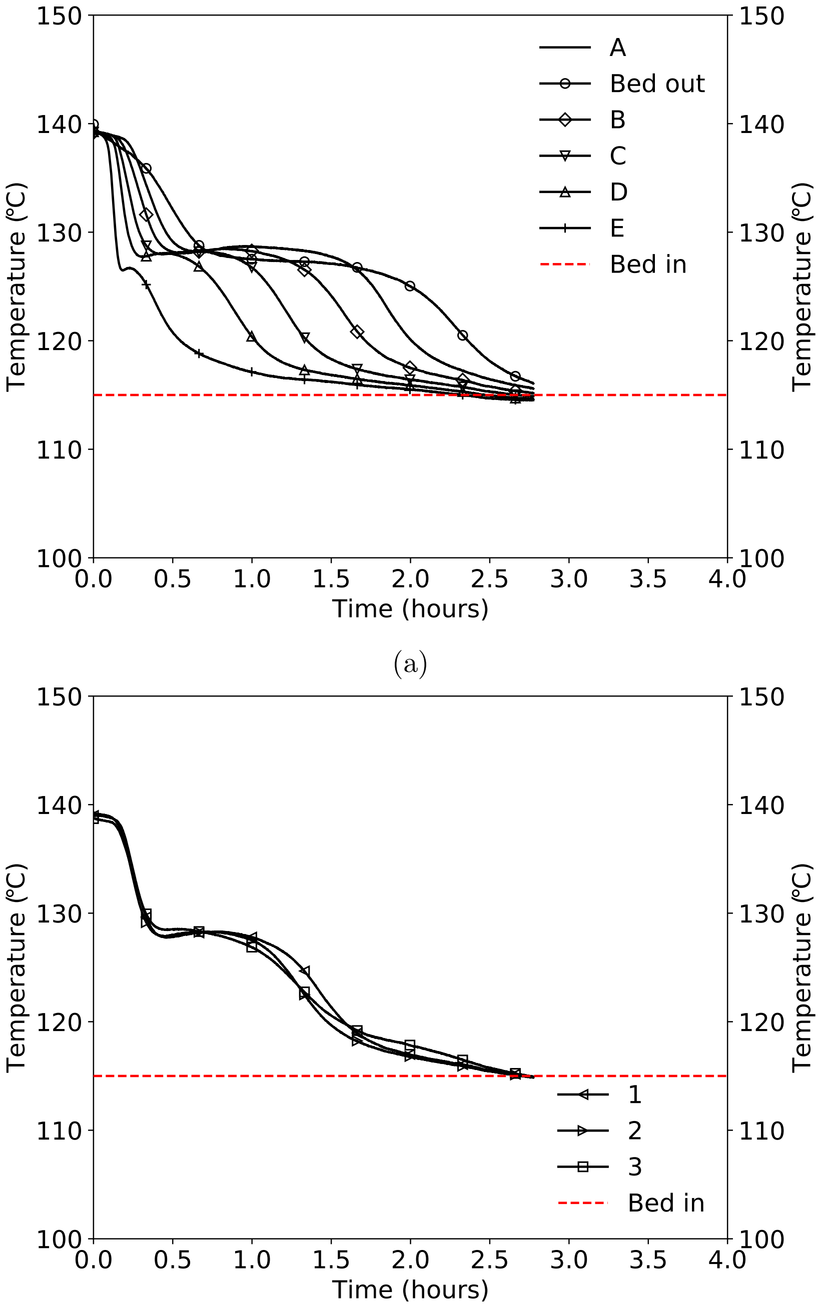

(a)

(b)

Figure 2.17: Temperature distribution during discharging cycle within the bed along with the inlet and outlet bed temperatures along the (c) axial and (d) radial direction of the media containment. The initial bed temperature is 140 °C and the discharging temperature is 115 °C. The mass flow rate of glycerol was kept constant at 3.16 g/s.

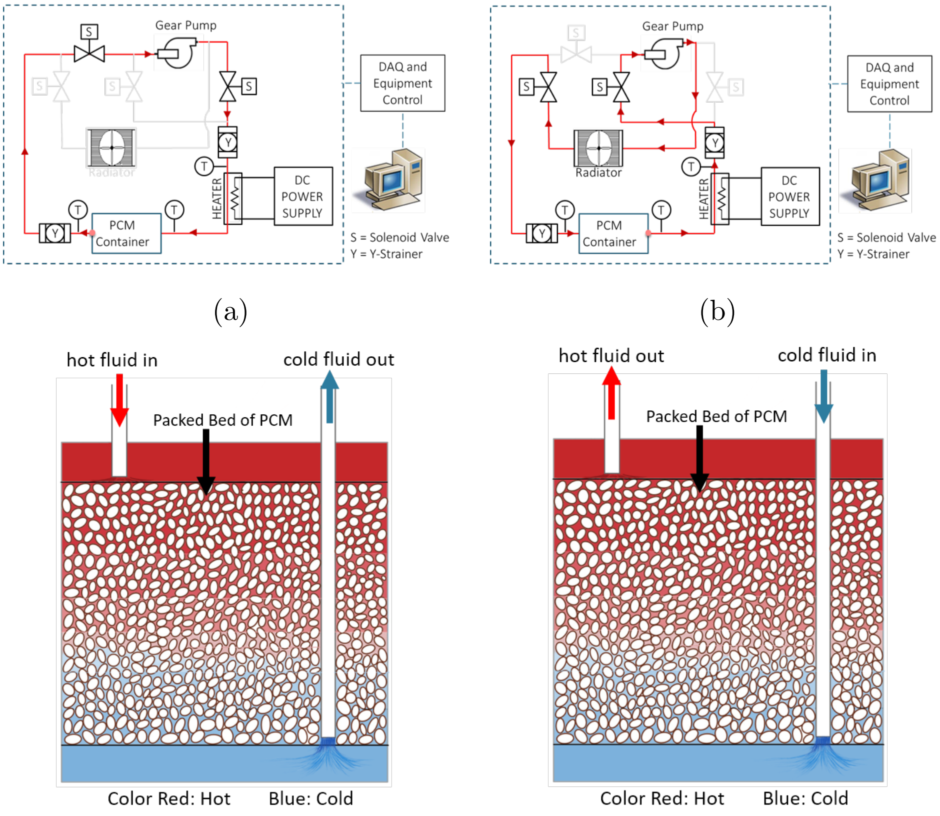

(a) (b)

(c) (d)

Figure 2.18: Schematic of flow loop while (a) charging and (b) discharging. Packed bed during (c) charging showing hot fluid enters from the top and colder fluid exits from the bottom, (d) discharging showing hot fluid exits from the top and colder fluid enters from the bottom maintaining a stable temperature gradient in the bed.

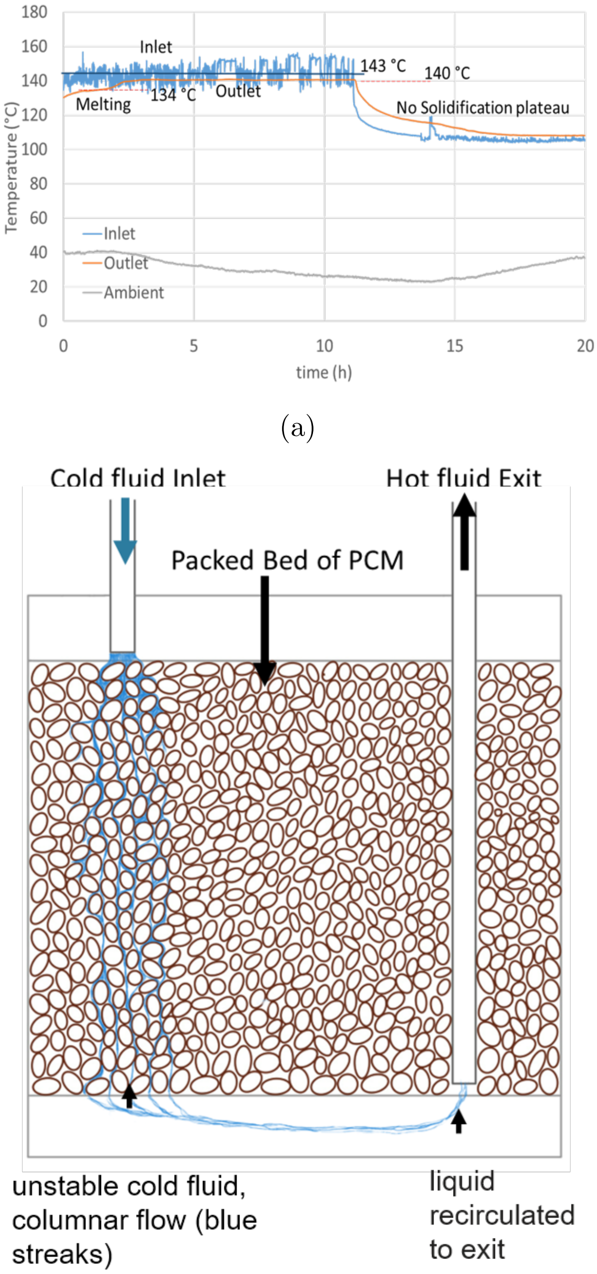

(a)

(b)

Figure 2.19: Bed behavior without flow reversal. (a) Temperature traces of the bed outlet shows that there is no clearly defined exotherm plateau as found during flow-reversal. (b) Schematic of packed bed during discharging without flow-reversal, showing cold fluid enters from the top and hot fluid exits from the bottom. Given low hydrodynamic resistance of the bed, it is likely that colder fluid now unstable because of its weight, falls down in a column within the bed and collects at the bottom.

TRICKLING FLOW TES

It is established that for a fully submerged bed, flow reversal is necessary. This requires a complex design of the flow loop and controls that automatically open and close valves during charging and discharging. In addition to this complexity, a major disadvantage of a fully submerged flow is the expense and weight of the heat transfer fluid in the containment. Weight can be a major hindrance for installation on building roof tops. One way of mitigating this issue is through trickling flow through the packed bed. Figure 2.20 shows a schematic of trickling flow in the packed bed system. A fine mesh is placed on the top of the packed bed that helps the heat transfer fluid to accumulate above the packed bed. The fluid slowly trickles through the packed bed due to gravity and collects at the bottom of the container below the platform holding the bed. There is direct contact heat exchange between the phase change media and the heat transfer fluid. There is no need of flow reversal in this case because buoyancy is not active. We need much less heat transfer fluid thus reducing the system weight and the cost significantly. Consequently, this TES system can be easily transported and installed. To build this system a platform with high to moderate hydrodynamic resistance is needed. Future work can involve implementation of this design and characterization of its thermal performance. The bed will be instrumented with multiple thermocouples to record the temperature of the bed axially, radially and the fluid inlet and exit from the bed for both charging and discharging. The effectiveness of the trickling flow compared to the fully submerged flow can be studied.

2.3.5 Comparison with Existing HDPE Latent Heat Storage Systems

A number of latent heat storage systems using HDPE and related materials have been demonstrated in literature. All show high capacity reflecting the large latent heat of highly crystalline HDPE. Table 2.2 compares the capacity (sensible + latent), charge/discharge temperature difference, and system form for several of these. The thermal capacity of these systems is similar when accounting for the sensible heat contribution. Past studies utilized larger $\Delta T_{c/dc}$ (e.g. 30 - 100 °C) than used here (e.g. 15 - 20 °C), which would imply lower exergetic efficiency as discussed above. However, this is apparently an operational choice rather than an intrinsic characteristic of the systems considered. All systems use approaches to minimize thermal diffusion distances in the low

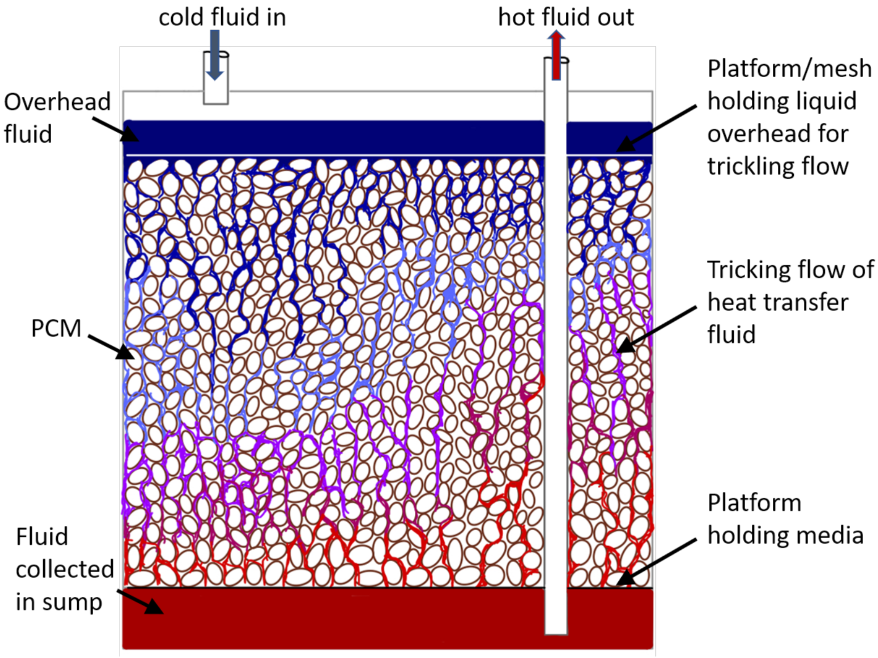

Figure 2.20: Schematic of a trickling flow of heat transfer fluid in the packed bed thermal energy storage system during discharging. Unlike the fully submerged system, the flow direction is not reversed, rather a unidirectional flow pattern is used.

conductivity PCM.

The primary difference between the current and previous work is the approach to maintain acceptable heat transfer across the melting transition. Here we use traditional fiber reinforcement and coating approaches to produce shape stable media. Zauner *et al.* [57], [58] applied a fin and tube arrangement to enhance heat transfer but found deformation of the fins due to thermal expansion of HDPE and also formation of voids between the PCM and fins. These effects may lead to increased maintenance cost and reduced performance. Further, the material and manufacturing costs of the fin and tube setup are likely to add substantially to the capital cost of the storage system. The co-polymer used by Abe *et al.* [56] and Kanimoto *et al.* [55] provides a degree of shape stability that allows direct contact heat exchange. However, to prevent the rods from bending at elevated temperatures special aluminum honeycomb structures for supporting the rods were required. Again the cost of extruded aluminum support is likely to substantially impact system cost. The cross-linking approach of Salyer and Davison [59] provides sufficient shape stability to allow packed bed operation without additional support. However, the electron beam processing approach requires highly specialized manufacturing capabilities. The stabiliza-

Table 2.2: Comparison with existing HDPE latent heat TES systems

Citation	Capacity	$\Delta T_{c/dc}$	PCM/Set-up
[59]	628.5 kJ/kg	100 °C	crosslinked HDPE, packed bed
[57], [58]	410.0 kJ/kg	50 °C	HDPE, fin tube exchanger
[56], [55]	420.0 kJ/kg	40 °C	ethylene-silicone copolymer rods simulating crosslinked HDPE
This work	420.0 kJ/kg	20 °C	HDPE composite, packed bed (145 °C charge)

tion approach presented here using fiber reinforcement and coating provides good mechanical and thermal stability in an unsupported packed bed configuration (currently tested to over 100 charge/discharge cycles). The application of traditional processing approaches provides ease of synthesis with widely available equipment. This is likely to provide benefits in system cost and scale up.

2.4 Conclusion

Storage of thermal energy is an important element in energy management, and latent heat storage systems have significant advantages in terms of their energy density and exergetic efficiency, i.e. low temperature difference between charging and discharging conditions.

Here we presented a low-cost, shape stable polymer composite latent heat storage media and a thermal energy storage system utilizing this composite. We stabilized high-density polyethylene via traditional composite formulation methods consisting of reinforcement with an inert filler and partial coating with rigid thermoset polymer. This approach offers a useful alternative to previously explored methods of stabilization such as crosslinking. This stabilization strategy yields media with excellent latent heat capacity for small media volume, mechanical and thermal stability, and compatibility with heat transfer liquids such as propylene glycol and glycerol. The media shows no significant deformation on melting and minimal migration of molten media during operation, due to the extremely high effective viscosity of the molten composite, strength of the fiberglass reinforcing phase, rigidity of the epoxy coating, capillary action of the filler, and minimal buoyant driving force.

The thermal energy storage system applies the composite phase change media in a packed bed with direct contact to the glycerol heat exchange fluid. This arrangement offers excellent heat transfer performance due to the low conduction resistance and high surface area enabled by the media shape stability and small feature size. We have characterized the effect of operational conditions (e.g. fluid flowrates and temperatures during charge and discharge) on energy storage and thermal power delivery. An optimal discharging rate for maximum energy extraction from the system was found for the particular packed bed system, but the system is capable of higher thermal powers with small penalties in efficiency. Importantly, the strong heat transfer performance allows low temperature difference between charging and discharging conditions. The high energy density and swift charge/discharge capability of the system offers potential to open new applications for thermal storage in medium temperature industrial applications.

Chapter 3

High Density Polyethylene Composite as Phase Change Material for Latent Heat Thermal Energy Storage - Pilot-Scale Experimental Study

3.1 Introduction

In Chapter 2, samples of a refined form-stable media from high-density polyethylene (HDPE) and reinforcement fibers were synthesized. It was established in the previous chapters that HDPE is an effective phase change thermal energy storage (TES) media for the operating temperature we are interested in (110 °C - 140 °C). Moreover, HDPE shows good thermal stability and limited supercooling. Also, it is largely inert in heat transfer fluids (HTF) like glycerol and propylene glycol. Previously, stabilization was achieved by reinforcement with glass fibers. Manufacturing of this previous composite formulation is sensitive to base material viscosity and the melt flow index. To address manufacturability concerns, a refined media design is developed and synthesized.

3.2 Approach

This section provides an overview of the PET-HDPE composite as well as the design and setup of a pilot-scale TES system. The system allows quantification of the energy storage and thermal performance of the phase change material (PCM) under conditions appropriate to applications. Additionally, we present an methods to determine the long-term form stability of the media.

3.2.1 Media

The composite media is developed for application in large scale TES systems. We deploy the composite as relatively larges plates with thickness 1.3 cm and lateral dimension of 58 cm × 53 cm or 29 cm × 53 cm formed from HDPE pellets and bonded polyester batting. In this subsection, we outline the constituent materials and detail the manufacturing process for the composite PCM plates.

COMPONENTS

Post consumer recycled HDPE resin (Talco Plastics, Inc.) serves as the phase change element. Natural color resin is sourced as biconvex disc-shaped pellets. Its density at ambient condition is 0.95 g/cm^2. The density of molten HDPE is 0.76 g/cc [129]. The reinforcement phase is 100% recycled polyester fiber fill (Poly-Fil Heavy/Mid-Weight Batting from Fairfield Processing, CT, USA) used in textile applications [130]. The polyester batting has an aerial density of 0.16 kg/m^2, whereas polyester has a solid density of 1.38 g/cc [131].

MEDIA DESIGN

The selection of suitable materials for the composite media is crucial. We opt for HDPE as the thermal energy storage medium, owing to its significant latent heat capacity and a melting point that conforms to our desired operating range along with the cost and chemical compatibility benefits discussed previously. HDPE forms the bulk of the composite (80% by weight).

Polyester batting is chosen as the matrix to contain the melted HDPE. It acts as an inert filler. The PET fibers provide minimal mechanical resistance to deformation. Capillary pressure serves to hold the molten media in place with the batting acting as a sponge. The polyester batting has a high melting point, which is well beyond our system's operating conditions. It is nontoxic and remains nonreactive with HDPE and our chosen heat transfer fluid, glycerol, within the working temperature range. In this study, the polyester batting comprises 20% of the composite by weight. We anticipate that future studies may vary the ratio active material/filler ratio to optimize thermal performance and long-term stability. Based on the current composition the composite density is 0.835 g/cc, when HDPE is molten. Density of glycerin is 1.2 g/cc at 125°C. This results in a composite that is slightly buoyant under operating conditions, which is advantageous for preventing the leakage of molten HDPE. Initially, our aim was to create a neutrally buoyant medium; however, achieving this would require a composition of 82% PET, significantly reducing the media's energy storage density.

The geometry of the media elements (large, thin plates) was chosen based on a variety of design constraints. These include thermal performance, manufacturability, energy density, system cost, and HTF flow. Thin plates inherently present low thermal conduction resistance along the thickness of the media, the dominant direction of heat transfer during operation, as do elements with smaller lateral extent, such as pellets. As discussed below, however, large plates also show advantages in ease of manufacturing for the composite compared to smaller elements that are often implemented [59], [132]. Additionally, large plates provide a means to strategically control the bed porosity through careful plate arrangement, whereas a bed composed of randomly placed smaller pellets generally results in increased porosity, diminishing the energy density for a TES unit and affecting the system compactness. Larger containment, insulation, and heat transfer fluid volumes incur additional costs. The regular form of the plates also provides control of HTF flow through the bed. Thus, our plate design represents an optimization of both cost and thermal performance, allocating more resources to the PCM material compared to the auxiliary components of the system.

In the design of the composite plates, attention was paid to the edges, which are exclusively composed of polyester batting. This design choice enhances capillary retention at the periphery, effectively reducing the likelihood of molten HDPE migration and potential adhesion to adjacent plates.

MEDIA SYNTHESIS

PCM plates are produced using a batch process via a heated press. A continuous process is proposed and discussed later.

Figure 3.1 shows the composite media synthesis process. Part (a) is a schematic representation of the stacked layers inside our heated press, detailing the organization of polyester batting and HDPE pellets as well as the final compressed composite plate. Spacers determine the thickness of the end product.

Part (b) shows photos of actual assembly. The left image displays HDPE pellets evenly spread on a layer of polyester batting, while the right image presents an assembled stack of materials, separated by a PTFE Teflon sheet. This image was taken while creating a small-scale prototype composite element.

For full scale PCM plate production, we constructed a large heated press with aluminum platens, stops, and threaded rods for pressure application. This full-scale press has a footprint of approximately 0.75 m × 0.75 m and is equipped with three heaters on the top and bottom platens, and two heaters in the center of the assembly. This arrangement ensures symmetrical heat distribution in the vertical direction. The power to the heaters is controlled using a computer-controlled relay. We recorded the temperature of each platen and the heaters using K-type thermocouples connected to a data acquisition system linked to the computer. We set the heater and plate temperatures to a maximum of 185 °C to prevent charring of the media due to overheating.

Figure 3.2 shows the press in operation, with 10 stacks of constituent materials (each corresponding to a single media sheet) between aluminum platens before compression. Each layer of composite consists of 10 layers of polyester batting and nine layers of HDPE, alternately placed between the polyester layers. We spread out HDPE beads on top of the batting to create a relatively uniform layer of HDPE.

We attached Unistrut to the bottom and top platens and placed 1/2 -inch threaded rods to provide compression. Spacers were used between plates to define the final thickness of the consolidated composite sheet. We maintained a compressive force on the stack using springs. This ensured a continuous load on the stacks as the materials consolidated and eliminated the need for frequent tightening of the nuts to apply pressure.

With this configuration and proper insulation, we obtained ten consolidated plates of the final composite in a single press. We supplied the press with electrical power for around 7.5 hours, after which we allowed it to cool down to room temperature over the next 10 hours under the influence of externally applied loads. Although it is possible to process more plates in a single press run, the throughput of the press is constrained by the time it takes for heat to

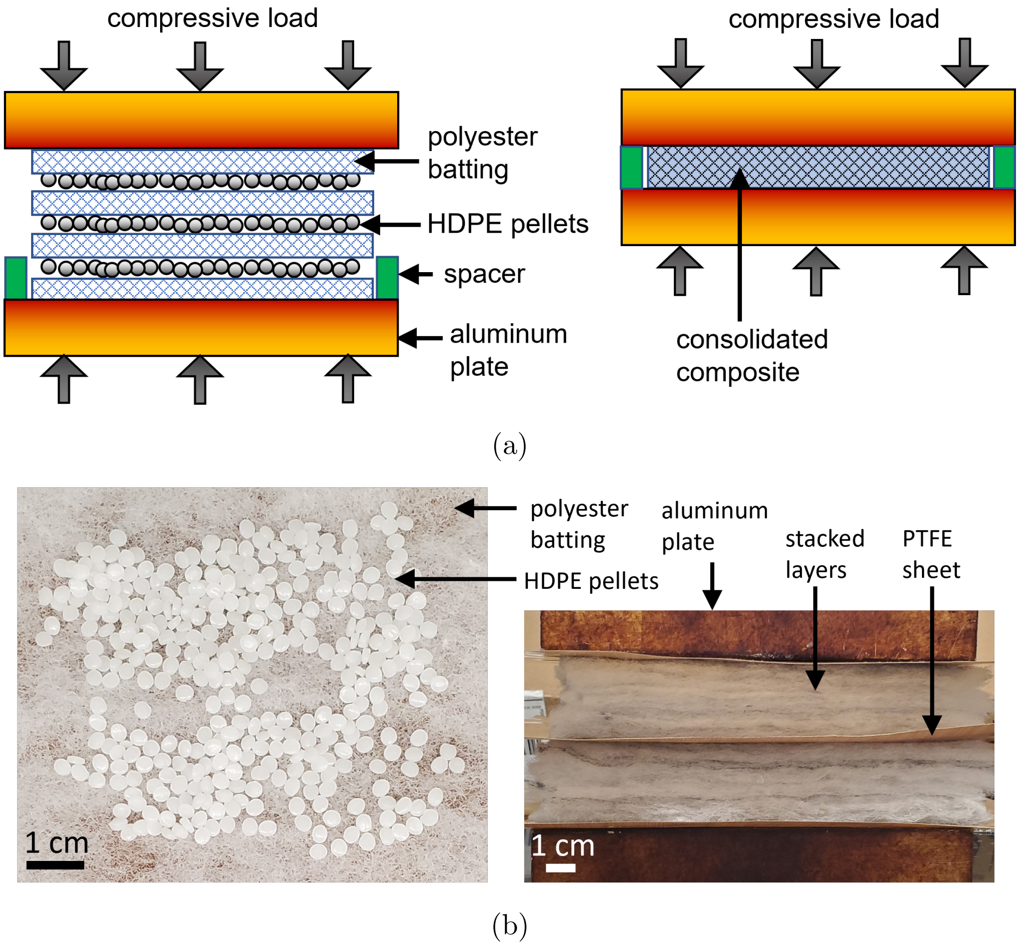

Figure 3.1: Composite media production setup and components. (a) Schematic of the composite media layers inside the heated press, indicating a selection of the polyester batting and HDPE pellet layers. A total of 10 layers of polyester batting and 9 layers of HDPE pellets are used in the actual setup, though only 4 layers of batting and 3 layers of HDPE are illustrated here for simplicity. Also shown is the consolidated composite plate post-press, with thickness determined by the height of the spacers used between the two aluminum heating plates. (b) Actual ingredients and assembly of the composite media. On the left is a demonstration of HDPE pellets spread over a layer of polyester batting. On the right is an image of two stacks of the materials (before compression), separated by a PTFE Teflon sheet, taken during the construction of a small-scale prototype composite.

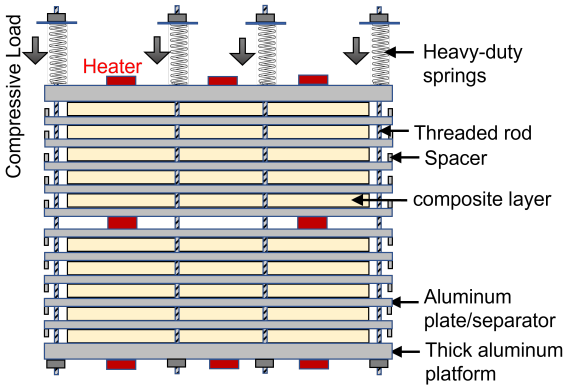

(a)

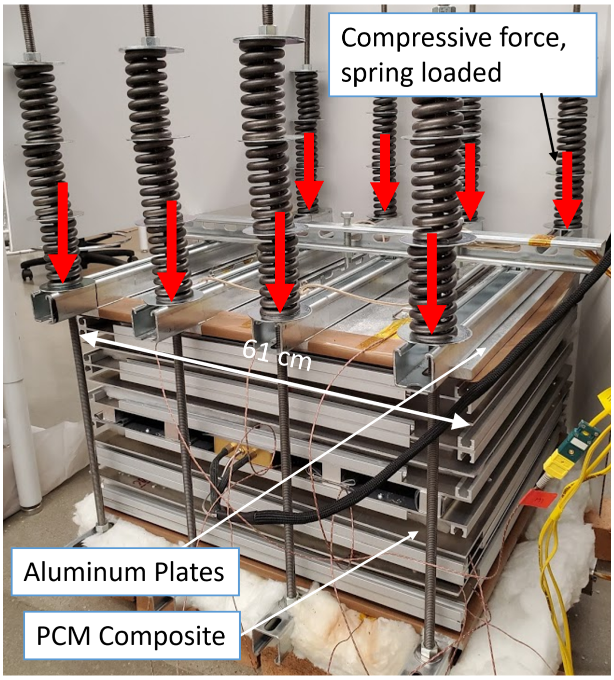

(b)

Figure 3.2: (a) Schematic of the custom-made, large heated press used for composite media sheet production, and (b) the final assembly of the full-scale setup. The press features a footprint of approximately 0.75 m × 0.75 m and is equipped with five heaters ensuring symmetrical heat distribution. The production setup consists of ten stacks of alternating layers of polyester batting and HDPE, each constituting a single media sheet. Unistrut attachments and threaded rods are used for compression, while spacers determine the final thickness of the consolidated composite sheet. The temperature and power to the heaters are controlled and monitored via a computer-controlled relay and K-type thermocouples.

diffuse into all the layers due to the poor thermal conductivity of the materials used.

3.2.2 Pilot Scale Storage System

In this section, we present a pilot scale thermal energy storage system that utilizes the composite PCM for efficient heat storage. A key feature of this system is a carefully engineered packed bed, essential for both storing and transferring heat. The packed bed system is housed in a stainless steel storage tank and fully submerged in glycerol. The bed is structurally supported at the top and bottom. The plate arrangements in the bed allows for unimpeded flow of the heat transfer fluid throughout the system. During operation, the system functions as a flow loop calorimeter. Hot fluid is delivered to the top of the bed during the charging phase, while colder fluid is extracted from below the bottom platform. To maintain hydrodynamic stability, the flow direction is reversed during the discharging phase.

A schematic of the thermal loop and controls for this system is shown in Figure 3.3a. This flow loop features a unidirectional gear pump that feeds two flow paths, which can be switched using four ball valves to control flow direction at the bed. The system is charged via a 2.4 kW electric heater and discharged to a water cooled compact heat exchanger, which generates steam during operation. Figure 3.3b shows an implementation of the full-scale TES system. The entire setup is located outside of a climate-controlled area.

PACKED BED DESIGN

The system uses a 1325 liter (350 gallon) pre-fabricated industrial bulk carrier (IBC), formed from stainless steel, for containment, thereby ensuring high-temperature operation without the risk of corrosion. The base of the tank measures 112 cm × 122 cm (44” × 48”), and its overall height is 119 cm (47”). The containment is modular allowing system expansion without significant design changes. We installed a perforated aluminum beam structure on the tank floor to support the weight of the composite plates when HTF is not present. Medium-sized stone pebbles (approximately 3-4 cm in diameter) were used as fillers up to the height of the aluminum beam top surfaces to reduce the amount of glycerol required to fill the empty space below the media. We then placed an aluminum mesh, 0.8 cm thick, on top of the structure to uniformly support the composite plates. The combined height of the structure and aluminum platform

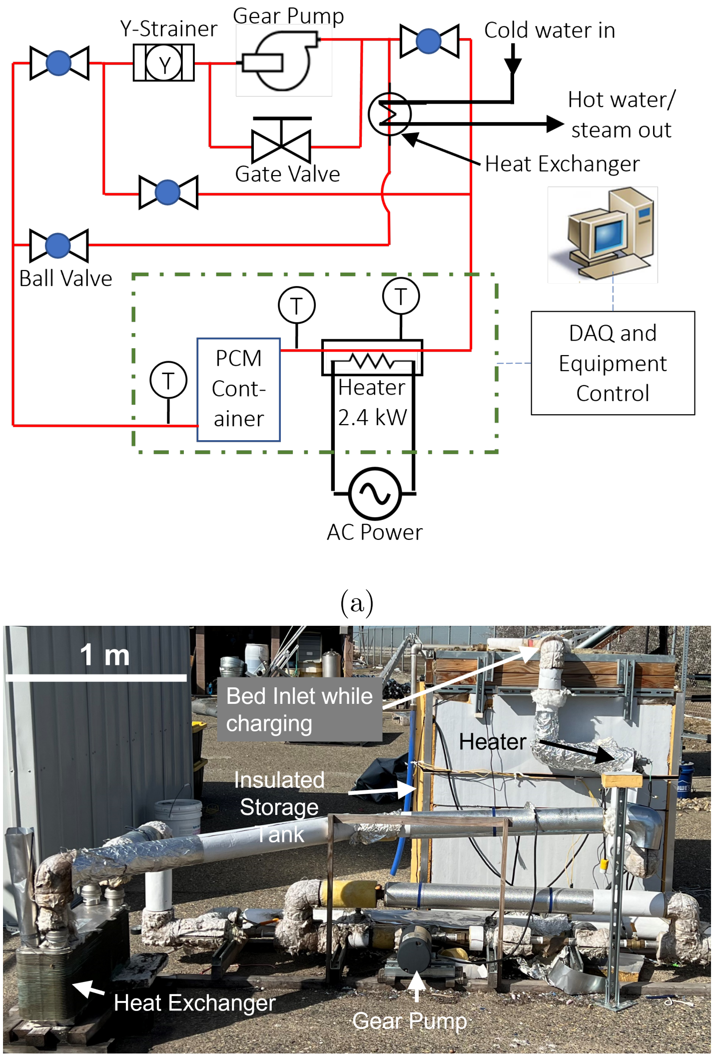

(a)

(b)

Figure 3.3: (a) Schematic of the thermal energy storage system featuring a unidirectional gear pump, which facilitates two flow paths that can be manually switched using four controlling ball valves. (b) A fully insulated, full-scale TES system with an inline heater installed for media charging. The packed bed, comprising strategically arranged composite plates, is contained within a stainless-steel tank. The bed is designed for unimpeded flow of the heat transfer fluid and minimized porosity for increased storage capacity. The entire system is located outside of a climate-controlled area.

Table 3.1: Media Size and weight

Media Size (cm)	Weight (Kg)
58 × 53 × 1.3	2.7
29 × 53 × 1.3	1.35

is approximately 100 cm.

The PCM is held in the containment vessel between the aluminum platform at the bottom, and a galvanized steel hardware cloth at the top, surrounded by glycerol, a low vapor pressure heat transfer fluid. Additionally, to ensure that the PCM is fully submerged in the glycerol, several weights are placed uniformly on top of the hardware cloth. This setup requires the addition of about 168 kg of glycerol to the tank.

Figure 3.4 portrays the refined media layout in the containment vessel. Production in a press allows us to make plates that are relatively regular and can be easily placed into the container and separated, as shown, by wire mesh to ensure that there is a flow path between the plates. This arrangement reduces porosity compared to a random media bed, thereby minimizing the liquid volume and maximizing capacity within a single container. Consequently, the weight, cost, and heat loss due to external surface area of the final system are all minimized.

As demonstrated in Figure 3.5, the plates must be arranged to ensure a well defined flow path throughout the bed. For uniform flow in the bed, we create two plate arrangements, which are stacked alternately. The gaps between the tiles in this design do not overlap. This layout necessitates creating two different sizes of tiles, as shown in Fig. 3.5 and Table 3.1.

Figure 3.6a illustrates the wiremesh separating assembly, which includes two types of mesh materials: a 23-gauge durable galvanized steel hardware cloth with a 1/4 in. mesh size and 14-gauge galvanized steel welded wire fencing material with a rectangular mesh opening of 5 cm × 10 cm (2 in. × 4 in.) Figure 3.6b provides a side view of this arrangement. To ensure adequate flow, we placed the coarser mesh sandwiched between two finer meshes, with a separation measuring at least 3 mm when they lay flat on top of each other. When assembled outside the bed, the spacing between the cloths was approximately 5 mm due to deformation on hanldling, but we expect the forces applied by the media to maintain a separation closer to the designed 3 mm. The wiremesh arrangement with small openings offers several advantages. Firstly, it promotes mixing

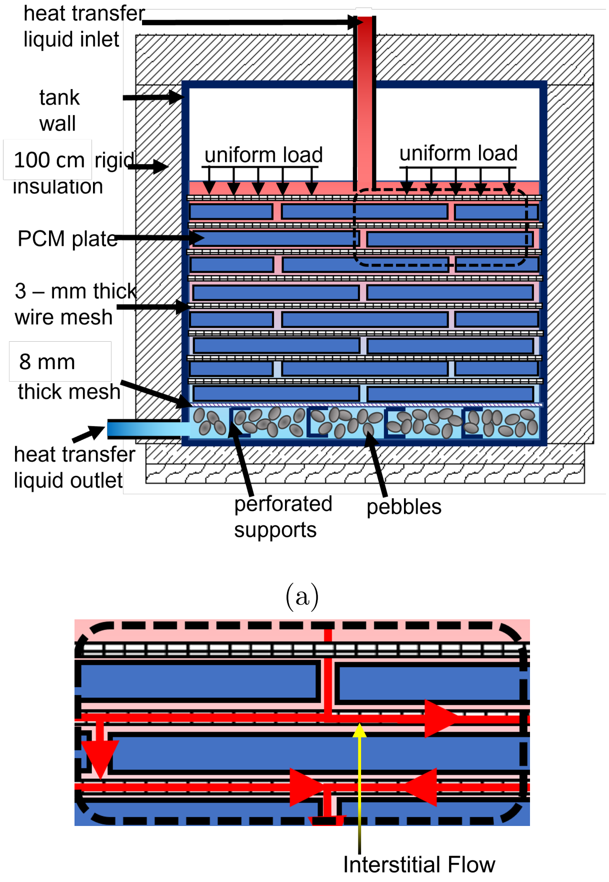

(a)

(b)

Figure 3.4: Detailed overview of the thermal energy storage system and its functioning: (a) A system schematic situated in a 350-gallon stainless-steel IBC, displaying the strategic arrangement of composite plates, supported by a unistrut structure and a thick aluminum mesh. The schematic also illustrates the containment of PCM surrounded by glycerol, the color gradient denoting fluid temperature distribution, and the insulation measures adopted for reducing heat loss. (b) A closer look at the bed, revealing the serpentine interstitial fluid flow amid the plates. This tailored design fosters optimized system parameters, including porosity, liquid volume, capacity, weight, cost, and heat loss.

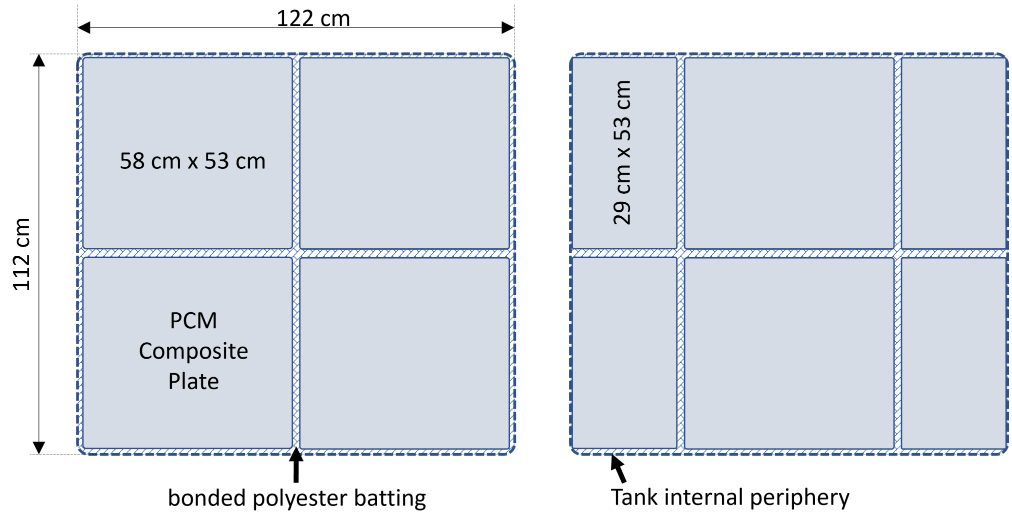

Figure 3.5: Tiling design for alternate stacking in the bed. Gridlines represent the border of each composite block through which HTF will flow. HTF flow will be directed along the edges of the blocks. Serpentine flow is expected due to offsetting gaps.

of the fluid as it passes over and through the meshes. This results in an increased heat transfer coefficient between the fluid and the composite. Moreover, the rigid structure of the wiremesh ensures that the composite plates maintain a gap and do not touch each other, preventing fluid flow restriction.

Straight and rigid stainless-steel pipes with a 2-inch external diameter carry the heat transfer fluid to and from the bed. The pipe that enters the tank from the top extends below the liquid level, ensuring that no air is entrained during discharge. We placed two thermocouples inside the tubes to measure the fluid temperature at the inlet and outlet; these are positioned at the entrance of the containment vessel. The media bed in the loop employs an inline flow heater attached to an AC power supply to heat the transfer fluid during charge and discharge. To maintain hydrodynamic stability, flow reversal is crucial for a fully submerged packed bed system [56]. The hot fluid is delivered to the top during charging, while the colder fluid exits from below the bottom platform to prevent local convection in the bed. We use a liquid-liquid heat exchanger as a thermal load during discharge.

To address the parasitic heat loss to the environment, the vessel is insulated with polyisocyanurate foam and rock wool. Relevant thermophysical properties for the experiments are provided in Table 3.2.

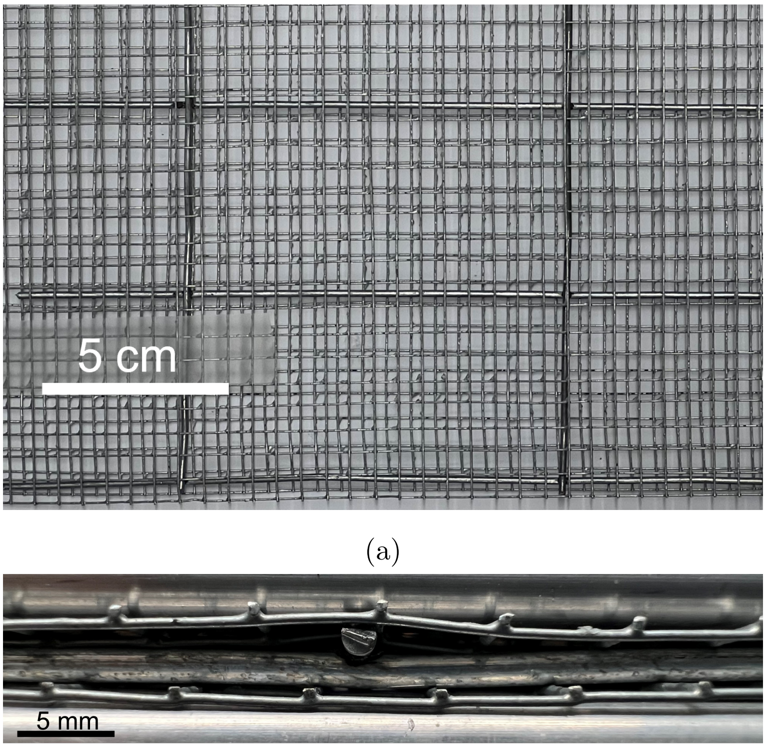

(a)

(b)

Figure 3.6: Detailed illustration of the wiremesh assembly used in the thermal energy storage system: (a) Top view showing the combination of a 23-gauge galvanized steel hardware cloth with a 1/4 in. mesh size and a 14-gauge galvanized steel welded wire with a 5 cm × 10 cm rectangular mesh opening. (b) Side view of the layered arrangement featuring the coarser mesh sandwiched between two finer mesh cloths, providing a minimum opening of 3 mm, ensuring adequate fluid flow. This wiremesh setup enhances surface roughness, promoting turbulent flow, thus increasing the heat transfer coefficient and maintaining necessary gaps between composite plates to avoid fluid flow restriction.

SYSTEM CONTROL

The packed bed configuration was tested at a fixed charge/discharge rate. The gear pump maintained a steady RPM, and we manually adjusted a gate valve in the bypass loop to attain the desired mass flow rate of the heat transfer fluid. Full power was supplied to the heater in the thermal loop during bed charging only. We controlled the flow direction during charging and discharging by manually manipulating control valves shown in Fig. 3.3a. We used K-type thermocouples from Evolution Sensors and Controls, LLC to measure temperature. These were connected to a temperature input module (National Instruments, NI-9211) of a compact data acquisition chassis (National Instruments, NI cDAQ-9172) controlled by a personal computer.

THERMAL CYCLING PROCEDURE

At the start of the charging phase, the temperature of the packed bed is maintained at 110 °C. Both flow heaters operate at their maximum power (2400 W), progressively heating glycerol until it exceeds the melting point of HDPE. The charging phase concludes once the bed outlet temperature rises significantly above the PCM's melting point, elevating the fluid inlet temperature from 110 °C to 145 °C.

Immediately following charging, we initiate the discharging process by reversing the heat transfer fluid flow direction and discontinuing the use of the heaters. Glycerol, is routed through a heat exchanger, where it transfers heat to flowing tap water. The HTF now at a temperature lower than that of the media's recrystallization temperature, is introduced at the bottom of the packed bed. The discharging process continues until the outlet temperature falls significantly below the PCM's solidification temperature.

3.2.3 Thermal Characterization

Thermal performance characterization of the system was performed via calorimetry experiments during discharge.

BULK CALORIMETRY CHARACTERIZATION

The rate of heat transfer to the TES system is calculated using calorimetry of the flow and is represented by the product of the mass flow rate ($\dot{m}$), the fluid's specific heat (c), and the temperature difference between the fluid inlet to (T_{in}) and outlet of (T_{out}) the bed (equation 3.1). The total heat capacity of

Table 3.2: Thermo-physical properties of HDPE and glycerol.

Properties	Value	Units
HDPE Melt Flow Rate (190 °C/2.16 kg)	0.8	g/10 min
HDPE Density (23 °C)	≥ 0.96	g/cm^3
glycerin (pure) specific heat (127 °C)	3.09	kJ/kg/K
glycerin (pure) viscosity (127 °C)	0.00686	Pa.s
glycerin (pure) density (127 °C)	1195.3	kg/m^3

the system is determined by integrating the rate of heat extracted during solidification and the rate of parasitic heat loss from the system to the ambient over time (equation 3.2).

$$q_{\text{flow}} = \dot{m}c(T_{\text{out}} - T_{\text{in}}) \tag{3.1}$$

$$\begin{aligned} Q_{\text{ex}} &= \int_{t_1}^{t_2} (q_{\text{flow}} + q_{\text{loss}})dt \\ &= \sum_{i=1}^{N-1} (\dot{m}c(T_{\text{out}_i} - T_{\text{in}_i}) + q_{\text{loss}})(t_{i+1} - t_i) \end{aligned} \tag{3.2}$$

Here, N represents the total number of experimental data points collected during the discharging process between two temperature points defined at times t_1 and t_2. The difference between these two times corresponds to the discharging time. The average power extracted, P_{ex}, is given by equation 3.3.

$$P_{ex} = \frac{Q_{ex}}{t_2 - t_1} \tag{3.3}$$

The heat loss rate of the bed is calculated by determining the total energy loss over a selected time period, between t_a and t_b, when the system is in an entirely molten state. This is obtained by integrating the product of the temperature difference between the fluid inlet and exit, the mass flow rate, and the specific heat of glycerol over the selected period. The average heat loss rate, q_{loss}, is then calculated as the total energy loss divided by the duration of the steady-state period. Equation 3.4 below presents the calculation of the average heat loss rate.

$$q_{\text{loss}} = \frac{\int_{t_a}^{t_b} \dot{m}c(T_{\text{in}} - T_{\text{out}})dt}{t_b - t_a} \tag{3.4}$$

ERROR ESTIMATION FOR THERMAL PERFORMANCE

The estimated uncertainty in the determination of system heat capacity is attributable to several sources. Each are considered here.

Thermocouples display an estimated error of ±0.15 °C relative to each other, based on the prior calibration. However, compared to other factors influencing energy measurements, this uncertainty is relatively minor. Hence, error bars for temperature readings are not displayed. The uncertainty in time measurement is likewise considered insignificant.

The determination of mass flow rate of the heat transfer fluid contains an uncertainty of ±2%, based on measurements of total flow volume (by diverting flow from the loop) and time at the relevant viscosity and density. The specific heat of glycerol slightly fluctuates within the temperature range of this study, with a variation of ±1%. Consequently, we use an average value of 3.09 kJ/kg/K for all energy and power computations. These errors in flow measurement and the thermophysical properties of the heat transfer fluid contribute to an overall uncertainty of ±3% in the energy and power values.

However, the major contributor to uncertainty in energy and power calculations is heat loss to the ambient environment. The instantaneous parasitic heat loss, calculated during media charging, ranges from 0.9 kW to 1.8 kW (4.9 W/kg to 9.8 W/kg of media), depending on environmental conditions. For a conservative approach to our energy and power calculations, we use the minimum heat loss rate of 0.9 kW (4.9 W/kg). Employing a higher parasitic heat loss rate would lead to a larger calculated value for stored energy.

The energy and power values reported in this study have upper and lower bounds, which are determined by several contributing factors: parasitic heat loss, flow measurement, and thermophysical properties. The lower bound is 3% less than the declared value, calculated using the minimum heat loss rate to the ambient environment. Conversely, the upper bound is 3% greater than the energy/power value calculated with the maximum ambient heat loss rate of 1.8 kW (9.8 W/kg).

THERMOCOUPLE CALIBRATION

We calibrated all thermocouples while they were connected to the data acquisition system. To ensure a uniform temperature environment, we utilized an aluminum block measuring 150 mm x 150 mm x 25 mm. This block featured holes of approximately 50 mm in length and a diameter slightly larger than the thermocouple probe diameter. These holes were drilled close to each other, perpendicular to the narrow axis of the block. We used a small amount of thermal interface compound (Arctic MX-4) to minimize contact resistance with the thermocouple probes. The block was heated to 190 °C on a hot plate and held steady. We recorded temperatures while the block remained at a steady state and as it was allowed to cool down slowly. For calorimetry purposes, we selected two thermocouples that provided the closest overall readings to measure the fluid inlet and exit temperatures, with a maximum observed difference of 0.15 °C during calibration.

3.2.4 Media Stability Characterization

To ensure suitable heat transfer performance in the packed bed TES system, it is crucial to maintain the shape of the composite plates while they are in their molten state and prevent consolidation of the bed. Moreover, it is essential to prevent the migration of the molten HDPE within or outside of the media, which can impede the flow of heat transfer fluid and lead to poor local heat transfer performance. We have addressed these issues by using partially bonded polyester fibers in the form of batting to stabilize the media against deformation or melt migration during operation. To minimize melt flow, we use HDPE with a low melt flow index characteristic of HDPE recycled from blow molded containers.

Although the low melt flow index (conversely, the high viscosity) of HDPE influences the kinetics of melt flow, ensuring a protracted duration for any melt flow escaping the polyester batting, the governing parameter for system equilibrium is the capillary pressure exerted by the partially bonded polyester batting. Specifically, when the applied external load remains below or equal to the established capillary pressure, the molten HDPE will reach an equilibrium state, thereby precluding any leakages from the batting.

The polyester batting acts as a sponge, retaining the molten HDPE due to its highly non-polar surface and enhancing the mechanical integrity of the composite in its molten state.

In the subsequent sections, we delve into two methods for characterizing media stability: leakage testing and equilibrium melt retention testing. The leakage testing focuses on the structural resilience of the media under designated operating conditions, whereas the equilibrium melt retention testing quantifies the media's capacity to retain molten material under a range of external com-

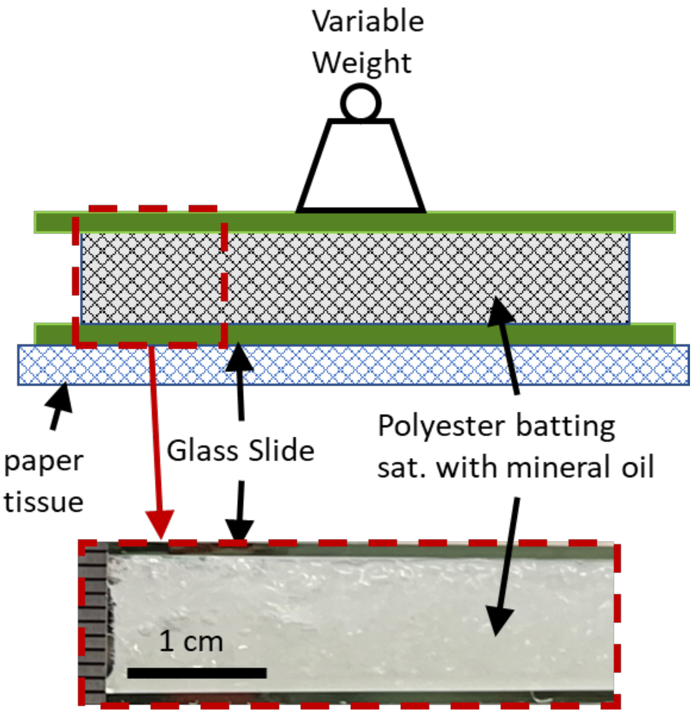

Figure 3.7: Experimental setup to investigate the melt retention capacity of HDPE within polyester batting under external load. A polyester batting sample is saturated with paraffin oil (an analog for molten HDPE) and sandwiched between two glass slides (5 cm x 7.6 cm) with load applied to the top slide. A microporous paper tissue is positioned beneath the setup to collect any oil seeping from the batting. External weight is added on top. The lower portion shows a picture of the batting saturated with paraffin oil during testing.

pressive stress. Collectively, these methods furnish a multifaceted evaluation of the media's stability.

Prototype plates of dimensions 15.2 cm × 15.2 cm (6” × 6”) were fabricated, mirroring the full-scale media composition without allowing HDPE to spread to the edge.

We trimmed one side of the prototype plate to expose various layers of HDPE and polyester for the consolidated composite. While they are mostly well merged, there are areas where the polyethylene is not fully integrated into the polyester batting. The trimming exposes this HDPE, enabling us to test for extrusion under compression of about 0.67 kPa, which is a representative pressure of the real-world scenario in the final configuration. The sample is maintained at 150 °C in glycerol for a duration of 24 h.

We performed experimental studies to determine the melt retention capacity of HDPE within the polyester batting. We measure the mass of liquid retained in the batting under an external load at equilibrium. For this investigation, a sample of polyester batting, with an areal density of $0.16\,\mathrm{kg/m^2}$ and a thickness of 1.5 cm, is utilized. Paraffin oil (commercially known as mineral oil), having a density of 860.2 $\mathrm{kg/m^3}$, is employed as an analog for molten HDPE. As alkanes, both HDPE and paraffin oil possess similar surface and interfacial energy properties. However, paraffin oil exhibits a significantly lower viscosity compared to molten HDPE, thus enabling it to attain equilibrium much more rapidly. The implications of this particular characteristic are explored in detail in Section 3.3.1.

The polyester batting sample was first saturated with mineral oil and placed between two glass slides of size, 5 cm × 7.6 cm (2" × 3"), as illustrated in the Figure 3.7. A microporous paper tissue was positioned beneath the bottom glass slide (ensuring no direct contact between the paper and the saturated batting) to collect the liquid that seeped out from the batting. After allowing sufficient time for the mineral oil to wick throughout the batting, additional weight was placed on the top glass slide. This caused more oil to ooze out of the batting and get absorbed by the paper towel at the base. Once the system reached a steady state condition under the given load, which took approximately 2 hours, the external weight on top was removed and the weight of the oil-saturated batting was measured. This process was repeated while increasing the weight on top of the upper glass slide.

The polyester batting serves as a sponge, retaining mineral oil while being subjected to external compressive stress. To analyze this phenomenon, we use the Young-Laplace equation, which provides insights into the pressure differences at the liquid-gas interface within the sponge's pores:

$$\Delta P_{yl} = -\gamma \left(\frac{1}{R_1} + \frac{1}{R_2} \right) \tag{3.5}$$

Equation 3.5 highlights the role of the liquid's surface tension (γ) and the principal radii of curvature of the interface (R_1 and R_2) in determining the pressure difference (ΔP_{yl}).

At equilibrium or steady state, the external compressive stress applied to the sponge (P_{external}) should be equal to the capillary pressure or the Young-Laplace pressure (ΔP_{yl}) within the sponge. This equilibrium prevents further oil flow out of the sponge.

In this context, the relationship between the external compressive stress and the Young-Laplace pressure can be expressed in Equation 3.6.

$$P_{\text{external}} = \Delta P_{yl} \tag{3.6}$$

With data points of external compressive stress (P_{external}) and the mass of oil retained from the sponge at steady state, we can gain insights into the sponge's behavior.

3.3 Results and Discussion

This section presents an evaluation of the performance of the phase change media composite and the TES system. Initially, an analysis of the media composite is provided, encompassing latent heat measurement via differential scanning calorimetry tests and stability assessments. The focus then shifts to the TES system, considering the overall system performance within a fully-immersed packed bed context. Particular attention is given to aspects of thermal storage capacity and charge-discharge temperature differentials. The section culminates in a comparison with established HDPE latent heat storage systems, positioning the unique characterisitc of these materials and systems within the broader context of latent heat storage technology.

3.3.1 Media Performance

Figure 3.8 illustrates a full-scale composite plate after pressing. The media is well consolidated, with polyester constituting 20% of the composite's total mass. Additional polyester batting around the edge prevents HDPE from spreading beyond the media boundary.

MEDIA THERMAL CAPACITY

To characterize the latent heat of fusion of the media, we conducted differential scanning calorimetry (DSC) experiments on the pure HDPE material in pristine conditions using a Perkin Elmer Jade calorimeter. The experimental procedure adopted in this study follows the methodology detailed in our previous work [132]. The DSC thermogram presented in Fig. 3.9 reveals that the latent heat of fusion for the pristine HDPE is 192 J/g. The diagram illustrates a complete melting/solidification cycle. A melting temperature of 133.9°C corresponds to the maximum endotherm, and a crystallization temperature of 120°C corresponds to the maximum exotherm is recorded. The presence of a substantial

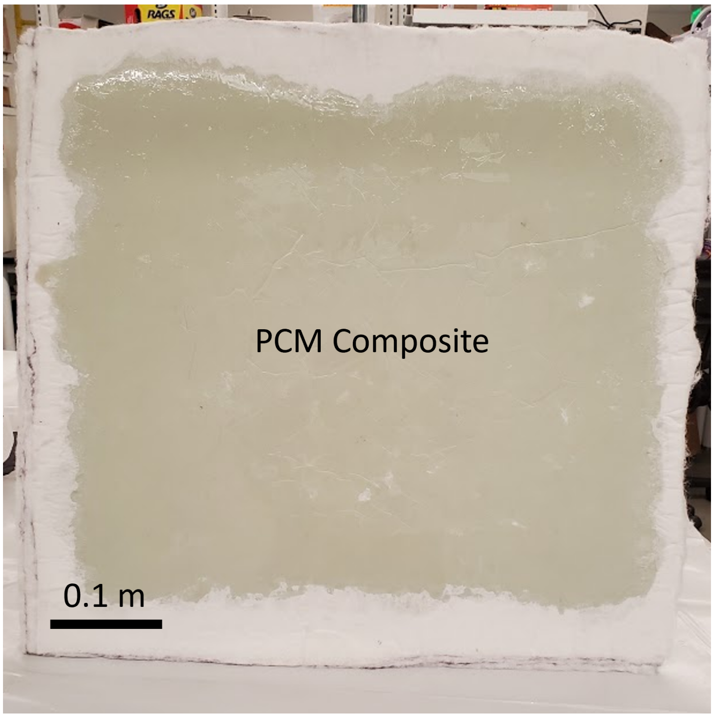

Figure 3.8: Phase change media for the TES system (as synthesized). The composite is approximately 1.3 cm thick and 58 cm × 53 cm (23” × 21”) on the sides, consisting of 10 layers of polyester batting and 9 layers of HDPE. The layers were subjected to high pressure and temperature (160 °C) till fully consolidated. The plates were formed without HDPE spreading to the edge.

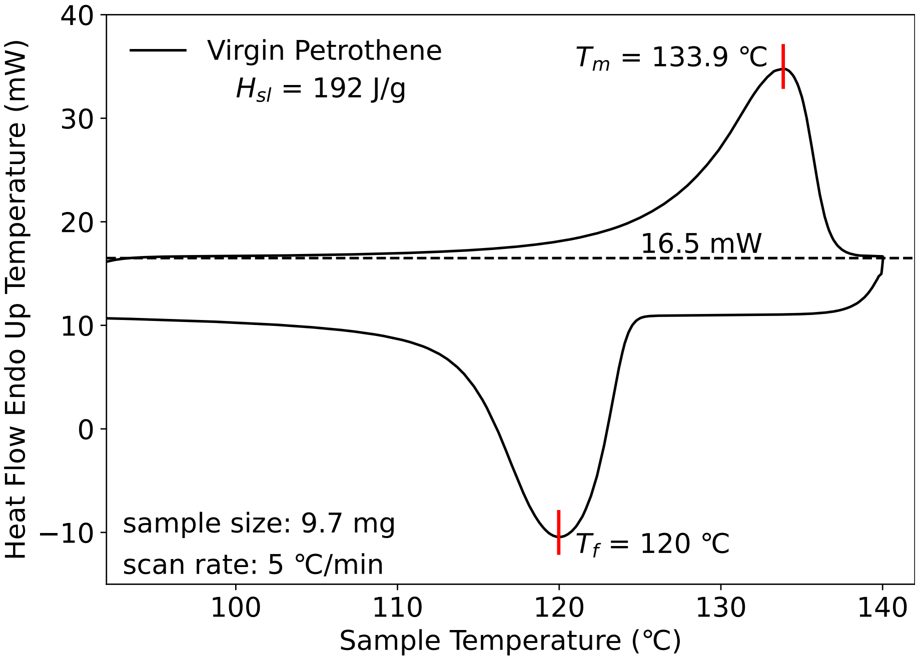

Figure 3.9: Thermodynamic characterization of the pristine HDPE media performed through DSC. The calorimetry procedure involved heating and cooling the sample between 90°C and 140°C at a rate of 5°C/min. The DSC thermogram reveals a latent heat of fusion of 192 J/g for the HDPE, demonstrating a complete melting/solidification cycle with peak temperatures of 133.9 °C for melting and 120 °C for crystallization. The notable hysteresis between these temperatures, largely due to the rapid temperature change rate, is anticipated to be less pronounced under operational conditions.

hysteresis between these temperatures is discernible. This hysteresis, however, can largely be attributed to the swift rate of temperature change, given the scanning rate of 5°C/min is substantially more rapid than what is typically observed under operational conditions. Consequently, we predict a reduced local hysteresis at operational heating and cooling rates.

The latent heat of the HDPE component is dominant in the system thermal behavior, but the total system thermal capacity also includes sensible contributions from all components. A more comprehensive understanding of these elements, and consequently the total thermal capacity of the media, is developed in Section 3.3.2, where we discuss bulk calorimetry tests and the resulting insights into the system's behavior.

MEDIA STABILITY

Media stability is of utmost importance for the reliable operation of a thermal energy storage system. This implies maintaining the shape of the composite plates when in a molten state, minimizing HDPE migration, and preventing the consolidation of the packed bed. In Section 3.2.4 we outlined two techniques for assessing the stability of the composite media: leakage testing and equilibrium melt retention testing. In this section, we present our findings on media's long-term stability and resistance to leakage based on these methods.

Figure 3.10 shows the prototype media mentioned before after thermal testing under pressure at high temperature in glycerol. We trimmed one side of the plate as shown. The magnified view reveals various layers. Following testing, we observe minor HDPE extrusion on the cut edge as anticipated, however, the intact sides with additional polyester batting prevent HDPE flow from the processed media.

The stability analysis necessitates a consideration of the small driving force for deformation or melt migration in a fully submerged system. This is due to the density of glycerin, which is 1.2 g/cc at 125°C, while the density of molten HDPE is 0.76 g/cc and the average density of the composite in its molten state is 0.835 g/cc. Consequently, both the HDPE and composite media are buoyant in glycerol under operating conditions. To counteract this buoyant force, hardware cloth is strategically placed between the composite layers. The metallic separation provides weight that counteracts buoyancy. It adds an additional weight to the system, amounting to a total of 64.44 kg of mesh across 18 layers. Therefore, the combined weight, including mesh, amounts to 246.44 kg. Consequently, the

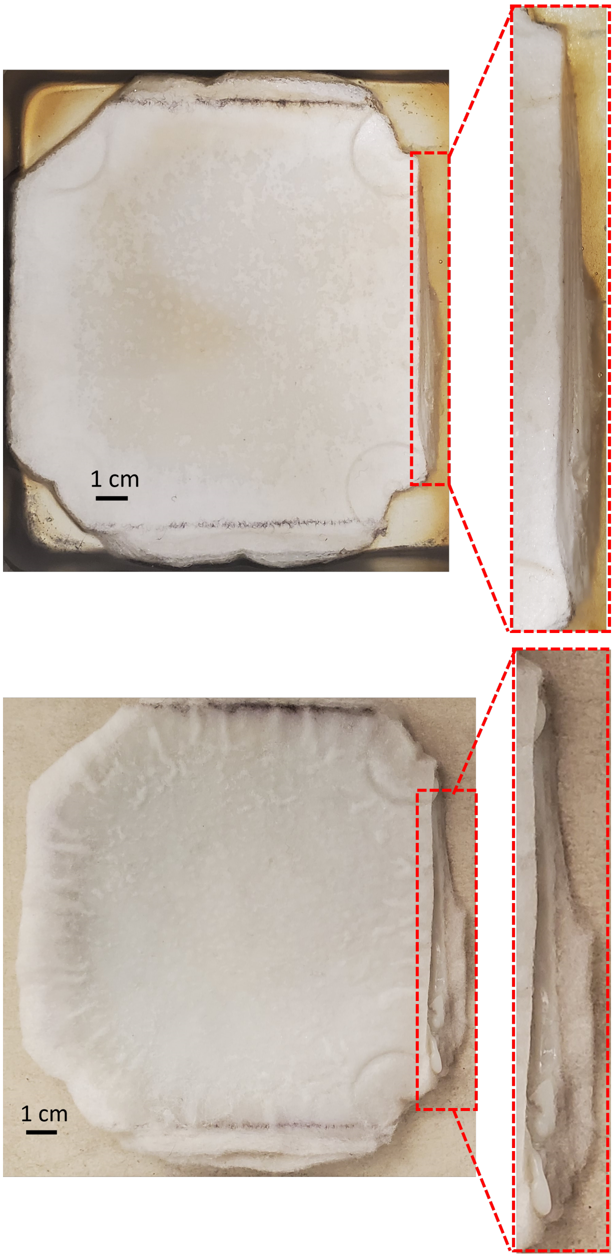

Figure 3.10: Prototype composite media designed to minimize excess melt flow, consisting of low melt flow index HDPE and polyester batting. (Top) The composite immersed in glycerol pre-testing, showcasing a trimmed edge that reveals various layers of material composition and integration. This arrangement allows for testing potential HDPE extrusion under representative pressure (0.67 kPa). (Bottom) Post-thermal testing, subjected to approximately 600 Pa pressure and 150°C for 24 hours. Minor HDPE extrusion is observed on the cut edge, with intact sides effectively containing the HDPE within the composite structure.

stress on the bottommost layer due to this weight is approximately 1.939 kPa. This mitigates the stress on the composite media at the top of the bed to a mere 6.1% of what would be experienced at the bottom of a similar glycerol-free bed. Further, we calculated the net pressure considering the cumulative net buoyant forces from successive bottom layers. Each layer contributes a net buoyant force of approximately 8.24 N. This force incorporates the downward-acting weight of the plate and wire mesh and the upward-acting buoyancy on the fully submerged composite plate. As we have 18 layers in total, this buoyant force accumulates upwards, resulting in a total net buoyant force of 148.3 N acting on the topmost layer. The net pressure exerted on the topmost plate in the bed was computed to be 0.119 kPa.

The preliminary assessment of the composite's stability, as illustrated in Figure 3.11a, offers promising indications of its operational robustness, although further long-term testing is needed to fully validate its performance over numerous charge-discharge cycle, as would be required in real-world applications. After about 36 hours in the molten state, the media (full-scale) shows no apparent signs of melt migration or consolidation. As indicated in Figure 3.11.b, there is some superficial imprinting of the wiremesh on the composite, but this does not compromise the surface or lead to any HDPE leakage. The polyester batting on the external surfaces form an additional barrier against any HDPE leakage beyond the fibrous reinforcement. The polyester, possessing a significantly higher melting temperature than the maximum operational temperature, shows no adhesion to other composite plates or separating mesh. No flow is observed from the edges of the plates, and the additional polyester batting at the edges shows no signs of HDPE intrusion.

Assessing the media stability over long durations (e.g. years) and numerous thermal cycles is a critical requirement, however, a direct measurement is impractical in the experimental time available. To circumvent this restriction, we have adopted a predictive approach rooted in the principle of equilibrium. At this equilibrium state, the polyester batting retains the molten HDPE effectively, exhibiting no net driving force for the migration or leakage of the HDPE from the media. This phenomenon serves as a reliable indicator that the system is stable and will likely remain so over extended periods. This method, thus, allows us to ascertain the likelihood of leakage over extended periods. By employing this predictive approach, we gain an understanding of the system's long-term stability without resorting to extremely long duration testing.

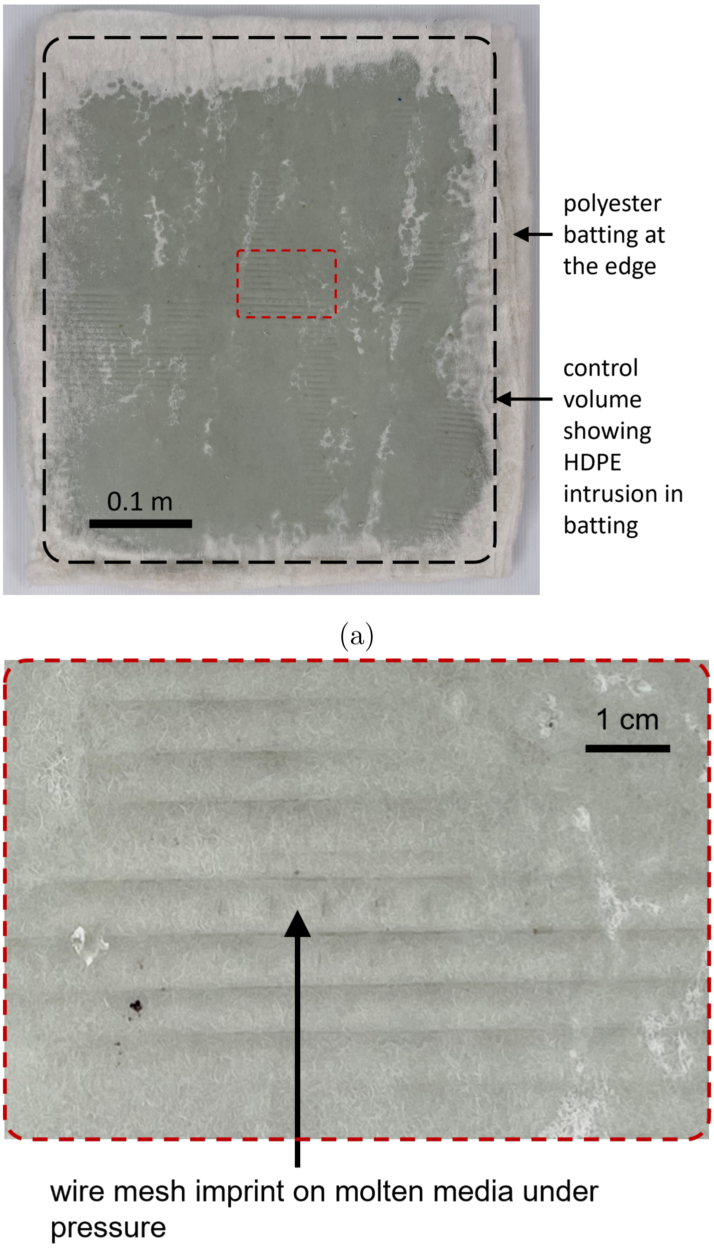

(a)

(b)

Figure 3.11: Evaluation of composite media stability across numerous operational cycles in a thermal energy storage system. (a) Composite integrity post exposure to temperatures exceeding 100°C for 50+ hours, demonstrating robustness with no apparent signs of melt migration or consolidation. (b) Surface imprinting of the wiremesh on the composite does not compromise the surface or lead to HDPE leakage. The external polyester batting forms an additional barrier against leakage, absorbs molten HDPE, and mitigates edge flow, reinforcing the composite's operational reliability.

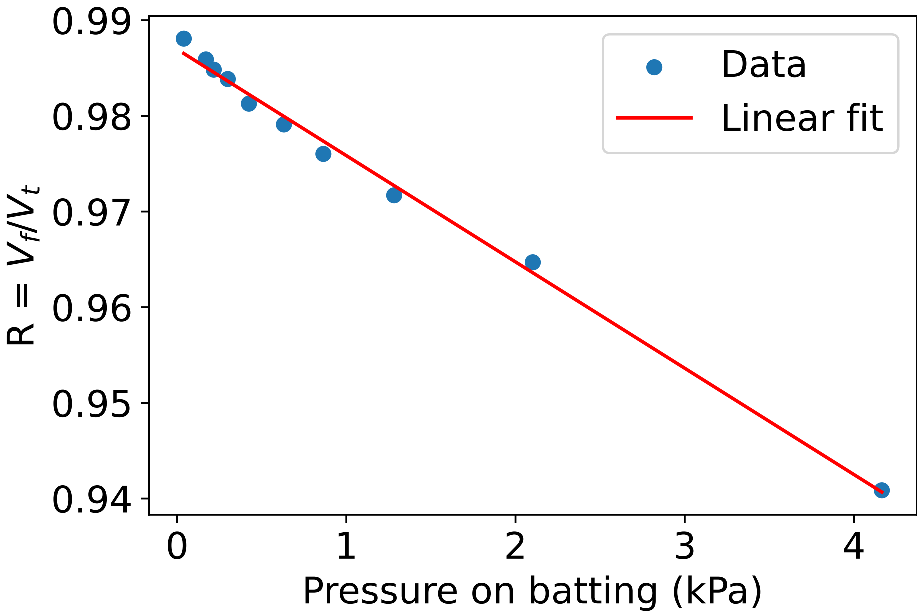

Figure 3.12: Relationship between applied external compressive stress and fraction of fluid volume retained in the saturated batting. Individual data points are measured retained volume ratio at different levels of applied external compressive stress.

As described in Section 3.2.4, we use low viscosity paraffin oil as an analog to molten HDPE to allow for testing the stable saturation of the batting with quick attainment of equilibrium. Paraffin oil and HDPE, both composed of long alkane chains, exhibit closely related chemical structures (CH3-(CH2)n-CH3). The primary difference lies in the length of these chains, with paraffin oil possessing shorter chains than HDPE. Both are non-polar in nature and have similar surface free energies: HDPE at 25.5 mJ/m2 [133], paraffin (solid) at 25.09 mJ/m2, and PETE at 42.35 mJ/m2 [134]. As the equilibrium disposition of liquid in the batting depends only on surface energy and density paraffin oil is an effective simulant for molten HDPE.

Figure 3.12 provides a plot of the volume ratio, R, defined as the fraction of total batting volume occupied by liquid, against the external compressive stress, p (expressed in kPa). The data display a clear downward trend in the volume ratio with the increase in applied compressive stress. A linear fit (Eq. 3.7) gives us a model to predict the relationship between external compressive stress and liquid retention in the batting:

$$R = -0.011p + 0.987 \tag{3.7}$$

where R is dimensionless and p has dimensions of kPa. The constant

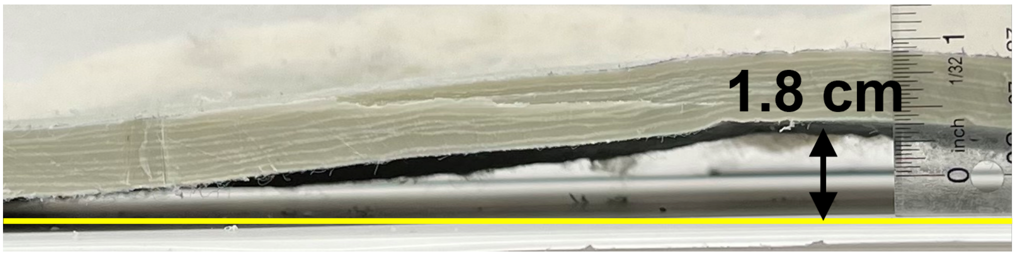

Figure 3.13: Maximum deformation of a composite plate. The figure depicts a full plate, split into two halves, with the most pronounced deformation occurring near the center of the plate.

-0.011 has dimensions of kPa^{-1}. Given an external compressive stress of 0.119 kPa acting on the top plates, we find that the corresponding volume ratio is 0.986 according to our established model. For the current composite plate comprised of 20% polyester by weight, we calculate that the volume ratio of HDPE in the composite at the melt temperature is 0.88. Based on the linear fit, this value translates to the composite being able to withstand an external compressive stress of approximately 9.624 kPa before any significant melt HDPE leakage would occur. It is important to note that this threshold is significantly higher than the maximum compressive stress in our system (0.119 kPa). Therefore, we expect no substantial melt flow from the polyester reinforcement regardless of operational duration.

While PET is more polar than HDPE, its polarity is relatively moderate, especially when compared to materials with high surface energy such as glass fibers [135]. Glass fibers are highly polar and susceptible to wetting by polar substances like glycerin. In our previous work, we applied a non-polar coating to glass fibers to avoid glycerin intrusion and potential swelling of the media [132]. In contrast, PET, though more polar than HDPE, does not exhibit strong wetting behavior towards polar compounds such as glycerin. This suggests a reduced likelihood of glycerin intrusion. However, it is important to note that PET possesses a higher surface energy compared to HDPE, which could raise questions about the potential for glycerin intrusion over extended periods. This topic remains an open question and falls beyond the scope of the current thesis, necessitating further investigation through long-term testing.

PLATE DEFORMATION

In the previous section we examined the stability of the media in terms of its leakage. Another crucial aspect is the structural integrity of the plates under prolonged operating conditions. The geometry of the thermal bed is crucial for ensuring efficient heat transfer and fluid flow. Any significant deformation in the composite plates could disturb their arrangement, potentially choking the flow of the heat transfer fluid and leading to reduced system performance. Therefore, understanding how these plates deform, especially under the cyclical thermal stresses experienced in charge-discharge phase is important. As illustrated in Figure 3.13, the most severe deformation of a composite plate typically manifests near the plate's center. This observation is particularly pertinent during the discharge phase when the material undergoes cooling, thus being exposed to a temperature gradient along its thickness. While this deformation is considerable, it is important to note that it is not expected to progressively worsen over time. During each subsequent charging cycle, the composite material melts, becoming malleable enough to revert close to its initial state, a flat plate. Consequently, this deformability does not significantly disrupt the bed geometry or arrangement, maintaining system efficiency.

3.3.2 System Thermal Performance

This section considers the overall performance of the TES system, with focus on stored energy density and discharge power. The system is characterized by conducting bulk calorimetry tests on packed beds filled with 182 kg of stabilized media.

While the DSC traces can provide data such as the latent heat of melting and the melting and recrystallization temperatures of pristine HDPE, conducting bulk experiments brings several key advantages. Firstly, these experiments account for the comprehensive composite composition, including the polyester fibers and HDPE consolidated in layers. Even a small sample (approximately 10 mg) of the final composite is susceptible to compositional variations due to the heterogeneous mix of the components, making bulk scale experiments essential. Secondly, the heating and cooling rate in DSC is considerably quicker than that employed during the full system's cycling, which is dictated by experimental constraints. This difference in rates can significantly influence the melting/recrystallization hysteresis and perhaps even the total heat capacity. Lastly, bulk experiments permit the characterization of the heat transfer performance of the entire system, encompassing fluid/media interactions.

Figure 3.14 captures the discharge process, where the y-axis shows the temperature difference between the bed's inlet and outlet during discharging, while time is denoted on the x-axis. The glycerol mass flux remains constant at 146 g/m^2/s throughout the operational cycle. The area used for the mass flux calculation is given by the nominal dimensions of the tank provided by the manufacturer, which is 1.3 m^2. Thus, the total mass flow rate is 190 g/s, and it would take approximately 15 minutes to drain all the glycerol from the tank under the operating conditions.

At the beginning of the discharging, the initial temperature of the bed was 143°C. As the discharge process commences, the bed outlet temperature rapidly decreases until the solidification exotherm sets in, indicated by an apparent temperature plateau due to the phase change of the storage media. Following the total solidification of the packed bed, the outlet temperature falls further before aligning closely with the inlet temperature.

Accurate accounting of energy withdrawn from the system requires measurement of the heat lost from the system to ambient. As the charging process approaches completion, typically when the bed is fully charged, we noted a temperature differential ranging between 2°C and 4°C between the charging temperature and the bed outlet temperature. Utilizing equation 3.4, we determine a power loss from the system to the ambient environment, which fluctuates between 0.9 kW and 1.8 kW during this phase. This variation depends on several factors such as the bed temperature and local conditions, including ambient temperature and air movement around the system. For a prudent approach towards our energy and power estimations, we adopt the lower heat loss rate of 0.9 kW (4.9 W/kg). Taking into account a greater parasitic heat loss rate would correspondingly amplify the computed stored energy value. Despite the system being situated outside a temperature-controlled environment, we observe minimal fluctuation in the ambient temperature in the immediate vicinity of the experimental setup during the discharging process. Consequently, we believe that this factor is unlikely to significantly affect the calculation of parasitic heat losses.

Figures 3.15 and 3.16 show energy and power, respectively, extracted during discharging for the discharge shown in Fig. 3.14. These energies primarily consist of the actual latent heat of melting/solidification of the phase change material, the sensible heat of the phase change material, sensible heat of the heat transfer fluid, and some sensible heat of the internal supporting materials placed in the bed.

In this system, the primary energy storage mechanism relies on latent heat, released over a specific temperature range during solidification. For clarity,

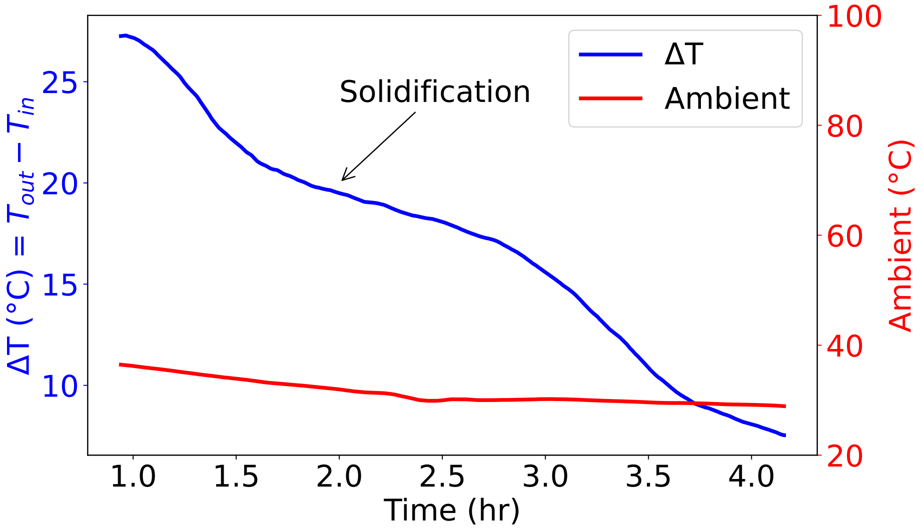

Figure 3.14: Example discharge process in the thermal energy storage system. The graph depicts the temperature difference between the bed's inlet and outlet over time, with a constant glycerol mass flux of 146 g/m^2/s. A distinct temperature plateau during discharging marks the phase change of the storage media. The small fluctuation in the ambient temperature suggests a minimal impact on the computation of parasitic heat losses.

we define 'nominal latent heat' as the heat energy harvested between 130 °C and 120 °C, given the non-isothermal exotherm exhibited during the discharge process. It emphasizes the sudden surge or increase in heat energy that's harvested in this temperature range. Alongside latent heat, there's a significant amount of sensible heat stored within the system, available over a wider temperature range. Therefore, 'total heat' refers to the energy extracted during discharge, starting from the initial bed temperature to the minimum operational or discharge temperature. In this context, we explore the influence of the minimum discharge temperature (that is, the lowest allowable temperature of the heat delivered by the system) on the system's energy capacity and the corresponding energy delivery rate. For the remainder of the chapter this minimum discharge temperature is consistently set at 120 °C.

Figure 3.15(a) illustrates the cumulative energy extracted from the media during discharge, plotted against the time elapsed since the start of the retrieval (as calculated using eq. 3.2, where t_1 corresponds to the start of the discharge and the time indicated in the figure equals $t_2 - t_1$). In Figure 3.15(b), the cumulative extracted energy is depicted against the retrieval temperature, with the temperature difference on the x-axis indicating the decrease in the fluid

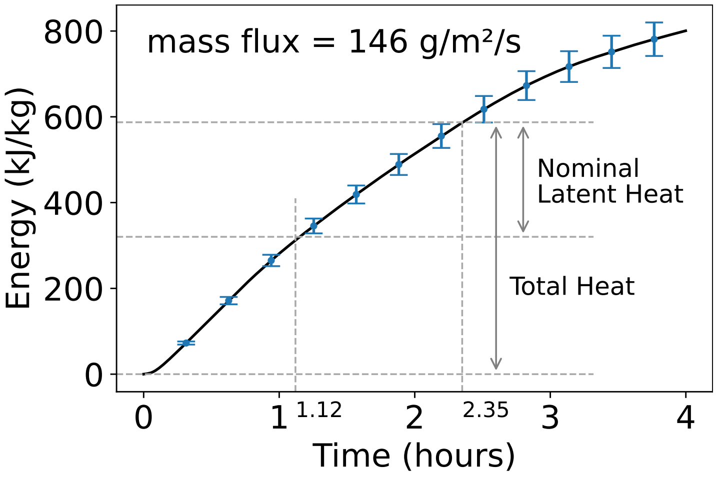

(a)

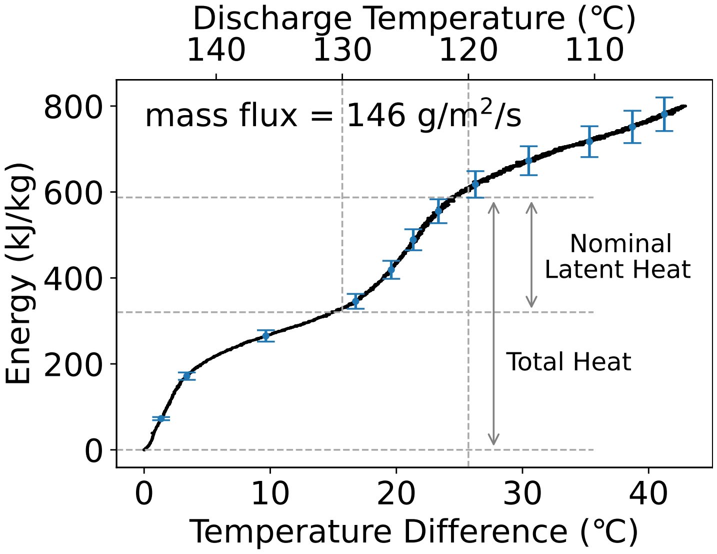

(b)

Figure 3.15: Cumulative energy extraction from the media during the discharge process shown in Figure 3.14. (a) Graph illustrates the time-dependent cumulative energy extraction since the start of retrieval, highlighting distinct phases of energy discharge: the rapid initial discharge due to hot fluid drainage and subsequent decrease in temperature difference, the consistent energy discharge rate corresponding to the release of latent heat, and the eventual deceleration marking completion of solidification. (b) Extracted energy is plotted against retrieval temperature, revealing the nuanced temperature change during the release of latent heat and the system's discharge efficiency. It is noted that approximately 79% of the maximum energy can be retrieved in about 67% of the full discharge time.

outlet temperature since the beginning of discharge.

At the outset, the energy is rapidly discharged as a result of the draining of hot fluid from the containment vessel combined with the low inlet fluid temperature at the start of the discharge phase. Following this initial surge, the pace of energy discharge tapers off due to the decreasing temperature difference between the inlet fluid and the media, until a fairly consistent rate is attained (from 1.12 to 2.35 hours after the start of the discharge process). This phase primarily corresponds to the release of latent heat. The subtle temperature change during the release of latent heat is distinctly visible. After 2.35 hours, the energy release rate decelerates even more, marking the completion of solidification and the system's gradual cooling towards equilibrium with the inlet fluid. The energy extracted from the beginning of discharging to a 25 °C drop (to 120 °C) totals 587 kJ / kg, achieved in approximately 2.35 hours. The maximum energy, 747 kJ/kg, can be retrieved with a 40 °C temperature drop, requiring a total discharge time of 3.61 hours. Thus, in this particular instance, approximately 79% of the maximum energy is retrievable in nearly 67% of the full discharge time. Comparatively, the energy discharged within the nominal latent energy temperature range is about 267 kJ/kg, requiring roughly 1.13 hours.

Figure 3.16 (a) shows the power derived from the media during discharge, as a function of the time elapsed from the beginning of the discharge process, calculated using equation 3.3. In Figure 3.16(b), the extracted power is plotted against the retrieval temperature. The x-axis represents the decrease in the fluid outlet temperature since the start of discharge. At the start of discharge, a swift extraction of energy results in an initial spike in power, peaking at 76.1 W/kg within 0.86 hours. Following this surge, the rate of energy discharge gradually decreases as the energy slope tapers off slightly.

For a comprehensive assessment of the system's performance under different operational conditions, it would be beneficial to investigate the impact of variables such as the fluid inlet temperature, initial bed temperature, and mass flux of the heat transfer fluid on the charging and discharging behaviors of the bed. Ideally, each parameter would be altered independently and metrics such as thermal capacity, charge/discharge rate, and charge/discharge temperature difference would be analyzed in relation to these variables. The current focus, however, is on understanding the behavior of the media after a single melt/freeze cycle and examining the media's response after prolonged immersion in hot glycerol. In-depth characterization of the system is considered for future studies.

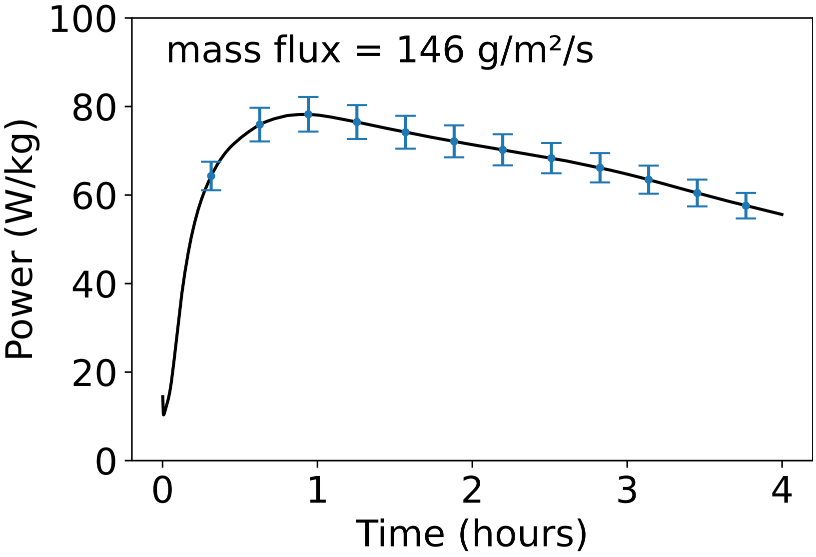

(a)

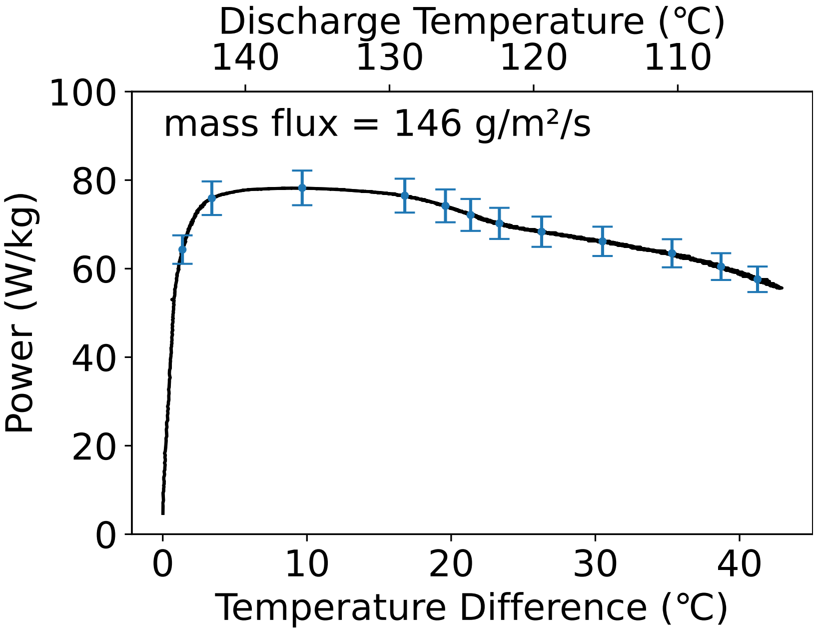

(b)

Figure 3.16: Evaluation of power extraction from the media during discharge process shown in Figure 3.14. (a) The power extraction plotted against time elapsed from the beginning of the discharge process, indicating an initial surge in power peaking at 76.1 W/kg within the first 0.86 hours. (b) The extracted power depicted against the retrieval temperature.

PREDICTIVE MODELING OF PLATE MELTING

Here we present a predictive model of melting behavior for the composite PCM. It allows us to understand and quantify the effect of slab thickness on the total melting time, an essential factor for the charging and discharging rates in TES systems. By using this model, we can optimize the thickness of composite plates to ensure efficient operation while keeping the manufacturing process straightforward and cost-effective. Furthermore, the predictive model can also serve as a tool for evaluating other PCM composites proposed in the literature, allowing meaningful comparisons between different composites.

Proceeding with this modeling, we represent the composite plate as a rectangular slab with semi-thickness L. To simplify calculations, we consider the plate to be thin, meaning the thickness-to-span-length ratio is less than 1/40. The variable x represents the semi-thickness of the slab such that $0 \leq x \leq L$.

Starting at time $t = 0$, we assume that the composite plate is completely solid and at its fusion temperature, T_f. We apply a time-dependent temperature $T_0(t)$ to the surface at $x = 0$, such that $T_0(t) > T_f$. During the charging phase (i.e. melting phase), $T_0(t)$ can be treated as bed inlet temperature. As a result, a melt front forms at $x = 0$ and advances towards the plane at $x = L$. We use $s(t)$ to denote the location of the interface at time t.

Assuming constant thermophysical properties, we can express the partial differential equation (Eq. 3.8) that governs the temperature distribution $T(x,t)$ in the liquid phase, along with its corresponding boundary conditions (Eq. 3.9), as follows [136]:

$$\frac{\partial^2 T}{\partial x^2} = \frac{1}{\alpha}\frac{\partial T}{\partial t}, \quad 0 < x < s(t) \tag{3.8}$$

$$T(0,t) = T_0(t) \quad \text{and} \quad T(s,t) = T_f \tag{3.9}$$

$$k\left(\frac{\partial T}{\partial x}\right)_{x=s} + \rho H_{sl}\frac{ds}{dt} = 0 \tag{3.10}$$

Eq. 3.10 shows the Stefan condition that governs the behavior of the melt interface, with the initial condition that $s(0) = 0$. In Eqs. 3.8 - 3.10, k, α, and ρ represent the thermal conductivity, thermal diffusivity, and density of the liquid phase, respectively. By using a quasi-steady approximation, we can obtain an expression for the location of the interface $s(t)$. The core assumption is that the effects of sensible heat are negligible compared to those of latent heat. As a result of this simplification, the heat conduction equation in the phase where heat transfer is taking place becomes independent of time, although the position of the phase-change front can still vary with time. Specifically, the quasi-steady solution for $s(t)$ is given by Eq. 3.11. In the special case where $T_0(t) = T_0$ is a constant value, we can use Eq. 3.11 to derive the total melting time $t = t_{\text{melt}}$ of the slab. The equation for melting time with constant surface temperature is given by Eq. 3.12.

$$s(t) = \left\{ 2\frac{k}{\rho H_{sl}} \int_0^t \left[T_0(t') - T_f\right] dt' \right\}^{0.5} . \tag{3.11}$$

$$t_{\text{melt}} = \frac{L^2 \rho H_{sl}}{2k\left(T_0 - T_f\right)} \tag{3.12}$$

The total melting time, t_{melt}, as defined by Eq. 3.12, is influenced by several crucial parameters. The melting time exhibits a quadratic relationship with the semi-thickness of the slab, signifying that even a minor increase in thickness can substantially prolong the melting time. This underscores the strategic importance of maintaining thin composite plates in an operating design to enhance the charging/discharging rates of the TES system. Thermal conductivity of the composite also plays a pivotal role, with the melting time inversely proportional to it. Higher thermal conductivity ensures more efficient heat transfer within the material, facilitating faster melting. However, given the practical constraints of manufacturing and cost-effectiveness, our approach primarily focuses on optimizing the thickness of the composite plates instead of enhancing its thermal conductivity. Another influential factor is the temperature difference between the heating medium and the composite's fusion temperature, which acts as the driving force for heat transfer. While a larger temperature difference can expedite melting, it also adversely affects the overall exergetic efficiency of the system. Therefore, achieving a balance between the system's kinetic performance and exergetic efficiency is crucial.

Figure 3.17 illustrates the relationship between the thickness of a slab and the total time required to melt it completely, as predicted by Eq. 3.12. The parameters used in the calculation are a composite thermal conductivity of 0.5 and 1.31 W/m/K, a density of 0.835 g/cc, and a latent heat of melting of 192 J/g for the material. The heat transfer occurs through direct contact with a fluid that is maintained at a temperature 5°C higher than the fusion temperature of HDPE.

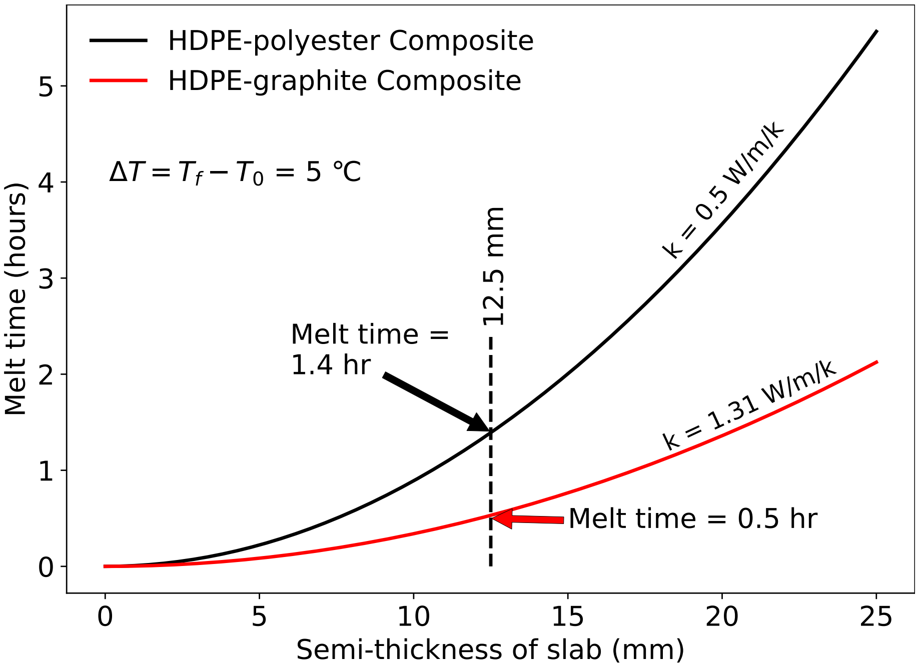

Figure 3.17: Relationship between the thickness of a slab and the total time it takes to melt completely, based on a composite thermal conductivity of 0.5 W/m/K and 1.31 W/m/K, a density of 0.835 g/cc, and a latent heat of melting of 192 J/g. The heat transfer is assumed to occur via direct contact with a fluid that is 1 °C higher than the fusion temperature of HDPE.

3.3.3 Comparison with Existing HDPE Latent Heat Storage Systems

Comparison between current and previous work is essential to evaluate the feasibility and cost-effectiveness of thermal energy storage applications. It determines the benefits and limitations of different approaches and identifies potential areas for improvement. This is particularly important when it comes to developing composite PCM, as several factors, such as material formulation, manufacturing process, and thermophysical properties, must be carefully considered. In this context, this section compares various studies on composite PCM highlighting the strengths and limitations of each approach.

Yang *et al.* [137] formulated and characterized a mixture of recycled high-density polyethylene and graphite for use in medium temperature thermal energy storage applications. The preparation process involved grinding the HDPE pellets to a particle size below 1 mm using a rotor mill, followed by the addition of graphite and mixing until a homogeneous mixture was obtained. The mixture was then placed in molds and heated to a temperature above the melting point for 30 minutes before being hot pressed to remove trapped air within the structure. The resulting composites were cooled and examined. The authors aimed to investigate the properties of the HDPE/graphite composite. Their findings indicate that a graphite content of 20 wt% led to an increase in the thermal conductivity of the phase change material from 0.5 to 1.31 W/mK, i.e. about 160%. Based on the analysis of Section 3.3.2, enhancing the thermal conductivity to this degree reduces the total melt time by 64% (e.g. to 0.5 hours for a plate of thickness 1.25 cm, similar to our current HDPE composite plate and a surrounding fluid temperature 5°C higher than the fusion temperature of HDPE.) While enhancing thermal conductivity is beneficial for faster charge-discharge rates, a more effective approach might be to reduce the material's thickness to improve thermal transport. However, preparing the composite described in [137] involves considerable additional processing and materials. Moreover, while their study does show notable improvements in thermal conductivity, it does not address the long-term shape and structural stability of the composite, which is crucial for sustained application.

In another study, Sciacovelli *et al.* [138] presented a novel method for the manufacture of composite PCMs intended for use in thermal energy storage applications. Using a continuous extrusion process, the authors demonstrated the feasibility of producing composite PCMs comprised of HDPE and graphite. By examining the relationship between material formulation, manufacturing process, and thermophysical properties of the composite PCM products, they provided valuable insights into the use of this method for large-scale production. The study highlights the importance of properly dispersing graphite particles throughout the HDPE matrix, which is achieved through careful mixing of HDPE pellets and graphite powder prior to extrusion. Moreover, the authors demonstrated that single-screw extrusion can produce composite PCM rods with a large length-to-diameter ratio, enabling high-throughput production suitable for bulk manufacturing. The use of a single-screw extruder in the manufacturing process allows for a continuous process with higher throughput compared to the batch-based approach demonstrated in the current work. However, the currently considered composite is also amenable to continuous processing, as described in Section 3.3.3.

Zauner *et al.* [57], [58] built and investigated a storage system using an insulated steel container with a fin-tube heat exchanger and HDPE as phase change material. The study identifies some potential challenges with this approach. The high viscosity of the HDPE polymer and small fin spacing made it difficult to remove all air from the PCM, which could affect its effectiveness as a phase-change material. Additionally, the deformation of the fins during melting and crystallization could increase maintenance costs and potentially affect the performance of the heat exchanger.The material and manufacturing costs of the fin and tube setup may also add substantially to the capital cost of the storage system. Overall, these factors should be carefully considered when evaluating the feasibility and cost-effectiveness of using this technology for thermal energy storage applications.

Abe *et al.* [56] and Kanimoto *et al.* [55] utilized a copolymer with shape stability, allowing direct contact heat exchange in their experiment. However, due to the need to prevent rod bending at high temperatures, specialized aluminum honeycomb structures were required to support the rods. This additional requirement for external support may significantly increase the overall cost of the system.

Salyer and Davison's descrive a method of cross-linking that provides enough shape stability to enable packed bed operation without the need for extra support [59]. The electron beam processing method used in their approach requires specialized manufacturing capabilities, however.

We previously [132] presented a novel shape-stable HDPE composite latent heat storage media. To achieve the required stability, we reinforced HDPE with treated glass fibers that acted as an inert filler, and partially coated the PCM elements with a rigid thermoset polymer. The treated glass fibers were uniformly mixed with molten virgin HDPE using a custom-made high shear mixer. Although this formulation worked well for small-scale production, it provides some challenges for scale up, due to the length and rigidity of the fibers required.

MANUFACTURING SCALABILITY

Scaling up the manufacturing process for the composite storage media to commercial levels presents unique challenges and considerations, particularly due to the poor thermal diffusivity of the materials applied. For our current setup, which employs a batch-based heated press approach, a direct scale-up might be infeasible due to throughput limitations. However, a transition to a continuous production method, such as a roll-to-roll calendering process, might offer a promising solution. The roll-to-roll process operates similarly to our heated press method, but instead of utilizing large heated platens, it employs heated rotating cylinders or rollers. These rollers apply the necessary heat and pressure to melt and consolidate the materials, but they do so in a continuous and streamlined manner. This process layout can address the constraints we've experienced with our heated press method while still preserving its benefits.

In the calendering process the thickness of the produced plates can be controlled by adjusting the gap between the rollers. This enables the production of composites of varying thicknesses, tailoring to different application needs. Second, the dwell time, which is crucial for ensuring complete melting and consolidation of our specific materials, can be controlled by modifying the angular velocity of the rollers. The continuous nature of the roll-to-roll calendering process also promises improvements in consistency, which is crucial for large-scale commercial production. It allows for a constant production flow that eliminates the down time for changeover and energy lost to cooling and heating inherent in batch processes, thus enhancing production efficiency. Economically, a continuous production method like roll-to-roll calendering can be more cost-effective at a larger scale. It reduces energy and time waste associated with batch processes.

We have designed a prototype roll-to-roll calendering process. This process, shown in Figure 3.18, entails a series of coordinated steps to produce the composite plates. The process begins with stacking alternating layers of polyester fibers and HDPE pellets. To facilitate the melting and consolidation of

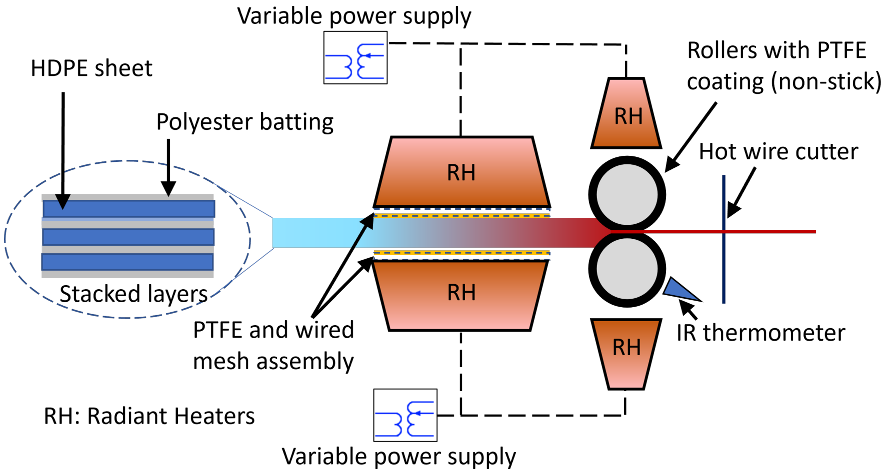

Figure 3.18: Schematic of continuous composite sheet forming for bulk-scale media production. The process begins with the stacking and preheating of alternating layers of polyester fibers and HDPE, followed by feeding the layers into a set of heated rollers maintained at temperatures optimal for HDPE melting but below polyester's melting point. The hot rollers, covered with PTFE sheets to prevent HDPE sticking, produce a consolidated composite, subsequently shaped using hot wire cutters.

these layers, they are preheated using infrared heaters before they are introduced to the calendaring stage. This preheating step is crucial to ensure a uniform heat distribution across the material layers, thereby reducing the likelihood of incomplete melting. The preheated layers are then fed into a set of heated rollers. These rollers are maintained at a temperature above the melting point of HDPE (130°C), but below that of polyester (260°C), to ensure selective melting of the HDPE pellets. To prevent the sticking of the molten HDPE to the rollers, they are coated with thin PTFE sheets, which act as a non-stick barrier between the rollers and the material. Upon passing through the rollers, the now consolidated composite material is sectioned into the desired shapes using hot wire cutters. This provides flexibility in shaping the product, making it adaptable for various applications.

3.4 Conclusion

This study investigated a composite consisting of HDPE and polyester fibers in batting form for potential use as a PCM in TES systems. The composite was synthesized, and its mechanical stability and heat capacity were assessed.

Manufacturing complexity associated with previous designs, such as using silane treated glass fibers with HDPE and the requirement for mixing them using a high shear mixer, is reduced. The new media has improved manufacturability and also lower cost of components. The composite showed compatibility with heat transfer fluids like glycerol. Operational tests in a submerged packed bed TES system revealed minimal deformation and absence of melt migration, indicating potential for long-term stability.

The TES system was designed to include the composite PCM in a packed bed in direct contact with the heat transfer fluid. The system demonstrated increased heat transfer performance and energy density. These characteristics are attributed to the composite's shape stability and small feature size (thickness), as well as its role in facilitating energy storage with a minimal temperature difference between the charging and discharging phases.

Tests for long-term stability indicated that the composite could withstand external compressive stresses greater than those typically encountered in standard operational conditions. Leakage of HDPE from the composite under these conditions is considered unlikely based on test results.

While the study provides initial insights, further research is required to investigate the influence of variables such as fluid inlet temperature, initial bed temperature, and heat transfer fluid mass flux on the charging and discharging behaviors of the system. These future investigations could contribute to a more comprehensive understanding of system performance.

Chapter 4

Rapid Steam Production and Performance Enhancement of a Steam Accumulator Using Packed-Bed Latent Heat Thermal Energy Storage Technology

4.1 Introduction

Steam remains an integral component in various industries, significantly contributing to modern energy consumption. By 2021, natural gas, which represented about 38% of the US energy production, and coal, which contributes around 22%, were predominantly used to generate steam. Even petroleum, though representing less than 1% of total production, was used in the form of residual fuel oil and petroleum coke for steam generation [139]. Steam remains relevant in modern times due to its unique features, which are irreplaceable by other systems. It is essential for various industrial processes such as heating, sterilization, cooking, and energy generation in industries like hospitals, food processing, electricity generation, paper production, petroleum refining, and chemical processing [140]. Its efficiency, safety, versatility, and adaptability ensure its continued importance and make it an indispensable element in these essential businesses.

Boilers are the main source of steam production, providing a reliable and efficient method for generating steam. However, the steam intermittency problem can pose challenges in maintaining consistent steam supply. Intermittency can cause instability in the steam system, leading to fluctuations in pressure, temperature, and flow rate. This can have negative consequences for processes that rely on a stable supply of steam, such as power generation and industrial applications. Despite this, steam remains crucial for many industries and processes.

Addressing the intermittency of steam generation requires a combination of strategies, including load management, advanced control systems, storage, and proper maintenance. Steam accumulators are devices designed to store excess steam during periods of low demand and release it when demand increases, helping to manage intermittency in steam generation systems. They serve as a buffer between the boiler and the steam-consuming processes, improving the system's overall stability, efficiency, and reliability.

Benefits of steam accumulators include improved boiler efficiency, faster response to load changes, reduced boiler size, and enhanced process stability. By maintaining a consistent steam supply, accumulators can ensure optimal performance and product quality across various applications, making them a valuable solution for addressing the challenges of steam intermittency.

Frequently, steam is required at high instantaneous flow-rate for short duration of time. A few applications with such requirements are in hospital and industrial sterilization, steam peeling, plastic molding, rubber processing, and hosiery finishing [141]. In such applications, a steam accumulator which can store and provide clean dry steam instantaneously at high temperature and pressure, to meet peak demand, is commonly used.

There are two types of steam accumulator based on operational mode: the pressure-drop accumulator and the constant pressure accumulator. The case study and model development introduced here is a combination of the two types and take advantage of the capabilities of thermal energy storage (TES) materials.

TES can utilize various forms of energy, such as sensible heat, latent heat, or thermochemical energy, sometimes even combining them. Sensible Heat Storage (SHS) stores energy by elevating the temperature of a solid or liquid substance. The storage capability of SHS depends on the specific heat of the material, the range of temperature change, and the volume of the material. Latent Heat Storage (LHS), in contrast, retains energy through phase changes in a material, like transitioning from solid to liquid or from liquid to gas. The effectiveness of an LHS system using Phase Change Material (PCM) relies on the specific properties of the PCM. Thermochemical storage takes a different approach, capturing energy through reversible chemical reactions that break and reform molecular bonds. Among these methods, latent heat storage is particularly notable for its high-energy density and its ability to store thermal energy at a constant temperature, which is determined by the PCM's phase transition temperature.

PCM can experience various types of phase transitions, such as from solid to solid, solid to liquid, solid to gas, and liquid to gas. Each transition type has its own unique features and suitable applications. For example, in solid-to-solid transitions, thermal energy is stored as the material shifts between different crystalline states, usually resulting in smaller changes in latent heat and volume compared to solid-to-liquid transitions. On the other hand, while solid-to-gas and liquid-to-gas transitions offer higher latent heat storage, they are generally not ideal for thermal storage systems due to the significant volume changes they undergo, which present containment challenges. As a result, our focus is on solid-to-liquid transitions. Although these may offer lower latent heat compared to liquid-to-gas transitions, they have the advantage of more manageable volume changes, making them more practical and easier to contain in a storage system.

An ideal PCM should have a suitable phase transition temperature and high latent heat for efficient thermal storage. Additionally, it should offer physical stability through minimal volume changes and low vapor pressure. [5]. Integrating a phase change material into a steam accumulator can elevate the system's performance and efficiency. Given that steam accumulators function as energy reservoirs, incorporating PCMs can increase their energy density and enable heat storage and discharge at an almost constant temperature. This not only stabilizes the device's operation but also permits a more regulated and efficient energy output. Furthermore, the enhanced energy storage could lead to reductions in both the physical dimensions and operating expenses of the device.

Steinmann and Eck [117] have acknowledged the potential of integrating PCM into a steam accumulator for isothermal energy storage, although their focus remained primarily on conventional steam accumulator designs. They proposed the integration of steam storages as buffer storage in solar thermal systems due to their fast reaction time and high discharging rates and discussed three methods for improving the performance of Ruths steam accumulators. The first method is to use an additional sensible heat storage to superheat the discharging steam. The second method is to incorporate encapsulated PCM into the liquid phase of the accumulator to maintain a constant steam pressure during discharging. The third method is to use an external flash evaporator to achieve the same goal. The hybrid storage concept presented by Dusek and Hofmann [142] in their paper involves adding PCM to the outer shell of a Ruths steam accumulator. Their paper presents a dynamic model for this configuration, based on energy and mass balance equations for the liquid water/steam part and the assumption of thermodynamic equilibrium between the two-phase fluid at all time. The model for the PCM layer is similarly founded on an energy balance equation. Building upon this foundational work, Rene *et al.* [143] further investigate the design and economic viability of such hybrid storage systems compared to traditional Ruths Steam Storage. The paper also discusses the economic feasibility of retrofitting existing Ruths steam accumulator with PCM, highlighting that it is most beneficial under certain conditions like long charge/discharge times and smaller storage sizes. Overall, the study offers insights into when a hybrid storage system can be a more cost-effective choice than a traditional steam accumulator. Buschle *et al.* [144] compared two methods for adding PCM to Ruths steam accumulators: internal and external. The external method involves wrapping a tube system in PCM. The internal method involves adding encapsulated PCM directly into these vessels using pressure-resistant tubes. The study compares these two approaches in terms of the thickness of the walls required and the time it takes for the PCM to solidify. Biglia *et al.* [145] focuses on enhancing the efficiency of industrial steam use, particularly in thermal processes like food sterilization. The authors propose a TES system using steam accumulators to better align steam production with demand. They develop a predictive model for a steam plant's performance under different conditions and validate it with a case study in the food industry. The model aims to optimize steam use and reduce costs. Stevanovic *et al.* [146] developed a numerical model to simulate and analyze the operation of steam accumulators, focusing on both liquid water and steam phases. The model is based on mass and energy balance equations and includes non-equilibrium correlations for condensation and evaporation rates. They validated the model with measured data and found that charging the accumulator with superheated steam leads to a steady increase in pressure, suggesting the need for subcooled feedwater injection for steam condensation and pressure reduction. Murakoshi and Fushimi [147], in their study uses dynamic simulations to analyze how steam pressure in a steam accumulator affects the levelized cost of storage and steam discharge time in an existing biomass power plant. The aim is to improve renewable energy storage and cost-efficiency.

This chapter introduces the use of a PCM (HDPE composite) in a packed bed configuration to enhance steam generation capacity, a departure from conventional systems that rely solely on pressure drop. It employs an in-depth thermodynamic analysis, represented by specific equations, to quantify and compare steam generation capacities under different working pressures for both conventional and PCM-enhanced packed bed accumulators. By employing a quasi-steady approximation, the study simplifies the heat conduction equation, focusing primarily on latent heat while treating the effects of sensible heat as negligible. This approach allows for a time-independent analysis of heat transfer in the phase where it occurs, though the phase-change front still vary with time. The study also explores two different operational contexts—constant pressure steam output and constant thermal energy output—and rigorously analyzes each through derived equations and graphical representations.

This chapter is organized as follows: Section 2 reviews the working principles of conventional pressure-drop steam accumulators and identifies gaps that this study aims to address. Section 3 outlines the methodology, which includes the integration of Phase Change Material (PCM) into a pressure-drop steam accumulator. Section 4 examines performance models for a PCM-based steam accumulator in two distinct operational contexts—constant pressure and constant thermal energy output—to understand the system's behavior under various conditions. Results are presented and analyzed in Section 5. The chapter concludes with a summary of the key contributions in Section 6.

4.2 Conventional Steam Accumulator

A steam accumulator is 50% to 85% filled with water depending on the application [143]. During the charging phase of the steam accumulator, the incoming steam is injected below the surface of the water already present in the accumulator using a distribution manifold fitted with steam injectors. The steam rapidly condenses, releasing its latent heat and increasing the pressure and temperature of the accumulator to its desired values [145]. The charging process can proceed in different ways, depending on whether super-heated steam or saturated liquid water is used [148]:

1. When super-heated steam is used for charging, the pressure within the accumulator rises, while the mass of the liquid storage experiences minimal changes.

2. If saturated liquid water is added, the pressure remains largely constant.
3. Indirect charging is another option, where a heat exchanger is integrated into the liquid volume, allowing for the use of a medium other than water and at lower pressure to source heat.

Steam accumulators experience a drop in steam pressure during discharge. When demand exceeds the boiler's capacity, the stored water at saturation temperature enables the generation of flash steam at the required rate, effectively addressing any overload. Conversely, when the demand is less than the boiler's capacity, the accumulator recharges using surplus steam, allowing the boiler to operate at its maximum continuous rating. In sliding pressure systems, discharge occurs in the form of saturated steam [141]. Saturation pressure plays a complex role in steam production rates. Specifically, at higher pressures, there's a reduced change in saturation temperature, leading to smaller alterations in the water's sensible energy. This also results in a decreased density of saturated liquid water, lowering the volumetric energy density. However, the energy required for evaporation is also reduced at these elevated pressures [148].

During both charging and discharging, fluctuations in the water level are natural. Factors affecting these fluctuations and pressure transients include initial and boundary conditions such as the initial mass of the water, steam inflow and outflow rates, and inlet steam temperature and pressure. In designing a steam accumulator, it is standard to calculate its internal volume based on these factors to meet the required steam production or accumulation needs, all while accommodating pressure changes between specified minimum and maximum values [146].

4.3 Packed Bed Steam Accumulator

A steam accumulator is a thermal energy storage device. A means of generating more steam is by adding heat directly into the boiling water. This can be done by, e.g. installing heaters in the accumulator or using a packed bed of thermal energy storage media. The latter could be the polymeric composite described later in this study, which will store the latent heat of fusion and some sensible heat during charging. The steam supplied by the accumulator will be in equilibrium with the water in it. The steam pressure will be equal to the saturation pressure corresponding to water temperature throughout the process. This temperature will depend on the details of the internal energy/temperature relationship for the media and the heat transfer in the media.

4.3.1 Latent Heat Thermal Energy Storage Media

An ideal PCM should posses the following properties [21], [37]: Firstly, the solid-liquid phase transition temperature of the material should align with the operating temperature of the application. The material should also have a high heat of fusion and minimal hysteresis between melting and solidification. High thermal diffusivity is desired for rapid charging and discharging. Compactness is another consideration; the material should have a high density to minimize the size of the storage container. Additionally, the material should exhibit minimal volume changes during phase transitions and have a low vapor pressure at operating temperatures to simplify containment design. Long-term thermal stability is required to withstand multiple charge-discharge cycles. The material should also be chemically stable, non-toxic, non-flammable, and non-explosive for safety reasons. Lastly, cost-effectiveness and large-scale availability are crucial for practical applications.

Reinforced HDPE composites are thermally stable and have a high enthalpy of crystallization. The recrystallization temperature is approximately 127 °C depending on the cooling rate. In a previous study [132], we developed a novel form-stable, solid-liquid PCM composed of fiber-reinforced HDPE composite. To enhance compatibility with HDPE, glass fibers were treated with a silane coupling agent to render their surfaces hydrophobic. These treated fibers were uniformly mixed with molten HDPE using a custom-built high shear mixer. Approximately, 14.5% of the composite was made of glass fibers. The blended material was then shaped into pellets. An epoxy coating was applied to these pellets, acting as a supportive exoskeleton rather than a full encapsulation. The media demonstrates robust thermal performance over 100 melt/freeze cycles, retaining a bulk latent heat of 162 to 172 kJ/kg. Mechanical stability was also commendable; only 1% of tested pellets showed severe leakage, while over 91% exhibited no leakage. Challenges include non-uniform mixing of fiberglass and HDPE, as well as occasional epoxy coating defects leading to encapsulation holes. Minimal pellet adhesion was observed, and when it did occur, it resulted in open porous structures. Therefore, the composite media shows promising prospects for durable thermal energy storage..

In previous chapter, we extended our research to design another PCM tailored for large-scale TES applications. In this design, the composite predominantly consisted of HDPE and bonded polyester (PET) batting. The PET batting makes up 20% of the composite by weight and serves a specific purpose: it acts as a matrix to contain the melted HDPE. Operating much like a sponge, the PET batting utilizes capillary forces to hold the molten HDPE, thereby preventing leakage and enhancing the composite's stability under low external compressive stress. However, additional research is needed to ensure that this composite formulation can sustain pressures up to those experienced in operational steam accumulators.

For applications requiring steam discharge at higher temperatures, the use of HDPE composites is a major disadvantage instead. Therefore, more materials that are compatible with water and have good thermal stability and high enthalpy of crystallization need to be investigated. One potential material includes polypropylene with melting point, 169.5 °C, and high latent heat of fusion (137.9 J/g for 100% crystalline polypropylene) [149].

Besides polypropylene, there are other PCMs that show promise for medium-temperature applications. These materials have appropriate melting temperatures and high latent heat of fusion, making them potential candidates for use in steam accumulators. Some PCMs with melting points below 170 °C are provided as examples in Table 4.1.

Table 4.1: Selected PCMs with Melting Points Below 170 °C

PCM	T_m (°C)	L (J/g)	Ref.
D-Mannitol	151.82	319	[81]
$LiNO_3/KCl$	165.6	272	[83], [150]
$LiNO_3/KNO_3$	135	135.6	[150]
$LiNO_3/NaNO_3/KCl$	160	266	[150]

Inorganic PCMs commonly include eutectic nitrate salt mixtures like $LiNO_3$–KCl, $LiNO_3$–KNO_3, $LiNO_3$–$NaNO_3$–KCl. These materials have demonstrated their efficacy and robustness, particularly because of their high decomposition temperatures[151]. They also offer high latent heat of melting and are compatible with standard container materials like stainless steel within operational temperature ranges[152]. However, these salts present challenges as they are both hygroscopic and strongly oxidizing [153]. As a result, specialized encapsulation is often required, and they are generally not suitable for direct contact with many types of heat transfer fluids.

Smaller PCM pellet size results in better heat transfer. Because the thermal conductivity of the PCM material is poor, smaller sizes will decrease the thermal resistance as a result of conduction. Therefore each pellet can be charged and discharged rapidly which is essential for the packed bed steam accumulator performance. Also, the addition of thermally conductive fillers in the HDPE matrix will aid in the quick charging and discharging of the material [137].

4.4 Performance Models

The physical model assumes that the pressure vessel is perfectly insulated, eliminating any parasitic heat loss from the fluid to the surrounding environment. Additionally, the fluid is assumed to have a uniform temperature throughout its volume, indicating perfect mixing. Furthermore, the fluid is in thermal equilibrium with the walls of the pressure vessel at all times.

4.4.1 Steam Storage Capacity

In this section, the maximum steam storage capacity of a conventional and a packed bed steam accumulator is studied thermodynamically.

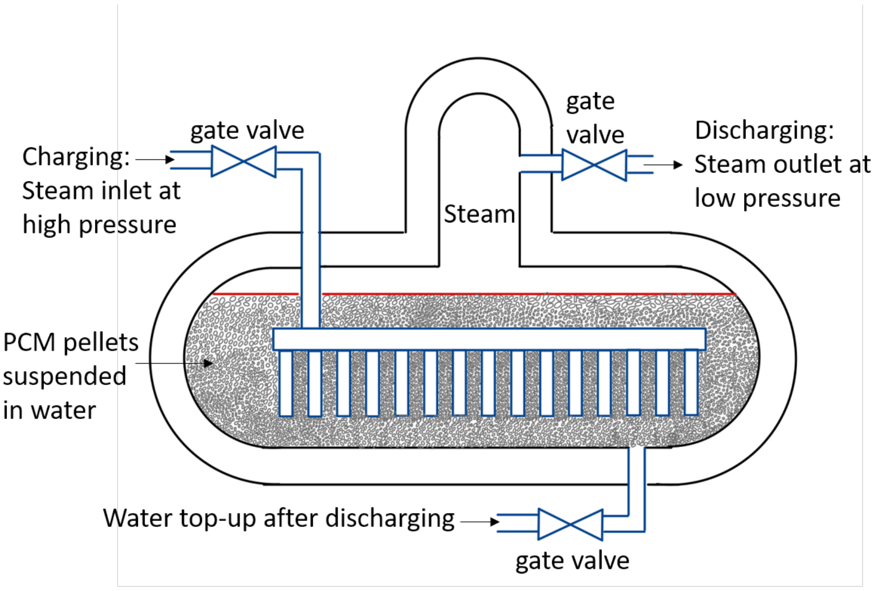

Figure 4.1: Schematic of a steam accumulator with phase change materials (PCM) in water.

Nomenclature:

P_1 = Charging pressure (bar g)

P_2 = Discharging pressure (bar g)

$h_{f|P_1}$ = Specific enthalpy of saturated water at P_1 (kJ/kg)

$h_{f|P_2}$ = Specific enthalpy of saturated water at P_2 (kJ/kg)
$h_{fg|P_2}$ = Latent heat of steam at p_2 (kJ/kg)
$v_{f|P_2}$ = Specific volume of saturated water at P_2 (m^3/kg)
T_1 = Saturation temperature of steam at P_1 (°C)
T_2 = Saturation temperature of steam at P_2 (°C)
c_s = Specific heat of PCM before melting (kJ/kg-°C)
c_L = Specific heat of PCM after melting (kJ/kg-°C)
L = Latent heat of melting of PCM (kJ/kg)
T_m = Melting temperature of PCM (°C)
ρ_{PCM} = density of PCM ($\mathrm{kg/m}^3$)

The specific energy, e, released by the PCM during operation from a higher operating pressure, i.e. the charging pressure, to a lower pressure, i.e. the discharging pressure, can be calculated as shown in Equation 4.1.

$$e = \begin{cases} c_L(T_1 - T_2) & \text{if } T_m < T_2 < T_1 \\ c_L(T_1 - T_m) + L & \text{if } T_m = T_2 < T_1 \\ c_L(T_1 - T_m) + L + c_s(T_m - T_2) & \text{if } T_2 < T_m < T_1 \\ c_s(T_1 - T_2) + L & \text{if } T_2 < T_1 = T_m \\ c_s(T_1 - T_2) & \text{if } T_2 < T_1 < T_m \\ 0 & \text{otherwise} \end{cases} \tag{4.1}$$

The energy extracted from the PCM in a steam accumulator depends on the initial and final temperatures, T_1 and T_2, and their positions on the specific energy-temperature curve. If both temperatures lie either in the "After Melting" or "Before Melting" zones, the energy extraction is purely due to sensible heat and the PCM remains in one phase—either liquid or solid. However, if the temperatures span across the melting point, T_m, the PCM undergoes a phase change and the energy extraction includes both sensible heat changes and latent heat.

The liquid level in the accumulator is assumed to be constant. This is achieved by adding feed-water when the level decreases due to discharging. Alternatively, water is removed when too much steam condenses during charging using a steam trap (ball float type) [141]. It is also assumed that the PCM is completely submerged in the water at all times during this analysis.

For a conventional steam accumulator, the steam storage capacity per

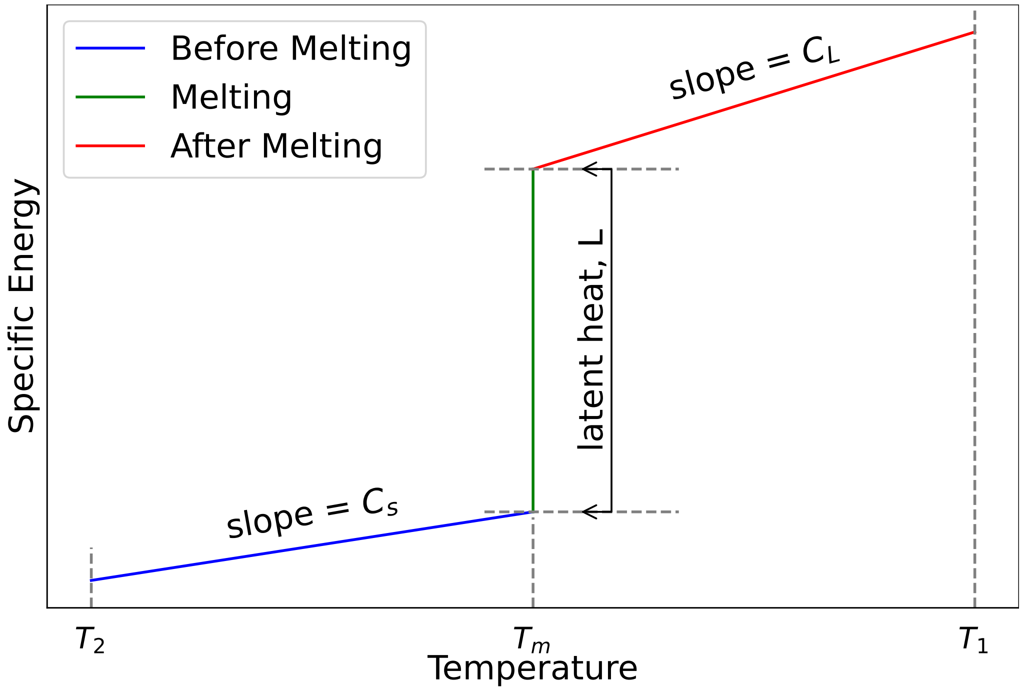

Figure 4.2: Illustration of specific energy as a function of temperature for a PCM. The specific energy varies linearly with temperature both before and after melting, showing a sudden increase at the melting temperature T_m. The calculations for specific energy are based on Equation (4.1).

unit volume of steam accumulator filled with saturated water is given by Equation 4.2 [141].

$$\text{Steam storage capacity}|_{\text{conventional}} = \frac{(h_{f|P_1} - h_{f|P_2})/v_{f|P_1}}{h_{fg|P_2}} \tag{4.2}$$

The term $(h_{f|P_1} - h_{f|P_2})$ represents the energy released as sensible heat when the pressure of saturated water drops from P_1 to P_2. Similarly, $h_{fg|P_2}$ is the latent heat of steam at P_2, representing the energy required to convert unit mass of saturated water into steam at this pressure. Consequently, the ratio $(h_{f|P_1} - h_{f|P_2})/h_{fg|P_2}$ denotes the proportion of flash steam generated (in kg) per kilogram of water.

In a rigid steam accumulator, the internal volume remains constant. Because the mass of water that can be stored in the accumulator varies with pressure, it is normalized by the amount of steam produced per unit volume of the accumulator. The initial state of the water in the accumulator is at pressure P_1; therefore, we use this pressure to consider the mass of water that the accumulator can hold. As a result, Equation 4.2 provides an estimate of the amount of steam produced per unit volume of the accumulator, assuming it is fully filled with water.

The equation for the steam storage capacity in a packed bed with PCM pellets differs from the one for a conventional accumulator by incorporating the additional energy storage contribution from the PCM. For a steam accumulator packed with PCM pellets, the steam storage capacity per unit volume of the accumulator is given by Equation 4.3. In this equation, ϵ accounts for the porosity, indicating how much of the accumulator volume is filled with water. The term $(h_{f|P_1} - h_{f|P_2}) \cdot \epsilon / v_{f|P_1}$ represents the energy released from the water part of the packed bed.

In a packed bed accumulator, additional storage is provided by the PCM pellets, which primarily store energy due to phase change. This contribution is captured by the term $e\rho_{\text{PCM}}$. The term $(1-\epsilon)$ represents the proportion of the packed bed filled with PCM pellets per unit volume of the steam accumulator, and $(1-\epsilon)e\rho_{\text{PCM}}$ quantifies the energy stored in the PCM pellets. Finally, these terms are summed up and divided by $h_{fg|P_2}$ to find the equivalent amount of steam that could be generated per unit volume of the accumulator.

$$\begin{gathered}\text{Steam storage capacity}|_{\text{packed bed}} = \\ \frac{(h_{f|P_1} - h_{f|P_2}) \cdot \epsilon / v_{f|P_1} + (1-\epsilon)e\rho_{pcm}}{h_{fg|P_2}}\end{gathered} \tag{4.3}$$

4.4.2 Kinetic Behavior

In this study, we consider a thin PCM and the heat transfer is primarily dominant along the thickness of the material. This implies that the significant heat transfer occurs predominantly across two opposing surfaces of the slab.

Given the symmetric boundary condition and the rectangular geometry of the slab, we have opted to model only half of the entire geometry. This simplification is acceptable and does not impact the accuracy of our model as the heat transfer behaviour on one side of the slab mirrors that on the other side due to the imposed symmetry.

4.4.3 Solidification of Slab: Constant Temperature Boundary Condition

In this analysis, we focus on the solidification of a slab of the PCM with a constant temperature boundary condition. The solidification process is driven by a temperature differential $\Delta T = T_f - T_0$ between the PCM fusion temperature

(T_f) and the surface temperature (T_0). The temperature differential allows heat to flow from the PCM to the surrounding water, facilitating the generation of steam.

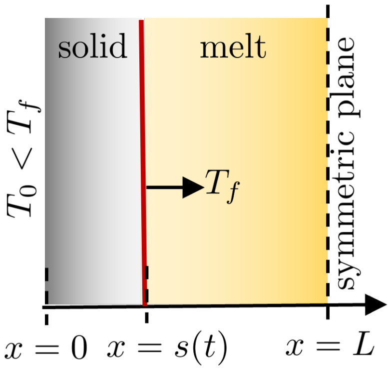

Figure 4.3: Rectangular slab undergoing solidification, with a semi-thickness of L. Boundary conditions are established with a constant surface temperature T_0, less than the fusion temperature T_f, maintained at $x = 0$. A symmetric condition with zero heat flux is applied at $x = L$. The location of the melt interface, denoted as $s(t)$, indicates the progression of the solidification front from left to right in the positive x direction, beginning at $x = 0$ and culminating at the symmetric plane $x = L$.

GOVERNING EQUATIONS

Equation 4.4 is the heat diffusion equation without any heat generation term. It describes how temperature T varies with time t and distance x within the solidifying PCM slab:

$$\frac{\partial^2 T}{\partial x^2} = \frac{1}{\alpha}\frac{\partial T}{\partial t} \quad 0 < x < s(t) \tag{4.4}$$

Let α denote the thermal diffusivity of the material and let $s(t)$ represent the position of the solid-liquid interface at time t. Equation 4.5 signifies the boundary condition and the initial condition, which are respectively the constant surface temperature T_0 and the fusion temperature T_f.

$$T(0,t) = T_0 \text{ and } T(x \geq s(t), t \geq 0) = T_f \tag{4.5}$$

This implies that at any given time t, the temperature at the solid-liquid interface and beyond ($x \geq s(t)$) is maintained at the fusion temperature T_f, while the surface temperature of the slab is kept constant at T_0. The balance of heat flux at the solid-liquid interface is depicted by the Stefan condition, as illustrated by Eq. 4.6 - 4.7 [136].

$$k\left(\frac{\partial T}{\partial x}\right)_{x=s} + \rho h_{sl}\frac{ds}{dt} = 0 \tag{4.6}$$

$$s(0) = 0 \tag{4.7}$$

Here, k represents the thermal conductivity, ρ denotes the density, and h_{sl} is the latent heat of fusion. The solidification of the liquid commences at $x = 0$, and the interface moves in the positive x direction at a velocity represented by ds/dt.

Figure 4.3 illustrates a rectangular slab with a semi-thickness of L. The applied boundary conditions for this configuration are as follows: one side is maintained at a constant surface temperature T_0 at $x = 0$, while the other side at $x = L$ is subject to a symmetric boundary condition where the heat flux equals zero. The diagram also marks the location of the melt interface.

QUASI-STEADY SOLUTIONS

Due to the inherent challenges in obtaining exact solutions for models defined within finite domains, it is often necessary to seek out approximate solutions. In this context, we adopt the quasi-steady approximation, premised on the assumption that heat transfer occurs exclusively in one phase and the impacts of sensible heat are minimal when compared to those of latent heat. Consequently, all the heat released during solidification is attributed to the progression of the phase-change front. Given these conditions, it is reasonable to anticipate that this approximation could overestimate the actual location of the interface [136].

$$s(t) = \sqrt{2\mathrm{Ste}\,\alpha t} \quad 0 \leq s(t) \leq L \ ; \quad 0 \leq t \leq t_{melt} \tag{4.8}$$

$$\mathrm{Ste} = \frac{c(T_f - T_0)}{h_{sl}} \tag{4.9}$$

The position of the solid-liquid interface, $s(t)$, is a function of the elapsed time, the Stefan number, Ste, and the thermal diffusivity, α (as defined in Eq. 4.8). The progression of this interface is bounded by the semi-thickness of the slab, L. The time associated with this process is further constrained by the total melting time, t_{melt}. The Stefan number, a dimensionless parameter, is calculated from the specific heat capacity c, the temperature difference between the fusion temperature and the surface temperature $(T_f - T_0)$, and the latent heat of fusion h_{sl}. As defined in Eq. 4.9, the Stefan number quantifies the ratio of sensible heat $c(T_f{-}T_0)$ to the latent heat h_{sl}.

Consequently, from Equation 4.8, we can calculate the total melt time t_{melt} for the PCM slab when $s(t) = L$. Equation 4.10 furnishes the duration necessary for the entire solidification process to take place. Notably, this time period is directly proportional to the square of the slab thickness and inversely proportional to the product of the thermal diffusivity and the Stefan number.

$$t_{\text{melt}} = \frac{L^2}{2\alpha\,\text{Ste}} \tag{4.10}$$

Considering constant thermophysical properties and applying Fourier's law of heat conduction, the heat flux through the solid phase can be calculated using:

$$q''(t) = k\frac{T_0 - T_f}{s(t)} \tag{4.11}$$

As the solidification process progresses, the solid-liquid interface, denoted as $s(t)$, advances, leading to an increased thickness of the solid phase. This increased thickness results in greater thermal resistance to heat transfer, which in turn reduces the heat flux. The heat flux is inversely proportional to the square root of time, as captured by the above equation. As time elapses, the denominator, being proportional to $\sqrt{t}$, increases, and thus, the heat flux decreases. This equation succinctly encapsulates the temporal evolution of heat flux during the solidification process, reflecting the increasing thermal resistance due to the expanding solid phase.

Equation 4.12 represents the total heat flux $Q(t)$ across the solid phase, given as an integral of the instantaneous heat flux $q''(t)$, from the onset of solidification ($t = 0$) up to a specific point in time t. This integrated heat flux scales with the square root of time, i.e., $t^{0.5}$, and adheres to the same constraints as the solid-liquid interface $s(t)$, which are $0 \leq t \leq t_{\text{melt}}$.

$$\begin{aligned} Q(t) &= \int_0^t q''(t)\,dt \\ &= \sqrt{2\rho k(T_f - T_0)h_{sl}}\,t^{0.5} \quad 0 \leq t \leq t_{\text{melt}} \end{aligned} \tag{4.12}$$

Equation 4.13 demonstrates the relationship between the total heat flux $Q(t)$ and the mass of steam generated per unit surface area of the PCM, denoted by m_1. The heat flux is divided by the latent heat of vaporization h_{fg} to yield this mass. The steam generation scales with the square root of time.

$$m_1 = \frac{Q(t)}{h_{fg}} = \frac{\sqrt{2\rho k(T_f - T_0)h_{sl}}}{h_{fg}(T = T_0)} t^{0.5} \quad 0 \leq t \leq t_{\text{melt}} \tag{4.13}$$

In contrast, the rate of steam generation per unit surface area of the PCM, $\dot{m}_1$, is obtained by differentiating m_1 with respect to time (Equation 4.14). It is proportional to the inverse square root of time and thus decreases as time progresses, maintaining the same time bounds as before.

$$\dot{m}_1 = \frac{dm_1}{dt} = \frac{\sqrt{2\rho k(T_f - T_0)h_{sl}}}{2h_{fg}(T = T_0)} t^{-0.5} \quad 0 \leq t \leq t_{\text{melt}} \tag{4.14}$$

By substituting Eq. 4.10 into Eq. 4.13, we can obtain the maximum mass of steam per unit mass of the PCM as the ratio of the two latent heats, as shown below:

$$\frac{M_{\text{steam, max}}}{M_{\text{PCM}}} = \frac{h_{sl}}{h_{fg}(T = T_0)} \tag{4.15}$$

where M_{PCM} is the mass of a PCM pellet with thickness 2L and cross sectional area A. Considering a thin media ($L << A$), the total surface area of the PCM pellet is approximately 2A. Additionally, Eq. 4.15 can also be derived from an energy balance analysis. This analysis assumes that the latent heat transferred from the PCM is exclusively utilized for the phase change of water and does not contribute to raising the temperature of the water.

4.4.4 Solidification of Slab: Constant Heat Flux Boundary Condition

In this section, we will analyze the solidification of a slab of the PCM, but this time considering a constant heat flux boundary condition. Here, the solidification process is driven not by a fixed temperature difference, but by a constant rate of heat transfer, or heat flux, from the PCM to the surrounding water. This constant heat flux allows the generation of steam as the PCM slab undergoes phase change.

GOVERNING EQUATIONS

Similar to our previous analysis, Equation 4.16 is the heat diffusion equation without a heat generation term, and it represents how temperature T varies with time t and distance x within the solidifying PCM slab:

$$\frac{\partial^2 T}{\partial x^2} = \frac{1}{\alpha}\frac{\partial T}{\partial t} \quad 0 < x < s(t) \tag{4.16}$$

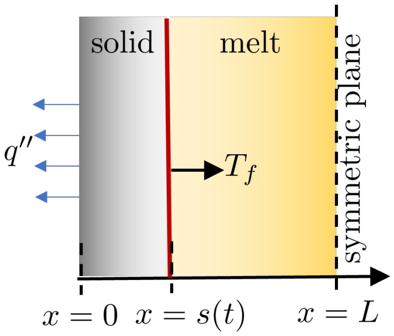

Figure 4.4: Schematic of a solidification of a slab with constant heat flux at the surface.

Unlike the previous scenario, the boundary condition and initial condition for this analysis are described by Equation 4.17. This equation indicates a constant heat flux at the surface, represented by q''_0, and states that before the onset of solidification, the slab was at the fusion temperature T_f. Also, the temperature at the solid-liquid interface and beyond ($x \geq s(t)$) remains constant at the fusion temperature T_f at any given time t.

$$-k\left(\frac{\partial T}{\partial x}\right)_{x=0} = q''_0 \quad \text{and} \quad T(x \geq s(t), t \geq 0) = T_f \tag{4.17}$$

Like the previous analysis with constant temperature boundary condition, the energy balance at the solid-liquid interface is governed by the Stefan condition represented by Eq. 4.18. The initial condition is defined by Eq. 4.19.

$$k\left(\frac{\partial T}{\partial x}\right)_{x=s} + \rho h_{sl}\frac{ds}{dt} = 0 \tag{4.18}$$

$$s(0) = 0 \tag{4.19}$$

QUASI-STEADY SOLUTIONS

The quasi-steady solution for the solid-liquid interface, $s(t)$, under constant heat flux boundary conditions is given by Eq. 4.20. Here, the solid-liquid interface position $s(t)$ grows linearly with time. The validity of this solution is within the bounds of the semi-thickness of the slab and the melting time.

$$s(t) = \frac{q''_0}{\rho h_{sl}}t \quad 0 \leq s(t) \leq L \;; \qquad 0 \leq t \leq t_{melt} \tag{4.20}$$

The total melting time, t_{melt}, under constant heat flux conditions can be obtained by substituting $s(t) = L$ into Equation 4.20. As a result, the total melt time is directly proportional to the slab thickness L, the density ρ, and the latent heat of fusion h_{sl}, and inversely proportional to the applied heat flux q_0''. This is given by Equation 4.21. This implies that for a given slab and a constant heat flux, the total melting time increases with the thickness of the slab.

$$t_{\text{melt}} = \frac{L\rho h_{sl}}{q_0''} \tag{4.21}$$

During charging or melting phase, the surface temperature $T_0(t)$ increases linearly with time due to the constant heat flux, as represented in Equation 4.22.

$$T_0(t) = T_f + \frac{q_0''^2}{k\rho h_{sl}} t \tag{4.22}$$

On the other hand, during discharging or solidification process, the surface temperature $T_0(t)$ decreases linearly with time as the heat is extracted from the slab, as represented in Equation 4.23.

$$T_0(t) = T_f - \frac{q_0''^2}{k\rho h_{sl}} t \tag{4.23}$$

This demonstrates that for a given slab and constant heat flux, the surface temperature changes linearly over time during both the charging and discharging processes.

This analysis assumes that the convective heat transfer coefficient between the surface of the PCM and the surrounding water is relatively large in the boiling regime. Consequently, the surface temperature of the PCM closely approximates the temperature of the water in the steam accumulator. Given the confined and pressurized conditions in the steam accumulator, the water temperature is assumed to have no spatial variation.

Under these conditions, the surface temperature of the PCM can be employed as the saturation temperature of the water, corresponding to the prevailing pressure. As this temperature declines, so too does the saturation pressure of the water, thereby enabling steam to exit at this decreased pressure.

The relationship between the saturation temperature of water and its corresponding saturation pressure is described by the Antoine equation (Equation 4.24) as follows.

$$\log_{10} P = A - \frac{B}{T_0(t) + C} \tag{4.24}$$

In this equation, P denotes the saturation pressure, T the saturation temperature, and A, B, and C are constants.

By utilizing the Clausius-Clapeyron equation and Antoine equation, we can derive a curve-fit equation to model the relationship between the saturation temperature and the corresponding enthalpy of vaporization of water. This equation can be used to fit a scatter plot of data points obtained from the steam table, providing a useful tool for predicting enthalpy values at different saturation temperatures.

$$h_{fg} = T_0(t)\left(A_1 - \frac{B_1}{T_0(t) + C_1}\right) \tag{4.25}$$

The mass of steam per unit surface area of the PCM generated can be computed from the heat flux $q''(t)$ and the time-varying enthalpy of vaporization h_{fg} as:

$$\begin{aligned} m_2 &= \int_0^t \frac{q''(t)}{h_{fg}}\, dt \\ &= G_1 \ln(1 + G_2 t) + G_3 \ln(1 + G_4 t) \quad 0 \le t \le t_{\text{melt}} \end{aligned} \tag{4.26}$$

The coefficients G_1, G_2, G_3 and G_4 are functions of the material properties of the PCM and the heat flux q_0'', defined as follows:

$$G_1 = \frac{k\rho h_{sl}}{(A_1C_1 - B_1)} \frac{B_1}{A_1} \tag{4.27}$$

$$G_2 = -\frac{q_0''}{k\rho h_{sl}(T_f - \frac{B_1}{A_1} + C_1)} \tag{4.28}$$

$$G_3 = -\frac{k\rho h_{sl}}{(A_1C_1 - B_1)} C_1 \tag{4.29}$$

$$G_4 = -\frac{q_0''}{k\rho h_{sl} T_f} \tag{4.30}$$

The rate of steam production per unit surface area of the PCM can be calculated by taking the derivative of Equation 4.26 with respect to time. This yields:

$$\dot{m}_2 = \frac{dm_2}{dt} = \frac{G_1G_2}{1 + G_2 t} + \frac{G_3G_4}{1 + G_4 t} \quad 0 \le t \le t_{\text{melt}} \tag{4.31}$$

The time dependency indicates that the rate of steam generation decreases as the PCM slab continues to melt.

Table 4.2: Steam generation capacity (kg) per m^3 for standard steam accumulator

	$P_1 \to$ (bar g)	1.8	1.9	2.0	2.2
P_2 (bar g)	T_{sat} (°C)	131.35	132.53	133.68	135.88
1.0	120.42	19.76	21.87	23.93	27.87
1.2	123.45	14.35	16.48	18.55	22.52
1.4	126.25	9.29	11.43	13.52	17.51
1.6	128.88	4.52	6.68	8.77	12.79
1.8	131.35	0	2.17	4.28	8.32
2.0	133.68	-	-	0	4.06

4.5 Results

4.5.1 Example System

Let the internal volume of the steam accumulator be 1 m^3 excluding the steam collection area overhead. The porosity of the packed bed, ϵ, is 0.5. The PCM is HDPE composite consisting of 15 % (by wt.) treated glass fibers. Therefore, the density of the composite is 1056 kg/m^3. The crystallization temperature of the composite is 132 ° C. Let us assume that the specific heat of the composite before and after cooling is 2.4 kJ/kg°C. The latent heat of solidification is approximately 160 kJ/kg. Let us consider a range of pressures from 1.0 bar(g) to 2.2 bar(g) as the operating pressures. From Equations 4.2 and 4.3 the steam generation capacity for a range of working pressures can be tabulated as shown in Table 4.2 and Table 4.3.

The steam accumulator is initially charged at a pressure P_1, and then discharges at a lower pressure P_2. In the conventional steam accumulator (Table 4.2a), the steam generation is directly proportional to the pressure drop from P1 to P2. A larger pressure drop (i.e., larger difference between P1 and P2) results in a higher steam generation capacity.

4.5.2 Capacity Enhancement

Figure 4.5a and b depicts a series of curves characterizing the relationship between the pressure drop from charging to discharging stages and the mass

Table 4.3: Steam generation capacity (kg) per m^3 for enhanced steam accumulator utilizing a 50 % porous packed bed of PCM composites with HDPE as the primary storage medium, at various operating pressures (bar g).

	$P_1 \rightarrow$ (bar g)	1.8	1.9	2.0	2.2
P_2 (bar g)	T_{sat} (°C)	131.35	132.53	133.68	135.88
1.0	120.42	15.54	51.74	53.36	56.47
1.2	123.45	11.29	47.63	49.26	52.39
1.4	126.25	7.30	43.78	45.42	48.57
1.6	128.88	3.55	40.15	41.81	44.97
1.8	131.35	0	36.73	38.39	41.57
2.0	133.68	-	-	0	3.19

Table 4.4: Fractional increase in steam generation achieved by using the packed bed method compared to a traditional steam generator.

	$P_1 \rightarrow$ (bar g)	1.8	1.9	2.0	2.2
P_2 (bar g)	T_{sat} (°C)	131.35	132.53	133.68	135.88
1.0	120.42	-0.21	1.37	1.23	1.03
1.2	123.45	-0.21	1.89	1.66	1.33
1.4	126.25	-0.21	2.83	2.36	1.77
1.6	128.88	-0.21	5.02	3.77	2.52
1.8	131.35	0	15.93	7.98	4.00
2.0	133.68	-	-	0	-0.21

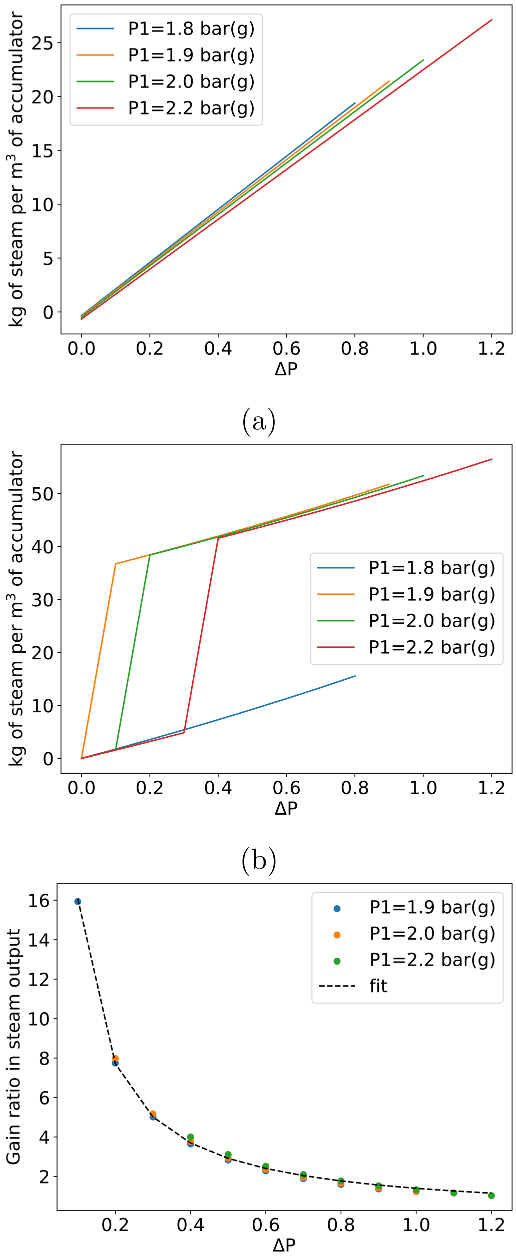

(a)

(b)

(c)

Figure 4.5: conventional (a) and packed bed (b) steam accumulator, max steam output, HDPE composite. (c) fractional gain

of steam generated per unit volume of saturated water. Each curve corresponds to a specific charging pressure. Fig. 4.5a pertains to a conventional steam accumulator. The relationship between pressure drop and steam mass generation appears linear, independent of the charging pressure. This observation is consistent with the principles governing conventional steam accumulators, where the steam generation primarily relies on the pressure drop. Contrastingly, Fig. 4.5b represents a packed bed steam accumulator. Here, the linear correlation between pressure drop and steam mass generation observed in the conventional case is supplemented by distinct jumps in steam mass generation at certain points. These abrupt increases correspond to the additional steam mass produced as a result of latent heat transfer from the phase change material (PCM) during its transition from a saturated water state to steam at the discharging pressure.

A critical observation in Fig. 4.5b arises from the behavior of the system at a charging pressure P_1 of 1.8 bar (g). Here, the corresponding saturation temperature is 131.35 ℃, marginally below the melting point of HDPE (132 ℃). Consequently, no discernible increase in steam output is observed with the decrease in pressure. However, for charging pressures where the corresponding saturation temperature surpasses the melting point of HDPE, a pressure drop that lowers the discharging pressure beneath the HDPE's melting point induces a sudden elevation in steam production.

Figure 4.5c delineates the fractional gain in steam production when implementing a packed bed steam accumulator in comparison to a conventional accumulator. In the current analysis, the resulting trend of percentage gain in steam output with respect to the increasing pressure drop adheres to an inverse power law relation.

It should be noted that this curve fit is only for a visual aid to see the trend and not a physical model to predict the values. In this case we have used the following equation for the non-linear curve fit:

$$y = \frac{a}{(x/c)^b} \tag{4.32}$$

where a = 1.07, b= 1.06, c = 1.28 bar(g).

We used the “scipy.optimize.curve_fit” module in python3 for the non-linear curve fitting using a least squares method. Here, 'y' represents the fractional gain (ratio of gain in steam output and conventional steam output) in steam output, and 'x' refers to the pressure drop. The trend exhibits a decrease in percentage gain with an escalation in the pressure drop, which can be

Table 4.5: Steam generation capacity (kg) per m^3 for standard steam accumulator

	$P_1 \rightarrow$ (bar g)	4.4	4.6	4.8	5.0
P_2 (bar g)	T_{sat} (°C)	154.85	156.25	157.60	158.92
3.6	148.83	11.2	13.8	16.3	18.8
3.8	150.41	8.3	10.9	13.4	15.9
4.0	151.94	5.5	8.1	10.6	13.0
4.2	153.42	2.7	5.3	7.9	10.3
4.4	154.85	0	2.6	5.2	7.7
4.5	155.55	-	1.3	3.9	6.3
4.6	156.25	-	0	2.6	5.0

primarily attributed to variations in the thermal contribution from the PCM.

At the solidification point of HDPE, the saturation pressure of water stands approximately at 1.855 bar (g). When the charging pressure escalates, both the PCM and water absorb an elevated amount of sensible heat. Nevertheless, the latent heat of vaporization of water substantially surpasses the sensible heat of both PCM and water. Therefore, when discharging from a higher charging pressure or in conditions of a larger pressure drop, the percentage gain in steam production tends to decrease.

In situations where the charging pressure falls below 1.855 bar (g), a negative gain is detected. Under such circumstances, the PCM maintains its solid state post the charging process, thus contributing only sensible heat during the discharging phase. As the specific heat capacity of HDPE is lesser to that of water, the steam output is reduced in comparison to the conventional steam accumulator, thereby resulting in a negative gain. This observation underscores the significance of the PCM's phase change, along with the associated latent heat transfer, in enhancing steam production in a packed bed steam accumulator.

Given the insights from the analysis, it is essential to address the influence of the packed bed's porosity on steam production. As demonstrated in the current model, a packed bed with 50% porosity ($\epsilon = 0.5$) exhibits a certain trend of steam production under varying charging and discharging pressures. However, it should be noted that porosity has a direct impact on the volume

Table 4.6: Steam generation capacity (kg) per m^3 for enhanced steam accumulator utilizing a 50 % porous packed bed of PCM composites with PP as the primary storage medium, at various operating pressures (bar g).

	$P_1 \rightarrow$ (bar g)	4.4	4.6	4.8	5.0
P_2 (bar g)	T_{sat} (°C)	154.85	156.25	157.60	158.92
3.6	148.83	8.1	46.1	47.9	49.6
3.8	150.41	5.97	44.1	45.9	47.6
4.0	151.94	3.9	42.1	43.9	45.7
4.2	153.42	1.9	40.2	42.0	43.8
4.4	154.85	0	38.3	40.2	42.0
4.5	155.55	-	37.4	39.3	41.0
4.6	156.25	-	0	1.8	3.6

Table 4.7: Fractional increase in steam generation achieved by using the packed bed method compared to a traditional steam generator.

	$P_1 \rightarrow$ (bar g)	4.4	4.6	4.8	5.0
P_2 (bar g)	T_{sat} (°C)	154.85	156.25	157.60	158.92
3.6	148.83	-0.28	2.34	1.93	1.65
3.8	150.41	-0.28	3.04	2.42	2.00
4.0	151.94	-0.28	4.22	3.15	2.50
4.2	153.42	-0.28	6.57	4.36	3.25
4.4	154.85	0	13.62	6.78	4.49
4.5	155.55	-	27.72	9.19	5.49
4.6	156.25	-	0	-0.28	-0.28

fraction of PCM within the bed, consequently affecting the latent heat storage and thus steam generation capabilities.

From the data and observations, it is reasonable to infer that a decrease in porosity would lead to an increase in the amount of PCM in the packed bed. With more PCM, the steam generation would potentially exhibit higher values, as the PCM could contribute more latent heat during phase change.

To better align the model with more practical or optimized scenarios, future calculations will be based on a packed bed with 20% porosity ($\epsilon = 0.2$). This adjustment aims to explore the steam generation capacity in a more dense packed bed configuration, which is hypothesized to result in enhanced performance in terms of steam output.

4.5.3 Steam Accumulator Performance at Constant Pressure Steam Output

In this subsection, we examine the behavior of the steam accumulator during steam discharge under constant pressure conditions. Such a condition is synonymous with maintaining a constant temperature boundary for the PCM slab. It is crucial to understand that a sustained boundary temperature for the PCM surface dictates that the steam's discharge occurs at its corresponding saturation pressure for that specific temperature. This understanding is underpinned by meticulous graphical analyses informed by our prior mathematical derivations, providing a systematic insight into the solidification process within this operational context. Leveraging the equations outlined in Section 4.4.3, we will showcase graphical representations that highlight the relationship between different parameters. For our examples, we use HDPE with a melting temperature of 134 °C, a density of 835 kg/m^3, and an enthalpy of melting of 192 kJ/kg.

Figure 4.6a illustrates the correlation between melt time (seconds) and the semi-thickness of the PCM (millimeters), as derived from equation 4.10. The equation suggests a parabolic trend between melt time and the square of the slab's semi-thickness. For this plot, we maintain a constant fluid inlet temperature of $T_0 = 133$ °C, leading to a steady temperature difference, ΔT of 1 °C and hence a constant Stefan number. The plotted curves, representing different thermal conductivities, vividly demonstrate an inverse proportionality between melt time and thermal conductivity.

Figure 4.6b plots elapsed time since the onset of solidification (measured

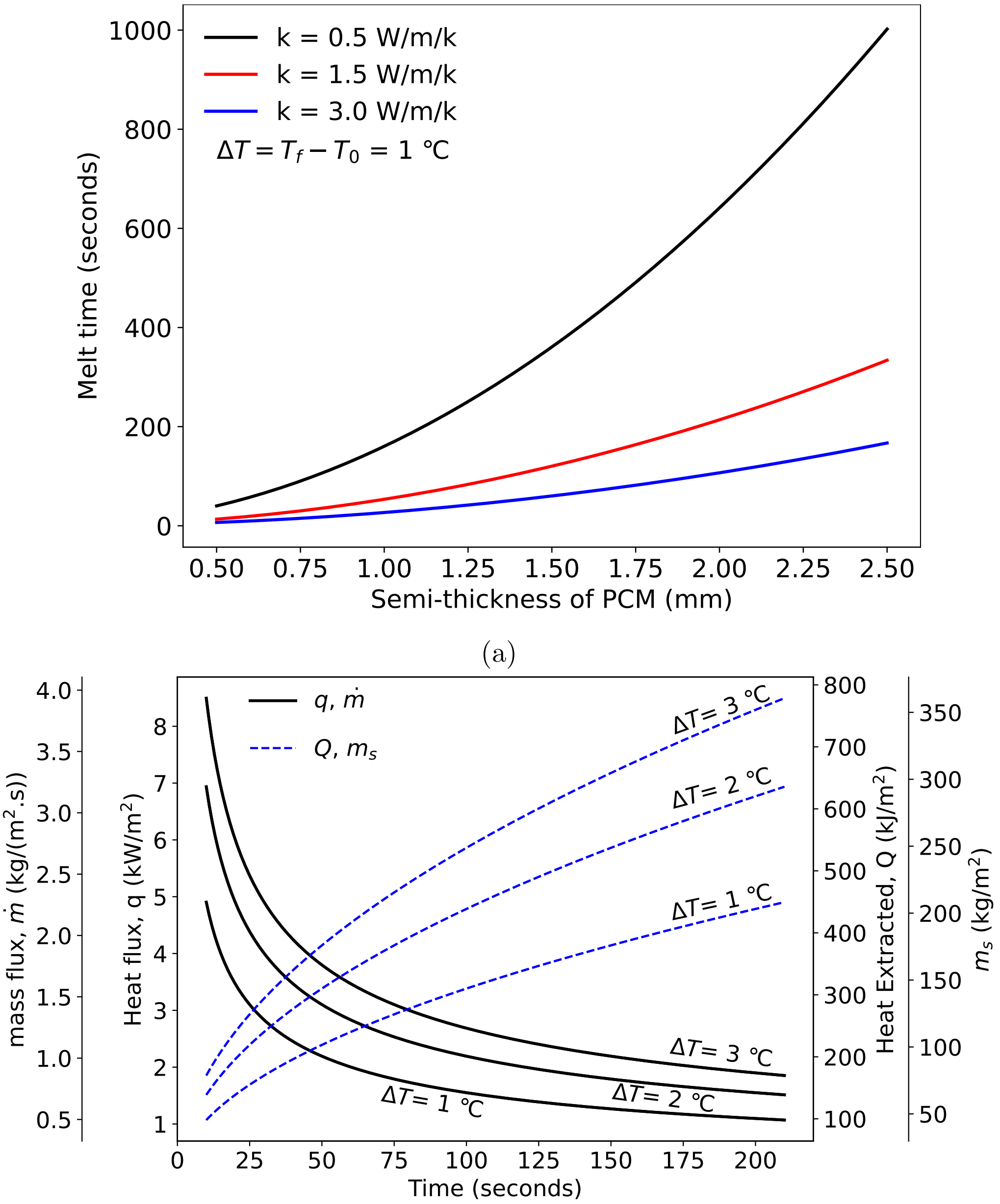

(a)

(b)

Figure 4.6: Relation between total accumulated mass of steam over a specific surface area of the PCM and mass flux of steam with time of discharge for constant surface temperature.

in seconds) against several parameters. On the primary Y-axis, we have both the heat flux (in kW/m^2, as per Eq. 4.11) and the mass flux (in kg/m^2·s, from Eq. 4.13). The secondary Y-axis on the right represents the heat extracted (in kJ/m^2, derived from Eq. 4.12) and the accumulated mass of steam per unit surface area of the PCM (in kg/m^2, based on Eq. 4.14). The heat flux and mass flux exhibit an inverse relationship with the square root of the elapsed time and are represented by solid black lines. Conversely, the heat extracted and the accumulated mass of steam per unit surface area of the PCM increase linearly with time and are depicted by dashed blue lines. For clarity, we've presented a series of curves for each relationship, corresponding to varying ΔT values of 1°C, 2°C, and 3°C.

In the model, an assumption was made that the sensible heat contribution from the PCM would be negligible when compared to its latent heat. To validate this assumption, we perform a simple comparison between the two forms of heat storage. The average specific heat capacity of HDPE is 2.0 kJ/kg ·°C and the latent heat of melting is 150 kJ/kg. For a temperature drop of 3 °C during the phase change process, the sensible heat contribution would be 6 kJ/kg. Thus, the ratio of sensible heat to latent heat is 0.04, which is also the Stefan number as given by Eq. 3.10. Since the Stefan number is much smaller than 1, this validates our initial assumption of neglecting the sensible heat contribution from the PCM in comparison to its latent heat. Consequently, treating the heat transfer process as quasi-steady is justified.

4.5.4 Steam Accumulator Performance at Constant Thermal Energy Output

In this subsection, our focus transitions to the steam accumulator's functionality when governed by a constant heat flux condition. Under these circumstances, the accumulator consistently delivers a uniform rate of thermal energy, a feature essential for applications that demand a consistent energy discharge over prolonged durations. This operation rests on maintaining a uniform heat transfer rate across the boundary of the PCM slab. By employing the mathematical framework established in section 4.4.4, we shall navigate the complexities and implications of this particular operational mode. We'll also use graphical analyses to show relationships between key parameters in the context of a consistent heat flux boundary.

In a packed bed system with 20% porosity, 80% of the bed volume is filled by the PCM, with the remaining 20% consisting of water. Given the densities and specific heats of both the PCM and water, their combined sensible heat can be determined as a weighted sum of their individual sensible heat contributions. Specifically, for a 1 m^3 volume undergoing a temperature drop of 3°C, the sensible heat contributions from the PCM and water amount to 5068.8 kJ and 2347.2 kJ, respectively. These calculations use a water density of

932 kg/m^3 at the operating temperature [141]. When comparing this combined sensible heat to the latent heat, assuming the entire volume to be PCM, the combined sensible heat accounts for approximately 4.68% of the latent heat. This implies that, in this context, the latent heat contribution is substantially greater than the sensible heat. Hence, for the purposes of this study, using the PCM volume as an approximation is reasonable. Nonetheless, for more accurate outcomes or for different scenarios, accounting for the sensible heat contributions from both PCM and water in the packed bed is advised. In subsequent analyses where the mass of steam generated per unit volume is discussed, it is implicitly understood that this refers to the volume occupied by the PCM.

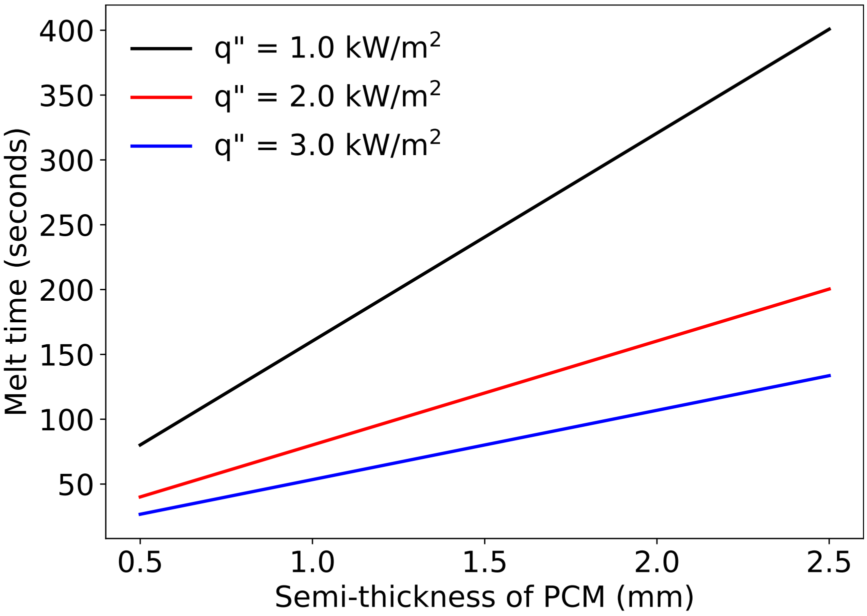

Figure 4.7: Melt time as influenced by the thickness of the PCM slab for varying heat flux values.

Figure 4.7 represents the temporal aspect of the solidification process as influenced by the slab's thickness and the applied heat flux. In the presented figure, three distinct heat flux values have been employed for visualization: 1 kW/m^2, 2 kW/m^2, and 3 kW/m^2. As articulated by Eq. 4.21, there exists a linear dependency of the melt time on the thickness of the PCM. Concurrently, the melt time exhibits an inverse proportionality to the heat flux.

Figure 4.8 depicts the variation of steam temperature and corresponding output pressure with the discharge time, as indicated by Eq. 4.23. The represented steam temperature approximates the surface temperature of the PCM, justified by the large convective heat transfer coefficient in the phase change regime which allows the water's temperature to be considered uniform

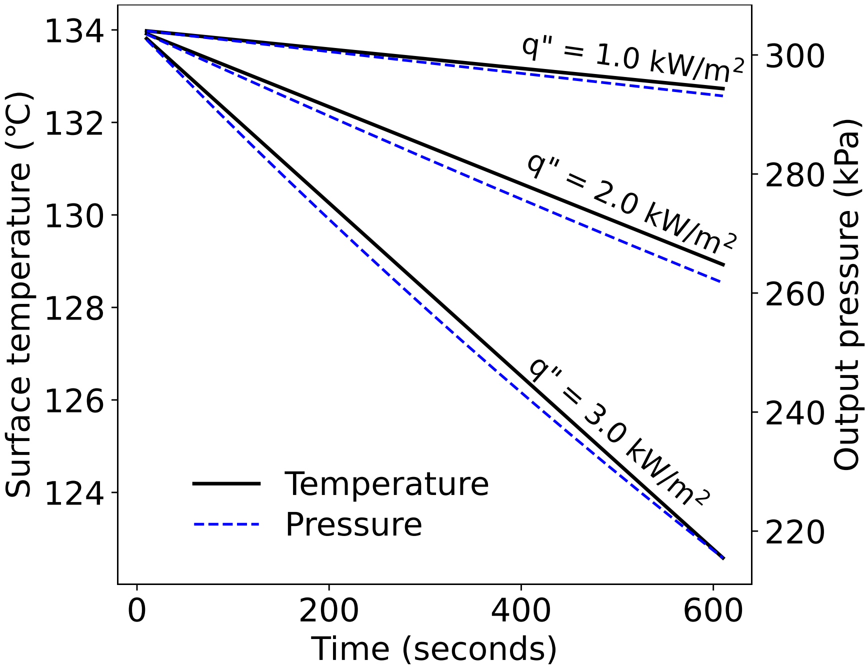

Figure 4.8: Evolution of steam temperature and its associated output pressure during discharge time.

and equivalent to the PCM's surface temperature. The pressure, derived from the Antoine relationship (Eq. 4.24), corresponds to the saturation pressure of water at the given temperature. The graphical representation demonstrates a linear decline in temperature over time, while the pressure exhibits a subtle non-linearity. Three distinct curves are based on heat flux values of 1 kW/m^2, 2 kW/m^2, and 3 kW/m^2. The evident faster drop in temperature for higher heat fluxes stems from its squared dependency on the heat flux.

In Figure 4.9, we delve into a comprehensive representation of the interplay between discharge time and two critical parameters. Firstly, the heat extracted per unit surface area of the PCM is plotted against the discharge time on the primary Y-axis. This heat is computed as the product of the constant heat flux and the time elapsed. Parallelly, on the secondary Y-axis, we observe the mass of steam delivered per unit surface area of the PCM, determined using Eq. 4.26. For clarity and comparative insights, data is presented across three distinct heat flux values: 1 kW/m^2, 2 kW/m^2, and 3 kW/m^2. Further scrutiny into equations 4.27 - 4.30 reveals that values for G_2 and G_4 are very small, on the order of 10^{-8}. This minuteness allows for a simplification using Taylor series expansion applied to Eq. 4.26. The equation evolves into a form that is effectively linear in time, as represented by:

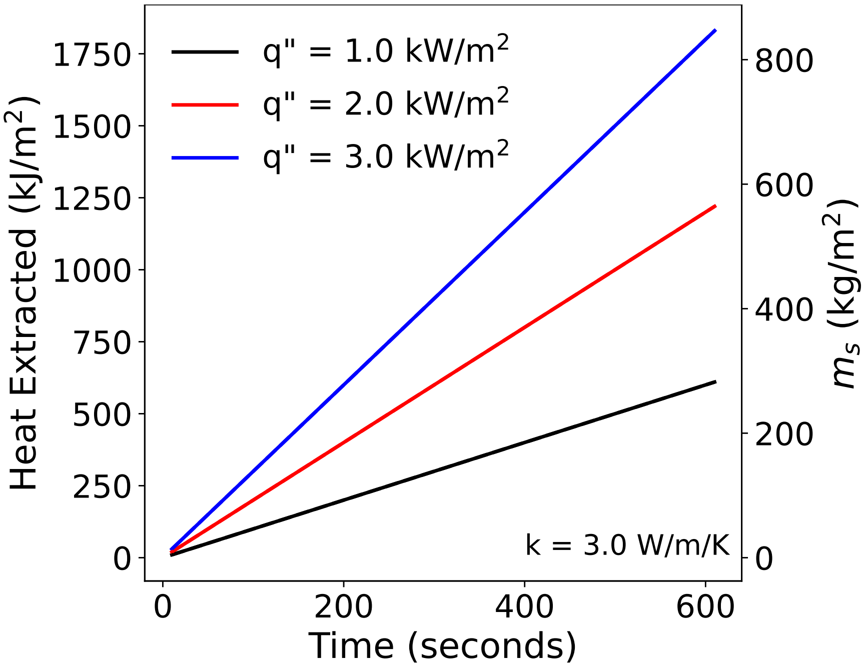

Figure 4.9: Relation between the total accumulated mass of steam per unit surface area of the PCM and the heat extracted with respect to the time of discharge, under conditions of constant surface heat flux

$$\begin{aligned} m_2 &= G_1 \ln(1 + G_2 t) + G_3 \ln(1 + G_4 t) \\ &\approx (G_1 G_2 + G_3 G_4)t \quad 0 \le t \le t_{\text{melt}} \end{aligned} \tag{4.33}$$

Consequently, despite the inherent non-linearity, in practical scenarios, the steam produced showcases a linear progression. This implies a constant steam production rate, quantified as $(G_1G_2 + G_3G_4)$.

To derive the relationship between the heat extracted, $Q(t)$ and the output pressure, we merge equations 4.24 and 4.23. Using the relation $Q(t) = q_0''t$, we can express t in terms of Q. For practical applications, we can simplify this relationship further using the Taylor series expansion to approximate certain nonlinear behaviors.

$$\begin{aligned} \log_{10} P &= A - \frac{B/(T_f + C)}{1 - q_0''Q/(k\rho h_{sl}(T_f + C))} \\ &\approx A - \frac{B}{T_f + C}\left(1 + \frac{q_0''Q}{k\rho h_{sl}(T_f + C)}\right) \end{aligned} \tag{4.34}$$

Therefore,

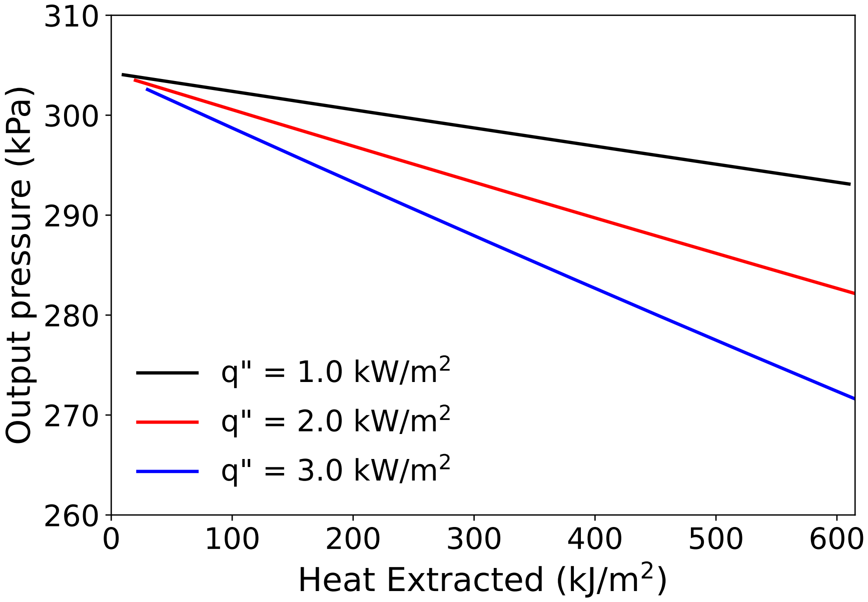

Figure 4.10: Relation between total heat extracted versus the output pressure.

$$
\begin{aligned}
P &= \exp\left(-\frac{q_0''B}{k\rho h_{sl}(T_f+C)^2}Q\right)\exp\left(A-\frac{B}{T_f+C}\right)\\
&\approx \left(1-\frac{q_0''B}{k\rho h_{sl}(T_f+C)^2}Q\right)\exp\left(A-\frac{B}{T_f+C}\right)
\end{aligned}
\tag{4.35}
$$

The fact that certain terms, specifically $q_0''/(k\rho h_{sl}(T_f+C))$ and $q_0''B/(k\rho h_{sl}(T_f+C)^2)$, are of a much smaller magnitude, on the order of 10^{-7} allows us to linearize an inherently nonlinear relation, making it easier to analyze and understand.

In Figure 4.10, the relationship delineated by Eq. 4.35 is visually represented. It is evident from the figure that the output pressure linearly diminishes with the increasing extracted heat. This observation aligns with the findings from Figures 4.8 and 4.9. In these figures, we observe a nearly linear decline in output pressure over time, while the extracted heat exhibits a linear growth with time. These consistent observations across the figures reinforce the validity of the theoretical derivation.

4.5.5 TES Economics through Low-Power Heat Pump Integration

TES systems are increasingly recognized for their potential to enhance energy efficiency and contribute to sustainability objectives. However, the economic feasibility of deploying TES systems remains a subject of scrutiny and ongoing research. This section aims to address this gap by examining the eco-

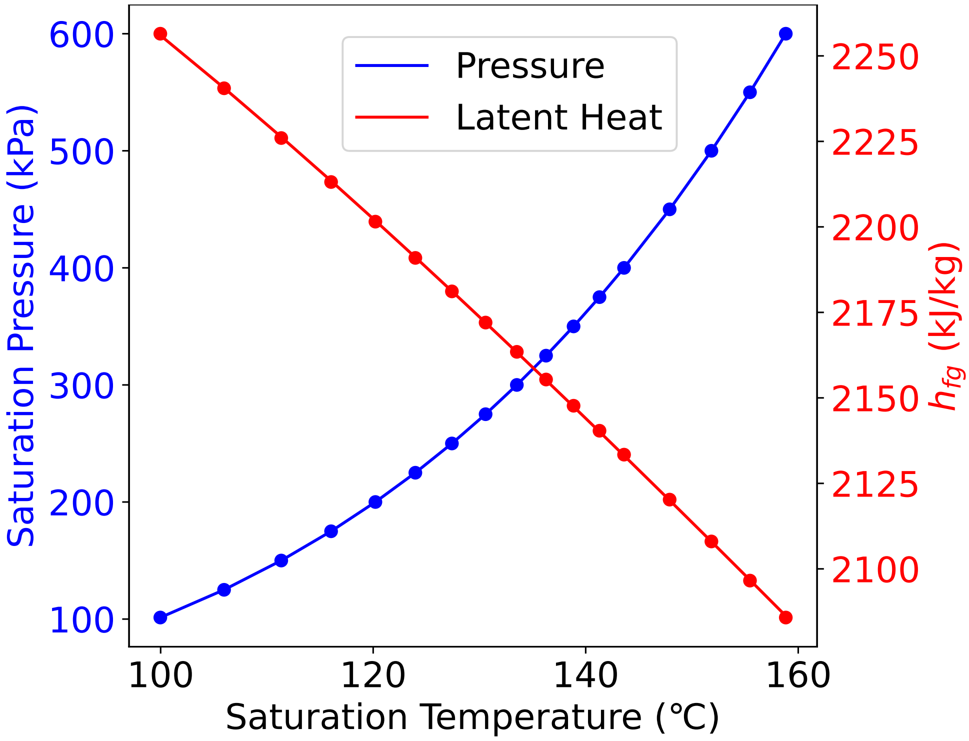

Figure 4.11: Variation of saturation pressure (kPa), latent heat of vaporization (kJ/kg), and saturation temperature (℃) of water between 100 ℃ to 160 ℃. The data for saturation pressure is fitted using the Antoine equation (Eq. 4.24) with parameters A = 7.0361, B = 1631.9818 °C, C = 224.4498 °C. The root mean squared error of the fit is 0.023. The data for latent heat of vaporization is also curve-fitted (Eq. 4.25) with parameters A_1 = -3.5458 kJ/(kg °C), B_1 = -2718.2939 kJ/kg, C_1 = 4.1282 °C. The corresponding root mean squared error is 0.257 kJ/kg.

nomic implications of integrating low-power heat pumps into TES systems. We introduce a cost-benefit analysis that evaluates two scenarios:

1. A high-power heat pump operating at d duty cycle (e.g., d=0.1,0.2,0.3,. . .).
2. A low-power heat pump operating at 100% duty cycle, coupled with a TES system.

For the first scenario, the high-power heat pump provides thermal energy to a given process intermittently, operating only during its d duty cycle. Due to its higher power requirements, the capital expenditure for this setup is considerably elevated.

Conversely, in the second scenario, a low-power heat pump operates at a constant 100% duty cycle. It splits its operational time between supplying thermal energy directly to the process and charging a TES system. Upon reaching full charge, the TES system can independently provide the required thermal energy to the process.

The key insight here revolves around the cost disparity between high- and low-power heat pumps. Specifically, the reduced capital cost of the low-power heat pump presents an economic advantage that potentially offsets the cost of installing a TES system. This section will delve into this interplay, quantifying how the capital cost savings from opting for a low-power heat pump could be reinvested into a TES system to make the overall setup more cost-effective.

d is a dimensionless value that represents the duty cycle of the heat pump. The variable x signifies the duration, in seconds, during which the heat pump is in operation to charge the TES system. Additionally, we introduce a constant R, which serves as a rate constant with units of inverse seconds (s^{-1}). We can derive an equation for the fractional savings achieved by installing a heat pump coupled with a TES system as opposed to using a high-power heat pump alone. This is given in terms of the capital cost of the high-power heat pump, as shown in Eq. 4.36.

$$\frac{\text{saving}}{\text{capital cost of heat pump}} = 1 - d(1 + Rx) \tag{4.36}$$

where,

$$R = \frac{\text{TES cost per kilo-Joule}}{\text{Heat Pump cost per kilo-Watt}} \tag{4.37}$$

In Equation 4.36, the term R is defined as the ratio of the cost per kilo-Joule of the TES system to the cost per kilo-Watt of the heat pump, as shown in Equation 4.37. This parameter encapsulates the relative capital costs of the two systems and is crucial for determining the economic feasibility of integrating a TES system with a low-power heat pump.

$$\text{TES cost per kilo-Joule} = \frac{\text{TES cost per kg PCM}}{\text{Energy stored per kg PCM}} \tag{4.38}$$

$$= \frac{(\text{Tank cost} + \text{Total PCM cost})/\text{Mass of PCM}}{\text{Energy stored per kg PCM}} \tag{4.39}$$

In this cost efficiency analysis, the primary focus is on the key components of the TES system—namely, the tank and the PCM. The "TES cost per kilo-Joule" is calculated as a function of these primary cost drivers. The

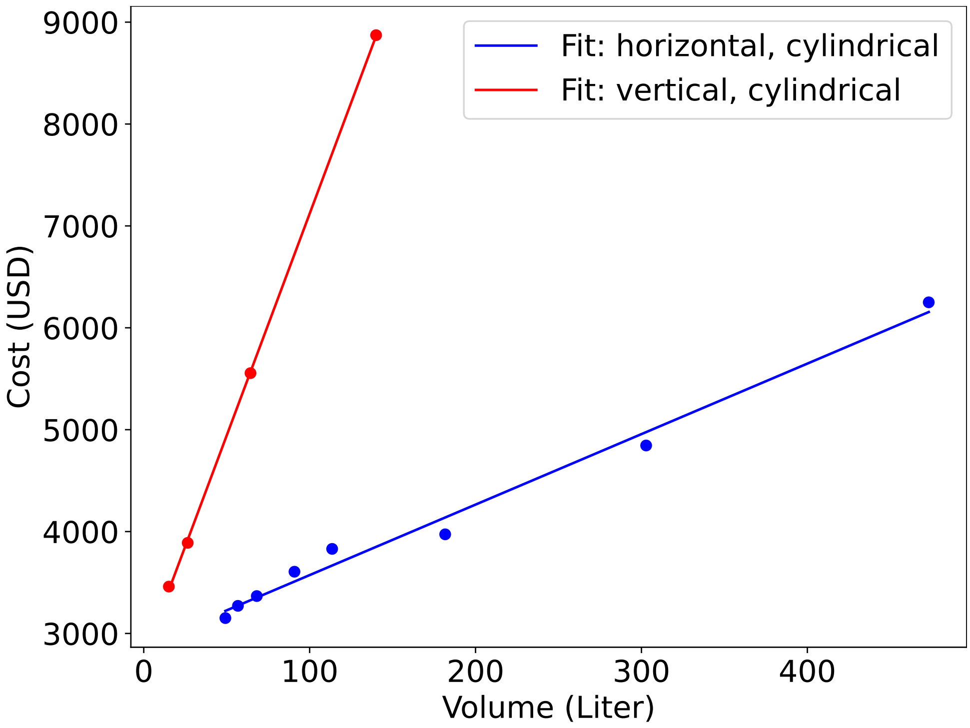

Figure 4.12: Cost vs. volume for steam flash tanks. Blue points represent horizontal cylindrical tanks, while red points represent vertical cylindrical tanks. The lines of best fit illustrate the linear relationship between volume and cost for each tank type. Units for volume and cost are liters and USD, respectively.

numerator represents the sum of the tank and total PCM costs, normalized by the mass of the PCM used. This sum is then divided by the ”Energy stored per kg PCM,” essentially representing the unit cost of the stored thermal energy.

Figure 4.12 illustrates a comparative analysis of the cost-to-volume ratio for two distinct types of flash tanks: horizontal cylindrical and vertical cylindrical. Linear regression fits for both the types show a positive correlation between the volume (in Liters) and the cost (in USD), implying that larger tanks are more expensive, as anticipated. The rate of cost increase with respect to volume is different between the two types. The lower slope for the horizontal cylindrical tanks suggests that for this type, the increase in manufacturing cost is more gradual than that for vertical cylindrical tanks. Henceforth, the horizontal tanks are considered for this cost analysis.

Table 4.8 presents an analysis of various TES tanks: their costs and features. The tanks are filled with a neutrally buoyant HDPE composite, which serves as the PCM. A packed bed setup with 20% porosity is considered, and it is observed that the mass of the PCM required scales favorably with increasing

Table 4.8: Comparison of thermal energy storage tanks. ”Vol (Ga)” and ”Vol (L)” indicate the volume in gallons and liters, respectively. ”Cost (USD)” is the flash tank cost, while ”TES Cost” also includes the cost of the Phase Change Material and flash tank. ”TES Cost/kg” denotes the cost of Thermal Energy Storage per kilogram of PCM. ”Orientation” describes whether the tank is horizontal or vertical, along with its shape.

Vol (Ga)	Vol (L)	Tank Cost (USD)	TES Cost (USD)	TES cost/kg (USD)/kg	Orientation
13	49.2	3,151	3,159	64.21	horz., cyl
15	56.8	3,271	3,280	57.75	horz., cyl
18	68.1	3,367	3,378	49.60	horz., cyl
24	90.8	3,606	3,621	39.88	horz., cyl
30	113.6	3,830	3,848	33.87	horz., cyl
48	181.7	3,973	4,002	22.03	horz., cyl
80	302.8	4,845	4,893	16.16	horz., cyl
125	473.2	6,250	6,325	13.37	horz., cyl
4	15.1	3,460	3,462	229.27	vert., cyl
7	26.5	3,889	3,893	146.91	vert., cyl
17	64.4	5,555	5,565	86.41	vert., cyl
37	140.1	8,872	8,894	63.48	vert., cyl

tank volume. This trend is evident in the declining "TES cost/kg" values as the tank sizes grow, particularly for horizontal cylindrical configurations.

To compute the PCM price, online data for recycled mixed-color HDPE [154] is used. The cost of the PCM is added to the base tank cost to derive the total TES cost, which is subsequently normalized per kilogram of PCM for easier comparison.

Figure 4.13 reveals a non-linear decrease in normalized TES cost as tank volume increases. This trend is well-described by the equation $a + b/v$, where v is the tank volume in liters, a = 7.4 USD/kg, and b = 2851.15 USD-L/kg. Assuming a TES cost of 12.5 USD/kg and a heat delivery capacity of approximately 200 kJ/kg within the operating temperature range, the cost per kJ of stored thermal energy is about 1/16th USD.

The TES cost is mainly influenced by two components: the tank and the PCM. The tank represents the more variable cost element, while the PCM cost becomes increasingly less significant with the upscaling of tank size, partly due to bulk purchasing efficiencies. This decreasing TES cost per kg of PCM for larger volumes indicates that investing in bigger systems could offer long-term economic advantages. This insight is particularly relevant for scalable thermal energy storage applications that demand large volumes.

Table 4.9 and Table 4.10 illustrate the fractional savings in dollars achieved by using a heat pump coupled with a TES system, as opposed to using a high-power heat pump alone. The capital costs of the high-power heat pumps are set at 250 USD/kW and 1000 USD/kW, respectively. The fractional savings are computed according to Eq. 4.36 and are based on varying duty cycles and operational durations. Figure 4.14 reveals a linear relationship between the savings and the TES charging time. The tables indicate that as the duty cycle and operational duration increase, the fractional savings tend to decrease.

Based on the tables and Eq. 4.36, it is evident that shorter charging times lead to greater fractional savings, particularly at lower duty cycles. Shorter charging times not only maximize savings but also imply a smaller TES size, which is advantageous. A lower duty cycle necessitates a more powerful heat pump to achieve the same average power output. Consequently, as duty cycle decreases, the capital investment in the heat pump increases, which in turn enhances the fractional savings relative to the heat pump's capital cost.

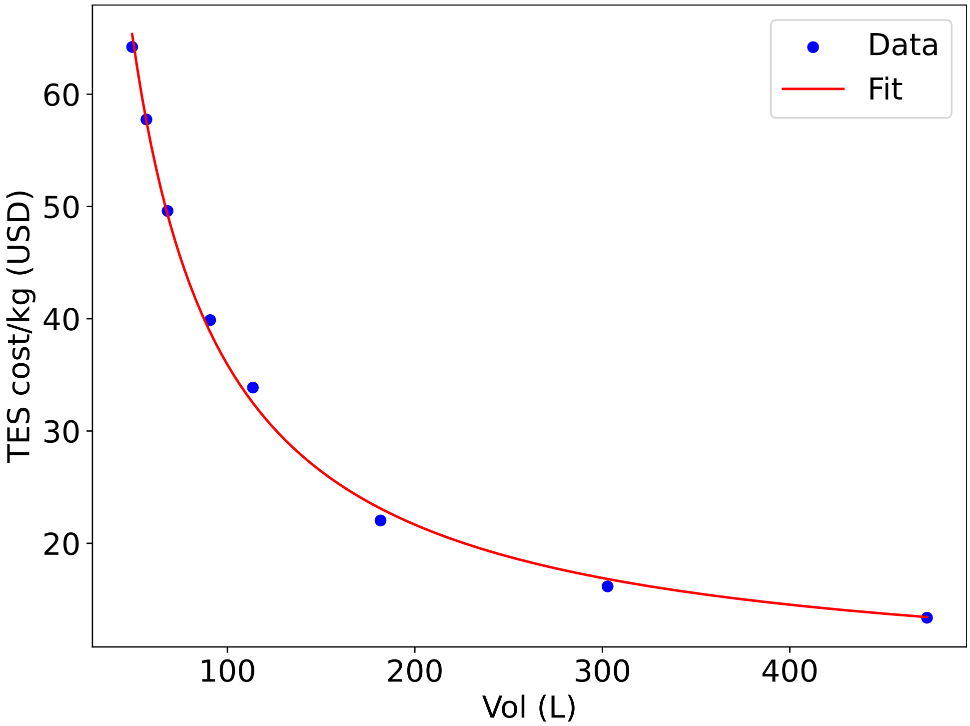

Figure 4.13: Relationship between the volume (in liters) and the thermal energy storage (TES) cost per kilogram (in USD) for horizontal tanks. The red curve represents the best-fit model, cost/kg = 7.40 + 2851.15/Vol (L), which closely fits the observed data with an R^2 value of 0.998 and a Root Mean Square Error of 0.869. The TES cost consist of the cost of the PCM in it and the tank.

Table 4.9: Fractional savings in dollars based on a heat pump capital cost of 250 USD/kW.

X (hr)	Fractional Saving ($)		
	d: 0.1	0.2	0.3
0.5	0.855	0.71	0.565
1	0.81	0.62	0.43
1.5	0.765	0.53	0.295
2	0.72	0.44	0.16
2.5	0.675	0.35	0.025
3	0.63	0.26	-0.11
3.5	0.585	0.17	-0.245
4	0.54	0.08	-0.38
4.5	0.495	-0.01	-0.515
5	0.45	-0.1	-0.65

Table 4.10: Fractional savings in dollars based on a heat pump capital cost of 1000 USD/kW.

X (hr)	Fractional Saving ($)		
	d: 0.1	0.2	0.3
1	0.8775	0.755	0.6325
2	0.855	0.71	0.565
3	0.8325	0.665	0.4975
4	0.81	0.62	0.43
5	0.7875	0.575	0.3625
6	0.765	0.53	0.295
7	0.7425	0.485	0.2275
8	0.72	0.44	0.16
9	0.6975	0.395	0.0925
10	0.675	0.35	0.025

4.5.6 Comparison with Existing Steam Accumulator Models

Steinmann and Eck [117] in their study, estimate the total mass of saturated steam generated during the discharge process in a pressure drop steam accumulator. They use approximations for both the specific heat capacity of liquid water and the latent heat of vaporization of steam, calculated at the average pressure based on the charging and discharging pressures. These approximations will result in an error of approximately 9% for the specific heat capacity value and 10% for the latent heat when assuming a pressure drop from 100 bar to 55 bar. In contrast, this work does not utilize average values for these parameters. Furthermore, Steinmann and Eck's model is limited to conventional pressure drop steam accumulators. Shnaider *et al.* [155] utilize the ideal gas law to approximate the interplay between steam temperature, pressure, and density. This approximation is notably imprecise for steam that is either saturated or approaching a saturated state. When a pressure drop from 100 bar to 50 bar is assumed, the error incurred by treating saturated steam as an ideal gas stands at 49.5% at 100 bar and 25.7% at 50 bar. Abdelsalam *et al.* [156] aims to explore the potential of hybrid thermal energy storage systems, focusing on the impact of key PCM design parameters like volume fraction and module spacing. The authors use a lumped system approximation to model PCM modules, assuming a spatially uniform temperature. While the study offers valuable insights into

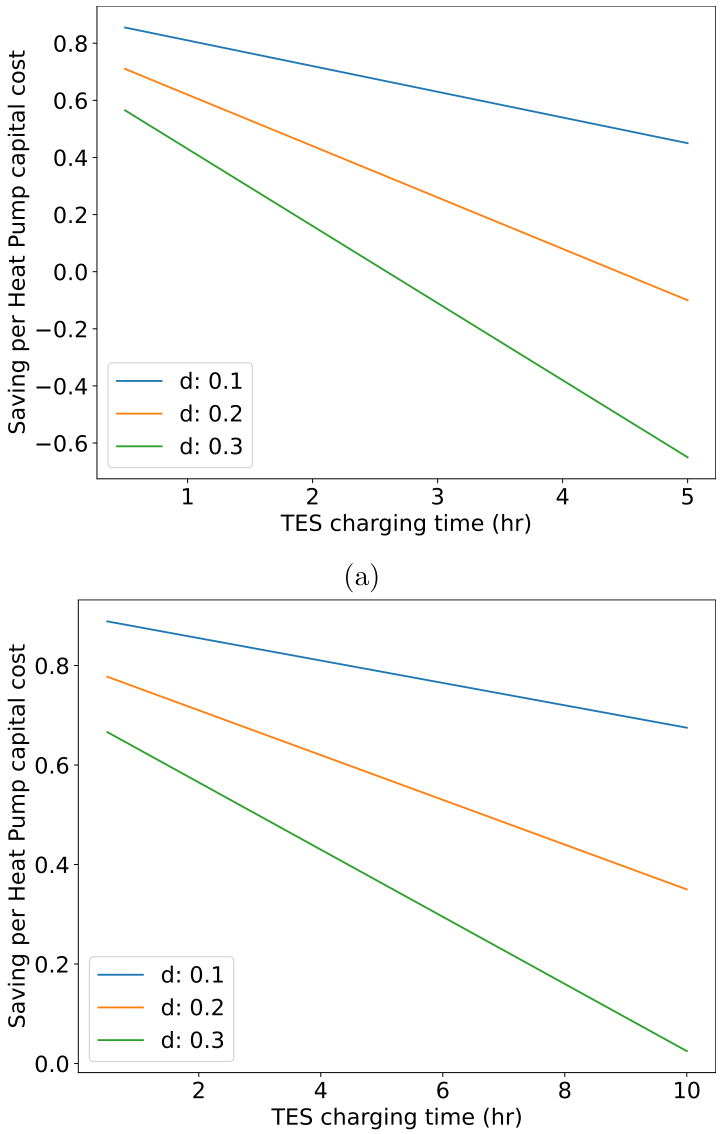

(a)

(b)

Figure 4.14: Fractional savings achieved using a TES system coupled with a heat pump versus a high-power heat pump alone. The capital costs of the high-power heat pump are set at (a) 250 USD/kW and (b) 1000 USD/kW. Savings are calculated for a range of duty cycles (from 0.1 to 0.3) and operational durations, as per Eq. 4.36.

PCM design parameters, the use of lumped system approximation poses limitations. It works best when the PCM has really good thermal conductivity or the modules are very thin. For PCMs that don't fit this criteria, the model might not give accurate results. Specifically, the approximation overlooks transient effects affecting the melt front, which varies with time. In contrast, our research takes these transient effects into account, allowing for a more comprehensive understanding of the system.

4.6 Conclusion

This chapter has provided an in-depth analysis of steam generation capacities in pressure-drop steam accumulators, comparing traditional setups with those incorporating Phase Change Material (HDPE composite) in a packed bed configuration. A detailed thermodynamic framework was used for this purpose, supplemented by a quasi-steady approximation approach to account for latent heat effects during phase changes. This analysis has been conducted under two operational contexts—constant pressure and constant thermal energy output. Deviations in performance between conventional and PCM-enhanced packed bed accumulators were identified and analyzed, particularly under varying working pressures.

Chapter 5

Conclusions

This concluding chapter synthesizes the research findings presented in the preceding chapters, offering a comprehensive overview of the work undertaken. It begins by revisiting the initial research objectives and summarizing the key findings, shedding light on the contributions made to the field of Latent Heat Thermal Energy Storage using polymeric materials. Subsequently, this chapter will address the limitations of the present study, providing a perspective on the research conducted. Furthermore, potential avenues for future research will be explored, delineating the next logical steps for extending the current study.

The crux of this research has been to advance the understanding and application of high-density polyethylene composites as phase change materials in latent heat thermal energy storage systems. Throughout the chapters, a multi-scale approach has been employed to assess the material properties, system performance, and practical implications of these composites.

Chapter 2 provided a foundational understanding of a bench-scale experimental setup. It established the efficacy of high-density polyethylene composites reinforced with glass fiber and epoxy resin in medium-temperature applications requiring heat below 120 °C. The thermophysical characterization confirmed the composite's stability over numerous melting and solidification cycles, substantiating its thermal capacity exceeding 160 kJ/kg.

Chapter 3 expanded upon these findings with a pilot-scale study that introduced a novel composite phase change material comprising high-density polyethylene and polyester fibers. The chapter illustrated the system's ability to be discharged at rates exceeding 70 W/kg, and the thermal capacity was found to be over 190 kJ/kg for high-density polyethylene. Moreover, the long-term stability and cost-effective manufacturability of the composite were confirmed.

Chapter 4 moved beyond storage to focus on the application of the high-density polyethylene composite in rapid steam production. A mathematical framework was developed to quantify the thermal performance of PCM-enhanced steam accumulators, revealing conditions under which the packed-bed accumulator could outperform traditional systems.

By sequentially progressing from material characterization to pilot-scale testing and, finally, to application-based performance assessment, this research presents a holistic view of the high-density polyethylene composites' capabilities and limitations. The integrated findings substantiate the material's high thermal capacity, efficient heat transfer, and operational stability, thereby making a compelling case for its application in medium-temperature thermal energy storage systems.

5.1 Summary of Research Findings

As mentioned in Chapter 1, Section 1.10, the central focus of this thesis was to delve into the viability and performance of high-density polyethylene composites as phase change materials in latent heat thermal energy storage systems, tailored for medium-temperature operations demanding heat below 120°C. The research primarily aimed to assess the thermal and mechanical characteristics of these composites at a bench-scale, corroborate these outcomes through more extensive pilot-scale experiments to gauge their practical relevance, and to understand the composite's ability for quick steam generation and its augmentative effects in a steam accumulator.

Major Findings

1. Bench-Scale Experimental Study:

   The high-density polyethylene composite, enhanced by glass fiber and epoxy resin, demonstrated promising thermal properties with a latent heat capacity exceeding 160 kJ/kg. A packed-bed setup with direct contact to a heat transfer fluid (glycerol) was found to offer superior heat exchange performance. The bench-scale experiments verified that the system could be operated at high rates with energy densities of greater than 100 W/kg, maintaining an exergetic efficiency averaging around 79%.

2. Pilot-Scale Experimental Study:

   A more advanced composite, consisting of high-density polyethylene and polyethylene terephthalate, was created and tested in a pilot-scale setup. It showed a latent heat value over 190 kJ/kg, and the system was successfully discharged at rates exceeding 70 W/kg. The study confirmed that the composite had minimal deformation and leakage potential, indicating its long-term stability.

3. Rapid Steam Production and Performance Enhancement:
   A thermodynamic framework was developed to understand the capabilities of steam accumulators incorporating the high-density polyethylene composite. The research revealed that the phase change material-enhanced packed bed system could potentially outperform traditional steam accumulators under certain conditions. This enhancement was particularly evident when the system was operated under constant pressure or thermal energy output contexts.

By meeting these objectives, this thesis contributes to the growing body of research on sustainable energy storage solutions. It particularly sheds light on how polymeric materials can be effectively used as phase change materials in thermal energy storage systems for medium-temperature applications.

5.2 Future Work

The investigations into high-density polyethylene composites as phase change materials in latent heat thermal energy storage systems have yielded compelling evidence of their utility and effectiveness, particularly for medium-temperature applications. One prospective avenue for extended study could involve bench-scale testing of the steam accumulator system. Such an endeavor would enable a more nuanced understanding of transient heat and mass transfer phenomena under realistic operational conditions.

As the technology matures, consideration should be given to the commercialization prospects of these composite materials in steam accumulator systems. Collaborative pilot studies, potentially facilitated by industrial partnerships, could evaluate the economic feasibility and scalability of the technology. Additionally, a techno-economic analysis comparing the life-cycle costs, environmental impact, and return on investment between conventional and composite-based steam accumulator systems could provide valuable insights. Such an analysis would be instrumental in gauging the economic competitiveness of this novel technology, a crucial factor for its broader acceptance and implementation.

By contemplating these research extensions, this thesis sets the stage for a multifaceted and long-term inquiry into the promising domain of latent heat thermal energy storage systems, thereby inviting further scientific scrutiny and commercial interest.

Bibliography

[1] Ioan Sarbu and Calin Sebarchievici. A comprehensive review of thermal energy storage. *Sustainability*, 10(1):191, 2018.

[2] Ioan Sarbu and Calin Sebarchievici. *Solar heating and cooling systems: Fundamentals, experiments and applications.* Academic Press, 2016.

[3] *Thermal Energy Storage (TES) - Global Market Trajectory & Analytics, Report, ID: 3440898.* Global Industry Analysts, Inc, May 2021.

[4] *Thermal Energy Storage (TES) - Global Market Trajectory & Analytics, Report, ID: 3329768.* Global Industry Analysts, Inc, Sept 2020.

[5] Atul Sharma, V Veer Tyagi, CR Chen, and Dharam Buddhi. Review on thermal energy storage with phase change materials and applications. *Renewable and Sustainable energy reviews*, 13(2):318–345, 2009.

[6] YB Tao and Ya-Ling He. A review of phase change material and performance enhancement method for latent heat storage system. *Renewable and Sustainable Energy Reviews*, 93:245–259, 2018.

[7] Ali Fallahi, Gert Guldentops, Mingjiang Tao, Sergio Granados-Focil, and Steven Van Dessel. Review on solid-solid phase change materials for thermal energy storage: Molecular structure and thermal properties. *Applied Thermal Engineering*, 127:1427–1441, 2017.

[8] Huili Zhang, Jan Baeyens, Gustavo Cáceres, Jan Degreve, and Yongqin Lv. Thermal energy storage: Recent developments and practical aspects. *Progress in Energy and Combustion Science*, 53:1–40, 2016.

[9] Jose Pereira Da Cunha and Philip Eames. Thermal energy storage for low and medium temperature applications using phase change materials–a review. *Applied energy*, 177:227–238, 2016.

[10] Ben Xu, Peiwen Li, and Cholik Chan. Application of phase change materials for thermal energy storage in concentrated solar thermal power plants: a review to recent developments. *Applied Energy*, 160:286–307, 2015.

[11] Kinga Pielichowska and Krzysztof Pielichowski. Phase change materials for thermal energy storage. *Progress in materials science*, 65:67–123, 2014.

[12] Yuan Tian and Chang-Ying Zhao. A review of solar collectors and thermal energy storage in solar thermal applications. *Applied energy*, 104:538–553, 2013.

[13] A Felix Regin, SC Solanki, and JS Saini. Heat transfer characteristics of thermal energy storage system using pcm capsules: a review. *Renewable and Sustainable Energy Reviews*, 12(9):2438–2458, 2008.

[14] Murat Kenisarin and Khamid Mahkamov. Solar energy storage using phase change materials. *Renewable and sustainable energy reviews*, 11(9):1913–1965, 2007.

[15] Amar M Khudhair and Mohammed M Farid. A review on energy conservation in building applications with thermal storage by latent heat using phase change materials. *Energy conversion and management*, 45(2):263–275, 2004.

[16] Mohammed M Farid, Amar M Khudhair, Siddique Ali K Razack, and Said Al-Hallaj. A review on phase change energy storage: materials and applications. *Energy conversion and management*, 45(9-10):1597–1615, 2004.

[17] Belen Zalba, Jose Ma Marın, Luisa F Cabeza, and Harald Mehling. Review on thermal energy storage with phase change: materials, heat transfer analysis and applications. *Applied thermal engineering*, 23(3):251–283, 2003.

[18] Ming Liu, Wasim Saman, and Frank Bruno. Review on storage materials and thermal performance enhancement techniques for high temperature phase change thermal storage systems. *Renewable and Sustainable Energy Reviews*, 16(4):2118–2132, 2012.

[19] Frank Baylin. Low temperature thermal energy storage: A state-of-the-art survey. *NASA STI/Recon Technical Report N*, 80:15583, 1979.

[20] KK Pillai and BJ Brinkworth. The storage of low grade thermal energy using phase change materials. *Applied Energy*, 2(3):205–216, 1976.

[21] A Abhat. Low temperature latent heat thermal energy storage: heat storage materials. *Solar energy*, 30(4):313–332, 1983.

[22] Concentrating solar power basics.

[23] JT Brinkley, Bennett Widyolar, Lun Jiang, Souvik Roy, Gerardo Diaz, James Palko, and Roland Winston. Low cost dispatchable heat for small scale solar thermal desalination systems. *Nonimaging Optics: Efficient Design for Illumination and Solar Concentration*, 16(11120):1112009, 2019.

[24] Jordyn Brinkley, Bennett Widyolar, Lun Jiang, Souvik Roy, Gerardo Diaz, James Wayne Palko, and Roland Winston. The internal compound parabolic concentrator (icpc)-a novel low cost solar thermal collection system for desalination processes. Technical report, Univ. of California, Merced, CA (United States), 2023.

[25] A Buscemi, D Panno, G Ciulla, M Beccali, and V Lo Brano. Concrete thermal energy storage for linear fresnel collectors: Exploiting the south mediterranean's solar potential for agri-food processes. *Energy Conversion and Management*, 166:719–734, 2018.

[26] Rui Chen, Zhenghua Rao, and Shengming Liao. Determination of key parameters for sizing the heliostat field and thermal energy storage in solar tower power plants. *Energy conversion and management*, 177:385–394, 2018.

[27] Fatih Sorgulu and Ibrahim Dincer. Design and analysis of a solar tower power plant integrated with thermal energy storage system for cogeneration. *International Journal of Energy Research*, 43(12):6151–6160, 2019.

[28] Maria Telkes. Thermal energy storage in salt hydrates. *Solar Energy Materials*, 2(4):381–393, 1980.

[29] M Fatih Demirbas. Thermal energy storage and phase change materials: an overview. *Energy Sources, Part B: Economics, Planning, and Policy*, 1(1):85–95, 2006.

[30] Arefeh Hesaraki, Sture Holmberg, and Fariborz Haghighat. Seasonal thermal energy storage with heat pumps and low temperatures in building projects—a comparative review. *Renewable and Sustainable Energy Reviews*, 43:1199–1213, 2015.

[31] CW Chan, J Ling-Chin, and AP Roskilly. A review of chemical heat pumps, thermodynamic cycles and thermal energy storage technologies for low grade heat utilisation. *Applied thermal engineering*, 50(1):1257–1273, 2013.

[32] Dominika Matuszewska, Marta Kuta, and Piotr Olczak. Techno-economic assessment of mobilized thermal energy storage system using geothermal source in polish conditions. *Energies*, 13(13):3404, 2020.

[33] Laia Miró, Jaume Gasia, and Luisa F Cabeza. Thermal energy storage (tes) for industrial waste heat (iwh) recovery: A review. *Applied energy*, 179:284–301, 2016.

[34] Kevin Merlin, Jérôme Soto, Didier Delaunay, and Luc Traonvouez. Industrial waste heat recovery using an enhanced conductivity latent heat thermal energy storage. *Applied energy*, 183:491–503, 2016.

[35] Jacob Edwards, Hitesh Bindra, and Piyush Sabharwall. Exergy analysis of thermal energy storage options with nuclear power plants. *Annals of Nuclear Energy*, 96:104–111, 2016.

[36] Abdullah A Al Kindi, Marko Aunedi, Antonio M Pantaleo, Goran Strbac, and Christos N Markides. Thermo-economic assessment of flexible nuclear power plants in future low-carbon electricity systems: Role of thermal energy storage. *Energy Conversion and Management*, 258:115484, 2022.

[37] D Buddhi and RL Sawhney. Proc: Thermal energy storage and energy conversion. *School of Energy and Environmental Studies, Devi Ahilya University, Indore, India*, 1994.

[38] Bruno Cárdenas and Noel León. High temperature latent heat thermal energy storage: Phase change materials, design considerations and performance enhancement techniques. *Renewable and sustainable energy reviews*, 27:724–737, 2013.

[39] Cemil Alkan and Ahmet Sari. Fatty acid/poly (methyl methacrylate)(pmma) blends as form-stable phase change materials for latent heat thermal energy storage. *Solar energy*, 82(2):118–124, 2008.

[40] Lijiu Wang and Duo Meng. Fatty acid eutectic/polymethyl methacrylate composite as form-stable phase change material for thermal energy storage. *Applied Energy*, 87(8):2660–2665, 2010.

[41] K Pielichowska, S Głowinkowski, J Lekki, D Biniaś, K Pielichowski, and J Jenczyk. Peo/fatty acid blends for thermal energy storage materials. structural/morphological features and hydrogen interactions. *European Polymer Journal*, 44(10):3344–3360, 2008.

[42] Krzysztof Pielichowski and Kinga Flejtuch. Recent developments in polymeric phase change materials for energy storage: poly (ethylene oxide)/stearic acid blends. *Polymers for advanced technologies*, 16(2-3):127–132, 2005.

[43] Ahmet Sarı, Cemil Alkan, Ali Karaipekli, and Adem Önal. Preparation, characterization and thermal properties of styrene maleic anhydride copolymer (sma)/fatty acid composites as form stable phase change materials. *Energy conversion and management*, 49(2):373–380, 2008.

[44] Ye Hong and Ge Xin-Shi. Preparation of polyethylene–paraffin compound as a form-stable solid-liquid phase change material. *Solar Energy Materials and Solar Cells*, 64(1):37–44, 2000.

[45] H Inaba and P Tu. Evaluation of thermophysical characteristics on shape-stabilized paraffin as a solid-liquid phase change material. *Heat and Mass Transfer*, 32(4):307–312, 1997.

[46] Ahmet Sarı. Form-stable paraffin/high density polyethylene composites as solid–liquid phase change material for thermal energy storage: preparation and thermal properties. *Energy Conversion and Management*, 45(13-14):2033–2042, 2004.

[47] Chang Hyung Lee and Hyeong Ki Choi. Crystalline morphology in high-density polyethylene/paraffin blend for thermal energy storage. *Polymer composites*, 19(6):704–708, 1998.

[48] Yibing Cai, Qufu Wei, Fenglin Huang, and Weidong Gao. Preparation and properties studies of halogen-free flame retardant form-stable phase change materials based on paraffin/high density polyethylene composites. *Applied energy*, 85(8):765–775, 2008.

[49] Yibing Cai, Qufu Wei, Fenglin Huang, Shiliang Lin, Fang Chen, and Weidong Gao. Thermal stability, latent heat and flame retardant properties of the thermal energy storage phase change materials based on paraffin/high density polyethylene composites. *Renewable Energy*, 34(10):2117–2123, 2009.

[50] Xiang Huang, Guruprasad Alva, Lingkun Liu, and Guiyin Fang. Microstructure and thermal properties of cetyl alcohol/high density polyethylene composite phase change materials with carbon fiber as shape-stabilized thermal storage materials. *Applied Energy*, 200:19–27, 2017.

[51] Igor Krupa, Gizela Miková, and AS Luyt. Phase change materials based on low-density polyethylene/paraffin wax blends. *European Polymer Journal*, 43(11):4695–4705, 2007.

[52] Cemil Alkan, Kemal Kaya, and Ahmet Sarı. Preparation, thermal properties and thermal reliability of form-stable paraffin/polypropylene composite for thermal energy storage. *Journal of Polymers and the Environment*, 17(4):254, 2009.

[53] Alvaro De Gracia and Luisa F Cabeza. Phase change materials and thermal energy storage for buildings. *Energy and Buildings*, 103:414–419, 2015.

[54] Werner Martienssen and Hans Warlimont. *Springer handbook of condensed matter and materials data*. Springer Science & Business Media, 2006.

[55] M Kamimoto, Y Abe, S Sawata, T Tani, and T Ozawa. Latent thermal storage unit using form-stable high density polyethylene; part i: performance of the storage unit. 1986.

[56] Y Abe, Y Takahashi, R Sakamoto, K Kanari, M Kamimoto, and T Ozawa. Charge and discharge characteristics of a direct contact latent thermal energy storage unit using form-stable high-density polyethylene. 1984.

[57] Christoph Zauner, Florian Hengstberger, Mark Etzel, Daniel Lager, Rene Hofmann, and Heimo Walter. Durability of a fin-tube latent heat storage using high density polyethylene as pcm. In *IOP Conference Series: Materials Science and Engineering*, volume 251, page 012123. IOP Publishing, 2017.

[58] Christoph Zauner, Florian Hengstberger, Mark Etzel, Daniel Lager, Rene Hofmann, and Heimo Walter. Experimental characterization and simulation of a fin-tube latent heat storage using high density polyethylene as pcm. *Applied energy*, 179:237–246, 2016.

[59] Ival O Salyer and Joseph E Davison. Thermal-energy storage in crosslinked pellets of high-density polythylene for home heating and cooling via off-peak electric power utilization. *Journal of applied polymer science*, 28(9):2903–2924, 1983.

[60] Hideo Inaba and Zhongmin Li. Thermal energy storage characteristics of a latent heat storage vessel packed with surface cross-linked, form-stabilized, high-density polyethylene pellets by boiling phenomenon. *Heat Transfer—Asian Research: Co-sponsored by the Society of Chemical Engineers of Japan and the Heat Transfer Division of ASME*, 28(8):649–663, 1999.

[61] C Yang, ME Navarro, B Zhao, G Leng, G Xu, L Wang, Y Jin, and Y Ding. Thermal conductivity enhancement of recycled high density polyethylene as a storage media for latent heat thermal energy storage. *Solar Energy Materials and Solar Cells*, 152:103–110, 2016.

[62] S Jegadheeswaran and Sanjay D Pohekar. Performance enhancement in latent heat thermal storage system: a review. *Renewable and Sustainable energy reviews*, 13(9):2225–2244, 2009.

[63] Liwu Fan and Jay M Khodadadi. Thermal conductivity enhancement of phase change materials for thermal energy storage: a review. *Renewable and sustainable energy reviews*, 15(1):24–46, 2011.

[64] Lingkun Liu, Di Su, Yaojie Tang, and Guiyin Fang. Thermal conductivity enhancement of phase change materials for thermal energy storage: A review. *Renewable and Sustainable Energy Reviews*, 62:305–317, 2016.

[65] Nasiru I Ibrahim, Fahad A Al-Sulaiman, Saidur Rahman, Bekir S Yilbas, and Ahmet Z Sahin. Heat transfer enhancement of phase change materials for thermal energy storage applications: A critical review. *Renewable and Sustainable Energy Reviews*, 74:26–50, 2017.

[66] Zhenjun Ma, Wenye Lin, and M Imroz Sohel. Nano-enhanced phase change materials for improved building performance. *Renewable and Sustainable Energy Reviews*, 58:1256–1268, 2016.

[67] C Amaral, R Vicente, PAAP Marques, and A Barros-Timmons. Phase change materials and carbon nanostructures for thermal energy storage: A literature review. *Renewable and Sustainable Energy Reviews*, 79:1212–1228, 2017.

[68] Zhenyu Liu, Yuanpeng Yao, and Huiying Wu. Numerical modeling for solid–liquid phase change phenomena in porous media: Shell-and-tube type latent heat thermal energy storage. *Applied energy*, 112:1222–1232, 2013.

[69] Xin Xiao, Peng Zhang, and Ming Li. Effective thermal conductivity of open-cell metal foams impregnated with pure paraffin for latent heat storage. *International Journal of Thermal Sciences*, 81:94–105, 2014.

[70] Changhong Wang, Tao Lin, Na Li, and Huanpei Zheng. Heat transfer enhancement of phase change composite material: Copper foam/paraffin. *Renewable energy*, 96:960–965, 2016.

[71] YB Tao, Y You, and YL He. Lattice boltzmann simulation on phase change heat transfer in metal foams/paraffin composite phase change material. *Applied Thermal Engineering*, 93:476–485, 2016.

[72] Y Zhao, CY Zhao, ZG Xu, and HJ Xu. Modeling metal foam enhanced phase change heat transfer in thermal energy storage by using phase field method. *International Journal of Heat and Mass Transfer*, 99:170–181, 2016.

[73] Weidong Liang, Guodong Zhang, Hanxue Sun, Pinsong Chen, Zhaoqi Zhu, and An Li. Graphene–nickel/n-carboxylic acids composites as form-stable phase change materials for thermal energy storage. *Solar Energy Materials and Solar Cells*, 132:425–430, 2015.

[74] Zichen Wang, Zhuqian Zhang, Li Jia, and Lixin Yang. Paraffin and paraffin/aluminum foam composite phase change material heat storage experimental study based on thermal management of li-ion battery. *Applied Thermal Engineering*, 78:428–436, 2015.

[75] Ahmet Sarı and Ali Karaipekli. Thermal conductivity and latent heat thermal energy storage characteristics of paraffin/expanded graphite composite as phase change material. *Applied thermal engineering*, 27(8-9):1271–1277, 2007.

[76] Yajuan Zhong, Quangui Guo, Sizhong Li, Jingli Shi, and Lang Liu. Heat transfer enhancement of paraffin wax using graphite foam for thermal energy storage. *Solar Energy Materials and Solar Cells*, 94(6):1011–1014, 2010.

[77] L Xia and P Zhang. Thermal property measurement and heat transfer analysis of acetamide and acetamide/expanded graphite composite phase change material for solar heat storage. *Solar Energy Materials and Solar Cells*, 95(8):2246–2254, 2011.

[78] Xianglei Wang, Quangui Guo, Yajuan Zhong, Xinghai Wei, and Lang Liu. Heat transfer enhancement of neopentyl glycol using compressed expanded natural graphite for thermal energy storage. *Renewable energy*, 51:241–246, 2013.

[79] Yajun Lv, Weibing Zhou, and Weizhun Jin. Experimental and numerical study on thermal energy storage of polyethylene glycol/expanded graphite composite phase change material. *Energy and Buildings*, 111:242–252, 2016.

[80] S Wu, TX Li, T Yan, YJ Dai, and RZ Wang. High performance form-stable expanded graphite/stearic acid composite phase change material for modular thermal energy storage. *International Journal of heat and mass transfer*, 102:733–744, 2016.

[81] Tao Xu, Qinglin Chen, Gongsheng Huang, Zhengguo Zhang, Xuenong Gao, and Shushen Lu. Preparation and thermal energy storage properties of d-mannitol/expanded graphite composite phase change material. *Solar Energy Materials and Solar Cells*, 155:141–146, 2016.

[82] Weihuan Zhao, David M France, Wenhua Yu, Taeil Kim, and Dileep Singh. Phase change material with graphite foam for applications in high-temperature latent heat storage systems of concentrated solar power plants. *Renewable Energy*, 69:134–146, 2014.

[83] Zhaowen Huang, Xuenong Gao, Tao Xu, Yutang Fang, and Zhengguo Zhang. Thermal property measurement and heat storage analysis of lino3/kcl–expanded graphite composite phase change material. *Applied energy*, 115:265–271, 2014.

[84] YJ Zhao, RZ Wang, LW Wang, and N Yu. Development of highly conductive kno3/nano3 composite for tes (thermal energy storage). *Energy*, 70:272–277, 2014.

[85] X Xiao, P Zhang, and M Li. Experimental and numerical study of heat transfer performance of nitrate/expanded graphite composite pcm for solar energy storage. *Energy Conversion and Management*, 105:272–284, 2015.

[86] Dileep Singh, Weihuan Zhao, Wenhua Yu, David M France, and Taeil Kim. Analysis of a graphite foam–nacl latent heat storage system for supercritical co2 power cycles for concentrated solar power. *Solar Energy*, 118:232–242, 2015.

[87] Dileep Singh, Taeil Kim, Weihuan Zhao, Wenhua Yu, and David M France. Development of graphite foam infiltrated with mgcl2 for a latent heat based thermal energy storage (lhtes) system. *Renewable Energy*, 94:660–667, 2016.

[88] Jifen Wang, Huaqing Xie, Zhong Xin, Yang Li, and Lifei Chen. Enhancing thermal conductivity of palmitic acid based phase change materials with carbon nanotubes as fillers. *Solar Energy*, 84(2):339–344, 2010.

[89] Peijun Ji, Huanhuan Sun, Yunxia Zhong, and Wei Feng. Improvement of the thermal conductivity of a phase change material by the functionalized carbon nanotubes. *Chemical engineering science*, 81:140–145, 2012.

[90] Tun-Ping Teng, Ching-Min Cheng, and Chin-Pao Cheng. Performance assessment of heat storage by phase change materials containing mwcnts and graphite. *Applied thermal engineering*, 50(1):637–644, 2013.

[91] TingXian Li, Ju-Hyuk Lee, RuZhu Wang, and Yong Tae Kang. Enhancement of heat transfer for thermal energy storage application using stearic acid nanocomposite with multi-walled carbon nanotubes. *Energy*, 55:752–761, 2013.

[92] TingXian Li, Ju-Hyuk Lee, RuZhu Wang, and Yong Tae Kang. Heat transfer characteristics of phase change nanocomposite materials for thermal energy storage application. *International Journal of Heat and Mass Transfer*, 75:1–11, 2014.

[93] Min Li, Meirong Chen, Zhishen Wu, and Jianxun Liu. Carbon nanotube grafted with polyalcohol and its influence on the thermal conductivity of phase change material. *Energy conversion and management*, 83:325–329, 2014.

[94] Da Hee Choi, Juhyuk Lee, Hiki Hong, and Yong Tae Kang. Thermal conductivity and heat transfer performance enhancement of phase change materials (pcm) containing carbon additives for heat storage application. *International journal of refrigeration*, 42:112–120, 2014.

[95] YB Tao, CH Lin, and YL He. Preparation and thermal properties characterization of carbonate salt/carbon nanomaterial composite phase change material. *Energy conversion and management*, 97:103–110, 2015.

[96] YB Tao, CH Lin, and YL He. Effect of surface active agent on thermal properties of carbonate salt/carbon nanomaterial composite phase change material. *Applied energy*, 156:478–489, 2015.

[97] Sumin Kim and Lawrence T Drzal. High latent heat storage and high thermal conductive phase change materials using exfoliated graphite nanoplatelets. *Solar Energy Materials and Solar Cells*, 93(1):136–142, 2009.

[98] Min Li. A nano-graphite/paraffin phase change material with high thermal conductivity. *Applied energy*, 106:25–30, 2013.

[99] Mohammad Mehrali, Sara Tahan Latibari, Mehdi Mehrali, Teuku Meurah Indra Mahlia, Emad Sadeghinezhad, and Hendrik Simon Cornelis Metselaar. Preparation of nitrogen-doped graphene/palmitic acid shape stabilized composite phase change material with remarkable thermal properties for thermal energy storage. *Applied energy*, 135:339–349, 2014.

[100] Trung Dung Dao and Han Mo Jeong. Novel stearic acid/graphene core–shell composite microcapsule as a phase change material exhibiting high shape stability and performance. *Solar Energy Materials and Solar Cells*, 137:227–234, 2015.

[101] Aziz Babapoor and Gholamreza Karimi. Thermal properties measurement and heat storage analysis of paraffinnanoparticles composites phase change material: Comparison and optimization. *Applied Thermal Engineering*, 90:945–951, 2015.

[102] Philip D Myers Jr, Tanvir E Alam, Rajeev Kamal, DY Goswami, and E Stefanakos. Nitrate salts doped with cuo nanoparticles for thermal energy storage with improved heat transfer. *Applied Energy*, 165:225–233, 2016.

[103] RK Sharma, P Ganesan, VV Tyagi, HSC Metselaar, and SC Sandaran. Thermal properties and heat storage analysis of palmitic acid-tio2 composite as nano-enhanced organic phase change material (neopcm). *Applied Thermal Engineering*, 99:1254–1262, 2016.

[104] Sina Lohrasbi, Mohsen Sheikholeslami, and Davood Domiri Ganji. Discharging process expedition of nepcm in fin-assisted latent heat thermal energy storage system. *Journal of molecular liquids*, 221:833–841, 2016.

[105] Jean-Pierre Bedecarrats, Jean Castaing-Lasvignottes, Françoise Strub, and Jean-Pierre Dumas. Study of a phase change energy storage using spherical capsules. part i: Experimental results. *Energy Conversion and Management*, 50(10):2527–2536, 2009.

[106] Jean-Pierre Bedecarrats, Jean Castaing-Lasvignottes, Françoise Strub, and Jean-Pierre Dumas. Study of a phase change energy storage using spherical capsules. part ii: Numerical modelling. *Energy Conversion and Management*, 50(10):2537–2546, 2009.

[107] Mario Cascetta, Giorgio Cau, Pierpaolo Puddu, and Fabio Serra. A comparison between cfd simulation and experimental investigation of a packed-bed thermal energy storage system. *Applied Thermal Engineering*, 98:1263–1272, 2016.

[108] Ming Wu, Chao Xu, and Ya-Ling He. Dynamic thermal performance analysis of a molten-salt packed-bed thermal energy storage system using pcm capsules. *Applied Energy*, 121:184–195, 2014.

[109] Harmeet Singh, RP Saini, and JS Saini. A review on packed bed solar energy storage systems. *Renewable and Sustainable Energy Reviews*, 14(3):1059–1069, 2010.

[110] J Pascal Coutier and EA Farber. Two applications of a numerical approach of heat transfer process within rock beds. *Solar Energy*, 29(6):451–462, 1982.

[111] M Kamimoto, Y Abe, K Kanari, Y Takahashi, T Tani, and T Ozawa. Latent thermal storage unit using form-stable high density polyethylene; part ii: numerical analysis of heat transfer. 1986.

[112] Sergio Pintaldi, Cristian Perfumo, Subbu Sethuvenkatraman, Stephen White, and Gary Rosengarten. A review of thermal energy storage technologies and control approaches for solar cooling. *Renewable and Sustainable Energy Reviews*, 41:975–995, 2015.

[113] Mahmood Mastani Joybari, Fariborz Haghighat, Jeff Moffat, and Paul Sra. Heat and cold storage using phase change materials in domestic refrigeration systems: The state-of-the-art review. *Energy and Buildings*, 106:111–124, 2015.

[114] E Oró, A De Gracia, Albert Castell, Mohammed M Farid, and Luisa F Cabeza. Review on phase change materials (pcms) for cold thermal energy storage applications. *Applied Energy*, 99:513–533, 2012.

[115] Ibrahim Dincer and Marc Rosen. *Thermal energy storage: systems and applications.* John Wiley & Sons, 2002.

[116] Walter Goldstern. *Steam Storage Installations: Construction, Design, and Operation of Industrial Heat Accumulators*, volume 4. Pergamon, 1970.

[117] Wolf-Dieter Steinmann and Markus Eck. Buffer storage for direct steam generation. *Solar Energy*, 80(10):1277–1282, 2006.

[118] Marc Medrano, Antoni Gil, Ingrid Martorell, Xavi Potau, and Luisa F Cabeza. State of the art on high-temperature thermal energy storage for power generation. part 2—case studies. *Renewable and Sustainable Energy Reviews*, 14(1):56–72, 2010.

[119] Fengwu Bai and Chao Xu. Performance analysis of a two-stage thermal energy storage system using concrete and steam accumulator. *Applied Thermal Engineering*, 31(14-15):2764–2771, 2011.

[120] LyondellBasell. Technical Data Sheet, Petrothene LM600700. Oct. 6, 2019 [Online]. Accessed Apr. 11, 2022.

[121] Henkel Corporation. Technical Data Sheet, Loctite Epoxy Marine. April 24, 2018 [Online]. Accessed Apr. 11, 2022.

[122] R Byron Bird, Warren E Stewart, and Edwin N Lightfoot. Transport phenomena revised 2nd edition, 2006.

[123] J.F. Richardson, J.H. Harker, and J.R. Backhurst. Chapter 4 - Flow of Fluids through Granular Beds and Packed Columns. In J.F. Richardson, J.H. Harker, and J.R. Backhurst, editors, *Chemical Engineering*, Chemical Engineering Series, pages 191–236. Butterworth-Heinemann, Oxford, Fifth edition, 2002.

[124] Victor Pozzobon, Julien Colin, and Patrick Perre. Hydrodynamics of a packed bed of non-spherical polydisperse particles: A fully virtual approach validated by experiments. *Chemical Engineering Journal*, 354:126–136, 2018.

[125] Irving Cruz-Matías, Dolors Ayala, Daniel Hiller, Sebastian Gutsch, Margit Zacharias, Sònia Estradé, and Francesca Peiró. Sphericity and roundness computation for particles using the extreme vertices model. *Journal of Computational Science*, 30:28–40, 2019.

[126] F.A.L. DULLIEN. 3 - Single-Phase Transport Phenomena in Porous Media. In F.A.L. DULLIEN, editor, *Porous Media (Second Edition)*, pages 237–317. Academic Press, San Diego, second edition edition, 1992.

[127] Calculate density and viscosity of glycerol/water mixtures, 4 April 2018.

[128] Suhil Kiwan and Qusai R. Soud. Experimental investigation of the thermal performance of a sand-basalt heat storage system for beam-down solar concentrators. *Case Studies in Thermal Engineering*, 19:100609, 2020.

[129] The materials analyst, part 69: Density, bulk density, melt density, and specific gravity (web-exclusive), Jan 01, 2006.

[130] FairField. Poly-fil heavy/mid/light weight batting. Accessed March. 08, 2023.

[131] Density of pet plastic — the ultimate guide, Feb 11, 2023.

[132] Souvik Roy, Gerardo Diaz, Roland Winston, and James W. Palko. Packed bed thermal energy storage system using form-stable high-density polyethylene. *Applied Thermal Engineering*, 218:119209, 2023.

[133] Hua Wei. Surface tension measurement of high density polyethylene and its clay nanocomposites in supercritical nitrogen. Master's thesis, University of Waterloo, 2009.

[134] Bronisłlaw Jańczuk, Tomasz Białopiotrowicz, and Wiesłlaw Wójcik. The components of surface tension of liquids and their usefulness in determinations of surface free energy of solids. *Journal of colloid and interface science*, 127(1):59–66, 1989.

[135] Yu K Shchipalov. Surface energy of crystalline and vitreous silica. *Glass and ceramics*, 57(11-12):374–377, 2000.

[136] Sadık Kakaç, Yaman Yener, and Carolina P Naveira-Cotta. *Heat conduction*. CRC press, 2018.

[137] C. Yang, M.E. Navarro, B. Zhao, G. Leng, G. Xu, L. Wang, Y. Jin, and Y. Ding. Thermal conductivity enhancement of recycled high density polyethylene as a storage media for latent heat thermal energy storage. *Solar Energy Materials and Solar Cells*, 152:103–110, 2016.

[138] A. Sciacovelli, M.E. Navarro, Yi Jin, Geng Qiao, Lifang Zheng, Guanghui Leng, Li Wang, and Yulong Ding. High density polyethylene (hdpe) — graphite composite manufactured by extrusion: A novel way to fabricate

phase change materials for thermal energy storage. *Particuology*, 40:131–140, 2018.

[139] Electricity explained, https://www.eia.gov/energyexplained/electricity/electricity-in-the-us.php, 2022.

[140] Chelsey Ryker. Steam: The most effective way to transfer heat or energy, https://www.nationwideboiler.com/boiler-blog/the-most-effective-way-to-transfer-heat-or-energy.html, 2020.

[141] Spirax Sarco. Steam accumulators, https://www.spiraxsarco.com/learn-about-steam/the-boiler-house/steam-accumulators, 2021.

[142] Sabrina Dusek and Rene Hofmann. A hybrid energy storage concept for future application in industrial processes. *Thermal Science*, 22(5):2235–2242, 2018.

[143] René Hofmann, Sabrina Dusek, Stephan Gruber, and Gerwin Drexler-Schmid. Design optimization of a hybrid steam-pcm thermal energy storage for industrial applications. *Energies*, 12(5):898, 2019.

[144] Jochen Buschle, Wolf-Dieter Steinmann, and Rainer Tamme. Latent heat storage for process heat applications. 2006.

[145] Alessandro Biglia, Lorenzo Comba, Enrico Fabrizio, Paolo Gay, and Davide Ricauda Aimonino. Steam batch thermal processes in unsteady state conditions: Modelling and application to a case study in the food industry. *Applied Thermal Engineering*, 118:638–651, 2017.

[146] Vladimir D Stevanovic, Blazenka Maslovaric, and Sanja Prica. Dynamics of steam accumulation. *Applied Thermal Engineering*, 37:73–79, 2012.

[147] Ryo Murakoshi and Chihiro Fushimi. Integration of a steam accumulator with a biomass power-generation system for flexible energy storage and discharge: Effect of the initial steam pressure on the steam discharge profile and levelized cost of storage. *Journal of Energy Storage*, 55:105586, 2022.

[148] Rainer Tamme, Thomas Bauer, Jochen Buschle, Doerte Laing, Hans Müller-Steinhagen, and Wolf-Dieter Steinmann. Latent heat storage above 120 °C for applications in the industrial process heat sector and solar power generation. *International Journal of energy research*, 32(3):264–271, 2008.

[149] M ARROYO López-Manchado and M Arroyo. Thermal and dynamic mechanical properties of polypropylene and short organic fiber composites. *Polymer*, 41(21):7761–7767, 2000.

[150] Abdulla M Gasanaliev and Bariyat Yu Gamataeva. Heat-accumulating properties of melts. *Russian Chemical Reviews*, 69(2):179, 2000.

[151] Y Li, G Yue, YM Yu, and QZ Zhu. Preparation and thermal characterization of lino3–nano3–kcl ternary mixture and lino3–nano3–kcl/eg composites. *Energy*, 196:117067, 2020.

[152] Zhaowen Huang, Zigeng Luo, Xuenong Gao, Xiaoming Fang, Yutang Fang, and Zhengguo Zhang. Investigations on the thermal stability, long-term reliability of lino3/kcl–expanded graphite composite as industrial waste heat storage material and its corrosion properties with metals. *Applied energy*, 188:521–528, 2017.

[153] Rasaiah Naveenkumar, Manickam Ravichandran, Vinayagam Mohanavel, Alagar Karthick, Lawrence Sundar Raj Leo Aswin, Swaminathan Shanmugasundaram Harini Priyanka, Sundramurthy Kiran Kumar, and Shanmugavelan Pradeep Kumar. Review on phase change materials for solar energy storage applications. *Environmental Science and Pollution Research*, 29(7):9491–9532, 2022.

[154] Resource Recycling. Occ and mixed paper prices jump this month, https://resource-recycling.com/recycling/2023/09/11/occ-and-mixed-paper-prices-jump-this-month/, 2023.

[155] DA Shnaider, PN Divnich, and IE Vakhromeev. Modeling the dynamic mode of steam accumulator. *Automation and Remote Control*, 71:1994–1998, 2010.

[156] MY Abdelsalam, P Sarafraz, JS Cotton, and MF Lightstone. Heat transfer characteristics of a hybrid thermal energy storage tank with phase change materials (pcms) during indirect charging using isothermal coil heat exchanger. *Solar Energy*, 157:462–476, 2017.